Thesis for The Degree of Licentiate of Engineering

Numerical Analysis of Cavitation-Induced Erosion in High-Pressure Fuel Injectors

under static and dynamic lift conditions

Mehmet Özgünoğlu

Department of Mechanics and Maritime Sciences
Chalmers University of Technology
Gothenburg, Sweden, 2024

Numerical Analysis of Cavitation-Induced Erosion in High-Pressure Fuel Injectors
under static and dynamic lift conditions

Mehmet Özgünoğlu

Report No 2024:02

Department of Mechanics and Maritime Sciences
Division of Marine Technology
Chalmers University of Technology
SE-412 96 Göteborg,
Sweden
Phone: +46(0)31 772 1000

Chalmers Reproservice
Gothenburg, Sweden 2024.

To my family.

Numerical Analysis of Cavitation-Induced Erosion in High-Pressure Fuel Injectors

under static and dynamic lift conditions

Mehmet Özgünoğlu

Department of Mechanics and Maritime Sciences
Division of Marine Technology
Chalmers University of Technology

Abstract

Fuel injection systems are crucial for all modern combustion engines. These systems often operate under very high pressures to ensure fast spray breakup for optimal fuel air mixing leading to efficient combustion in order to meet strict emission standards. However, this high-pressure environment, combined with complicated geometries, can lead to sudden velocity and pressure changes within the fuel injector, making it susceptible to cavitation – a phenomenon where local pressure drops below the vapor pressure and the liquid fuel suddenly evaporates. Cavitation-induced erosion in fuel injectors affects combustion efficiency and system durability, presenting a challenge for analysis.

This study explores the numerical assessment of cavitation-induced erosion in high-pressure fuel injectors using computational fluid dynamics (CFD). Reynolds-averaged Navier-Stokes (RANS) and Large Eddy Simulation (LES) are employed with specific sub-models. Cavitation is modeled using the mixture transport of modified Zwart-Gerber-Belamri approach. The investigation starts with low and high lift static needle positions, comparing the results with experimental data to gain insight into erosion behaviour in an industrial heavy duty injector. To examine the effect of the surface deviations to erosion patterns, static high lift condition is modeled with CAD and Tomography Scan separately. Finally, the effect of the needle motion is carried out by implementing "wobbling" and "lift only" motion profiles using RANS.

Keywords

Fuel Injector, CFD, Cavitation Erosion, Wobbling

Acknowledgement

This project is funded by the European Union Horizon 2020, the EDEM project, a Marie Skłodowska-Curie Action Innovative Training Network project, grant number 861002. The simulations were performed on the resources provided by the National Academic Infrastructure for Supercomputing in Sweden (NAISS) and the Swedish National Infrastructure for Computing (SNIC) at Chalmers Centre for Computational Science and Engineering (C3SE) and National Supercomputer Center at Linköping University (NSC).

First and foremost, I would like to express my sincere gratitude to my main supervisor Prof. Rickard E. Bensow for his patience, guidance, and wisdom. It would not have been possible to navigate the challenges of this project in many ways without his expert insight and constructive feedback. My gratitude extends to my co-supervisor Prof. Michael Oevermann both for his valuable inputs and continuous belief on me even before the project. I sincerely appreciate the knowledge and experience that Dr. Mohammad shared with me, enriching my understanding and skills in this field. His willingness to share his insights has been invaluable in my research. Additionally, I would like to extend my gratitude to Gerard Mouokue from Woodward L'Orange for his collaboration.

I also wish to express my appreciation to all my current and former colleagues from Chalmers and the EDEM project. A special mention to Mohsen, Mohammad, Ioli and Gabi that it was a great joy and experience for me to share the same working environment and time with you.

Lastly, I extend my heartfelt thanks to my family, whose unwavering encouragement and support have been my cornerstone throughout this journey. Their presence and faith in me have been my constant source of strength and inspiration.

Contents

Chapter 1

Introduction

1.1 High pressure fuel injectors

The environmental impact of heavy-duty engines, especially in maritime applications, is crucial. Shifting to sustainable solutions is essential for reducing emissions. Dual fuel engines, which can use both liquid fuel and a cleaner alternative such as natural gas, are becoming increasingly important in this sector. Their ability to switch between fuels offers operational flexibility and is a significant step towards greener maritime practices, demonstrating a commitment to reducing the environmental footprint in shipping.

The existence of high-pressure within the injector is a necessary industrial requirement since it is needed to provide efficient mixing/combustion process while taking into consideration stringent emission regulations [1]. Here, high-pressure fuel injectors, in particular heavy-duty dual-fuel engines, are pivotal for delivering the liquid pilot fuel efficiently into the combustion chamber, playing an important role in initiating and controlling the combustion process. The precision and timing of these injectors directly influence engine performance, fuel efficiency, and emission characteristics. The development and optimization of these injectors are essential, with advancements focusing on better fuel delivery control. This is particularly important in dual fuel engines, where balancing the injection of liquid and gaseous fuel is key for optimal performance.

1.2 Cavitation and cavitation erosion of high pressure fuel injector

High pressure environment and geometrical considerations cause sudden local velocity changes within the fuel injector. As a result of these sudden changes in velocity, the injector is more likely prone to cavitation, which occurs if the local pressure becoming less than the vapor pressure.

In fuel injectors, there are two forms of cavitation that can occur. The first, known as geometric cavitation, typically appears as a film-like sheet cavity formation within the nozzle. This mainly originates at the entrance of the orifice hole due to the local pressure drop induced by the orifice inlet hole geometry [2]. This type of cavitation is more pronounced in high lift needle

position. The second type is referred to as string cavitation, which is due to the low pressure regions created by the filament-like vortical structures. While it is understood that both varieties of cavitation influence the characteristics of the fuel spray, the specific impacts of geometrical cavitation and string cavitation have not been distinctly defined [3]. In Figure 1.1, experimental snapshots of string- and geometry-induced cavitation are presented. Here, both of these cavitation structures are observed in the same geometry, but in different needle positions [4].

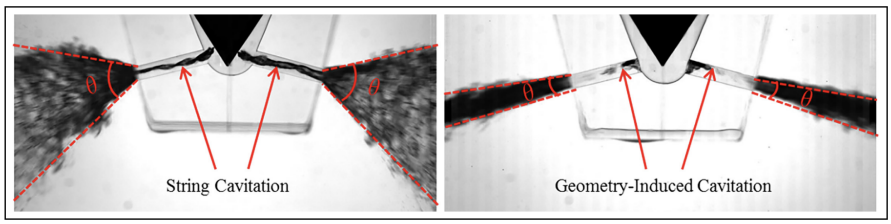

Figure 1.1: Experimental images of string and geometry induced cavitation [4]

In fuel injectors, the occurrence of these cavitation structures is not just a matter of internal fluid dynamics but also significantly impacts the injector's structural integrity. The presence of these cavitation types leads to variation in fuel flow and spray patterns, which are critical for efficient engine combustion.

Transitioning from general cavitation impacts, a key concern is cavitation erosion. This process, in which cavitation structures collapse near the injector surfaces, results in material erosion. This erosion compromises injector durability and performance, impacting both the fuel mixing and combustion processes.

So, this wear mechanism not only reduces the efficiency of the injector over time but also raises concerns about the longevity and maintenance of the fuel injection system. Moreover, material loss due to surface erosion makes the fuel injection system vulnerable to catastrophic system failures. Figure 1.2 illustrates the typical damage caused by cavitation erosion in fuel injectors [5].

1.3 Numerical assessment of cavitation erosion

Conducting experiments on cavitation erosion for high pressure fuel injection systems presents challenges due to the need for specialized equipment capable of replicating extreme pressure conditions accurately while maintaining precise control over fluid dynamics and cavitation phenomena. On the other hand, the ongoing technological development in computational power makes computational techniques a desired tool in the design phase of fuel injection systems. However, cavitation erosion assessment via numerical approaches for industrial high-pressure fuel injectors is still challenging as it requires computationally expensive simulation of flows with a wide range of time and length scales [6]. In addition, a significant challenge lies in the lack of universally valid cavitation models, further complicating the accurate prediction of erosion.

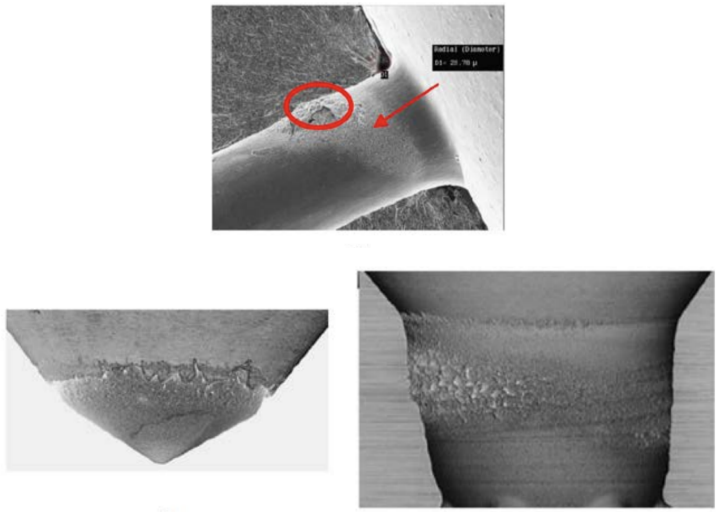

Figure 1.2: Cavitation erosion damage on a fuel injector components (orifice, needle and sac) [5]

Numerical assessment of cavitation erosion, conducted by various research groups, have explored a wide range of contexts beyond fuel injectors. These studies take into account diverse physical mechanisms and employ high-fidelity methods to understand cavitation erosion in different environments, such as in propellers, hydrofoils, and other hydraulic components. The numerical methods employed in these studies demonstrate variability in how they address compressibility effects, turbulence modeling, and multiphase flow modeling.

Dular et al. [7] introduced a model based on the detailed physical mechanism of cavitation erosion. These include the implosion of cavitation clouds, the pressure waves, the creation of micro-jets, and the formation of pits [8]. Bensow and Bark [9] employed LES to study cavitating flows over a propeller. Their findings, which align with experimental observations, suggest that LES can effectively capture crucial cavitation mechanisms such as reentrant jets and sheet cavity dynamics, which are important to correctly detect erosion [9].

Li et al. [10] proposed an erosion intensity function to assess the risks of cavitation erosion on hydrofoil surfaces. This function, derived from unsteady RANS simulations, is based on the average of the time derivative of the local pressure above a certain threshold.

Mihatsch et al. [11] used a density-based finite volume method. This method considers the compressibility of both fluid phases and captures the pressure waves induced by collapses. The study focuses on detecting and quantifying vapor structure collapses within the fluid domain, using the expansion of a liquid into a radially divergent gap as a reference. This setup exhibits unsteady sheet and cloud cavitation characteristics.

Peters et al. [12] presented an erosion model that relies on the micro-jet hypothesis. This model uses flow solution data to pinpoint areas prone to micro-jet occurrence. The model's effectiveness in simulating cavitating flows

was validated through experimental comparisons involving sheet cavitation on a NACA 0009 hydrofoil. Furthermore, their multi-scale Euler–Lagrange method effectively evaluates cavitation-induced erosion, aligning closely with observed erosion pit sizes and potentials [13].

Schenke [14] introduced a novel method for assessing the erosive aggressiveness of cavitating flows through numerical simulations. This technique utilizes the cavitation intensity approach combined with impact power functions to predict the impact power of cavity collapses. The numerical method developed by Arabnejad et al. [15],[16] has been effectively used to evaluate the risk of cavitation erosion in an incompressible formulation. This method takes into account both micro-jets and shock waves as key factors in cavitation erosion.

The above studies show that numerical assessment of cavitation erosion have been investigated and tested by many research groups. Experimental facilities are utilised to test and validate the accuracy of the developed models.

In the context of the fuel injector, the experimental techniques are more applicable for low-pressure systems targeting prevention and detection of cavitation-induced erosion inside the fuel injector. The difficulty in performing experiments in a laboratory environment is a known fact due to the nature of high-pressure operating conditions.

Moreover, computational investigation is practical if one would like to see the effects of the geometrical alterations in the design phase of the high-pressure injector, which is the main factor for the cavitation-induced erosion. Hence, a numerical investigation of cavitation-induced erosion is a desirable tool.

Numerical assessment of cavitation-induced erosion in fuel injectors can be grouped into the following categories:

- Modeling with density based and pressure based solvers,
- Taking into account of different turbulence and cavitation closures,
- Assessment of cavitation-induced erosion with different erosion indicator metrics.

Örley et al. [17] performed well-resolved LES methodology inside a nine-hole common rail diesel injector during a full injection cycle using a fully compressible flow solver. They have also configured different simulations for steady needle lift conditions. Their conclusion is that consideration of the unsteady needle motion is necessary for accurate prediction of erosion sensitive areas.

An explicit density-based approach is applied with real-fluid thermodynamic closure by Kolovos et al. [18]. They used different types of thermodynamic closures with the WALE – LES model and investigated the fuel heating and cavitation erosion location relationship during the needle movement for the five-hole injector. They were in good agreement with their numerical results against the X-ray derived surface erosion images. Another compressible simulations is done by Falsafi et al. [19]. They used real geometries and considered the entire injection cycle with time-dependent rail pressure and transient needle movement.

Santos et al. [20] applied LES methodology with the moving mesh technique using ANSYS to investigate cavitation erosion of a gasoline direct injection (GDi) type injector. Having erosion damage images from the injector durability test, they investigated various erosion indicators and concluded that the accumulated erosive power is the most promising indicator for predicting cavitation erosion. Another LES simulation of a diesel injector is applied by Koukouvinis et al. [21]. They simulated two similar injector designs together with the X-ray CT scans. Pressure peak due to vapor collapse is determined as a main tool to assess the cavitation erosion. The predicted pressure peak locations showed particularly good agreement with the observed erosion patterns.

Koukouvinis et al. [22] numerically investigated the high-pressure fuel pump as well. Here, they used a barotropic equation of state with a homogeneous equilibrium model. The locations susceptible to cavitation-induced erosion are identified based on the concept of an adverse pressure gradient, which serves as the necessary cause for the collapse of cavitation structures.

Brunhart [23] studied predictive capability of different erosion indicators for two fuel injection systems. His motivation was to compare the original eroding design with modified non-eroding design together with the experimental erosion images. In this benchmark study, DES and RANS turbulence modeling approaches are investigated. Squared material derivative, $(DP/Dt)^2$, and second derivative of potential power density, $PPD2$ [24], were the most promising erosion indicators among the ones investigated.

Cristofaro et al. [25] simulated the generic Spray A case with an implicit, compressible pressure-based and three-phase algorithm. They used Coherent Structure Model as an LES model to resolve turbulence. Cavitation erosion prone locations here are evaluated with recording the maximum intensity of pressure on the surface. Later, they applied the same algorithm to simulate cavitation in a diesel injector [26]. Here, they particularly investigated the effect of the geometry alterations caused by cavitation erosion by analyzing the nominal design geometry and the eroded one. One of the purposes of their study was to assess cavitation erosion. The conclusion was that the recorded pressure peaks on the nominal geometry fit well with the eroded regions of the experiments. Moreover, they applied the same cavitation erosion assessment strategy [27] to the well reported microthrottle [28].

Zang et al. [29] conducted simulations to investigate the effects of nozzle K-factor and needle lifts on the cavitating flow field and erosion risk within a diesel nozzle featuring a double array of holes. The relative risk of surface erosion served as an index for evaluating cavitation erosion risk on nozzle hole surfaces. The results showed that decreasing the K-factor significantly reduced cavitation intensity on hole surfaces, causing cavitation to retract towards the orifice entrance.

Kumar's study [30] evaluates the ZGB cavitation model coupled with the RANS turbulence model and taking into account the compressibility of both gas and liquid phases. Here, the quantitative and qualitative comparison has been done against experimental data and flow field analysis reveals the formation of vortices in the injector sac volume, including "hole-to-hole" connecting vortices and double "counter-rotating" vortices from the needle wall.

Wang et al. [31] investigate the internal flow characteristics and spray patterns of double-layer multi-hole diesel engine injector nozzles. Both experimental and computational approaches were employed to analyze variations between upper and lower layer nozzle holes. Actual geometry derived from X-ray scans facilitated accurate characterization of individual injection holes. Results indicated more intense cavitation development in upper layer holes, leading to higher injection rates and less cycle-to-cycle variations in spray patterns from lower layer holes.

Magnotti's work [32] introduced the Cavitation-Induced Erosion Risk Assessment (CIERA) tool, which connects multiphase flow simulation predictions with material erosion progression. The tool's development involved validating cavitation and erosion predictions for pressurized diesel fuel flow within channel geometries, including variations in Reynolds and cavitation numbers and different inlet corner geometries. The multiphase flow within the channel was modeled using a compressible mixture model with a homogeneous relaxation model for phase change and a dynamic structure approach with LES for turbulent flow. CIERA predictions demonstrated accurate qualitative and quantitative assessment performances when the results are compared with the experiments.

Mariasiu et al. [33] analyze the impact of different biofuels on erosion during the injection process. The research highlights varying levels of erosion intensity in injector nozzles when using diesel fuel compared to biodiesel and pure vegetable oil. Their findings emphasize the importance of enhancing injection system design and maintenance practices for compression ignition engines fueled with biodiesel.

Mouvanal et al. [34] followed a numerical procedure and aimed at predicting potential erosion caused by cavitation in flow devices such as throttles and nozzles. The proposed technique efficiently captures periodic vapor cloud shedding and collapse, allowing for the prediction of cavitation erosion zones. An algorithm detects collapse pressures indicative of material erosion due to cavitation. Numerical predictions were validated against experimental data, suggesting potential application in reducing the design cycle time of fuel injectors.

The reviewed studies showcase a variety of methodologies for assessing cavitation-induced erosion in fuel injectors, ranging from well-resolved LES methodologies to explicit density-based approaches and the development of novel assessment tools. These studies demonstrate promising results in predicting cavitation and erosion-sensitive areas. However, their direct applicability within an industrial context remains limited due to the high computational cost and complexity. Furthermore, these studies often overlook critical real-world scenarios such as surface deviations and wobbling motion of the needle, which can drastically affect both the occurrence and severity of cavitation and subsequent erosion inside the fuel injector. Hence, there is a significant research gap in developing methodologies that are not only more universally applicable and cost-effective but also capable of incorporating these real-world conditions.

1.4 Scope of the thesis

In this study, both RANS and LES turbulence modeling approaches are evaluated with corresponding $k-\omega$ SST [35] and WALE [36] sub-models. For RANS, the turbulent viscosity is redefined with Reboud's correction [37]. Assuming a homogeneous mixture, cavitation is modeled via a transport equation approach with mass transfer modeling. Therefore, the Zwart-Gerber-Belamri cavitation model is used with altered model coefficients.

Investigations into erosion patterns under various conditions, turbulence models, and needle motions have been conducted. The numerical results have been thoroughly compared with the experimental data, providing valuable insights into cavitation erosion behaviour. The impact of surface deviations and needle motion on erosion patterns has been examined, contributing to a better understanding of cavitation-induced erosion. Consequently, this study emphasizes the importance of coupling computational models with industrial practice, moving beyond simplified academic cases to address the complex interplay of factors encountered in real-world applications.

Chapter 2

Experiments

Experiments were performed on a high-pressure injector from L'Orange, typically used in heavy-duty and marine engines. This injector operates under a pressure of 2200 bar, and features 8 holes designed for optimum fuel delivery. The experiments, conducted at L'Orange facilities, are available for two static lift conditions, 480 µm – high lift and 20 µm – low lift. Figure 2.1 shows photographs taken at the end of the high lift experiment. Here, the geometry is filled with an epoxy material, which fills gaps of the eroded material. The experimental images suggest that material removal occurs predominantly on the upper side of the injector holes. However, it's important to note that the bottom side of the injector was not captured clearly in the photographs.

Although the experiment has been done with fixed lift positions, different erosion patterns are obtained when the injector holes are compared. These discrepancies are thought to be linked with,

- Center position mismatch of the needle within the sac due to machinery vibrations and/or incorrect positioning; and
- Having different surface deviation of each hole. This is going to be discussed in more detail in upcoming sections.

For the low lift condition, surface damage pictures are presented alongside with the filled epoxy materials in Figure 2.2. The damage-free zone is also indicated with red arrows, which starts from the upstream of the needle tip and ends with the start of the erosion. In the middle of the image, the duration information from the experiment is provided. Hence, from left to right, successive total time of the experiments is 2, 4.5, 16, and 40 hours. For both the needle and the sac, erosion patterns gradually increase, and the surface erodes towards the upstream flow direction.

While evaluating cavitation erosion experiments as in this case, it is important to note that the initial geometry becomes invalid once material removal begins. Therefore, it is crucial to exercise caution when comparing computational fluid dynamics (CFD) results with experimental results, as there are no geometry changes that occur during the calculations.

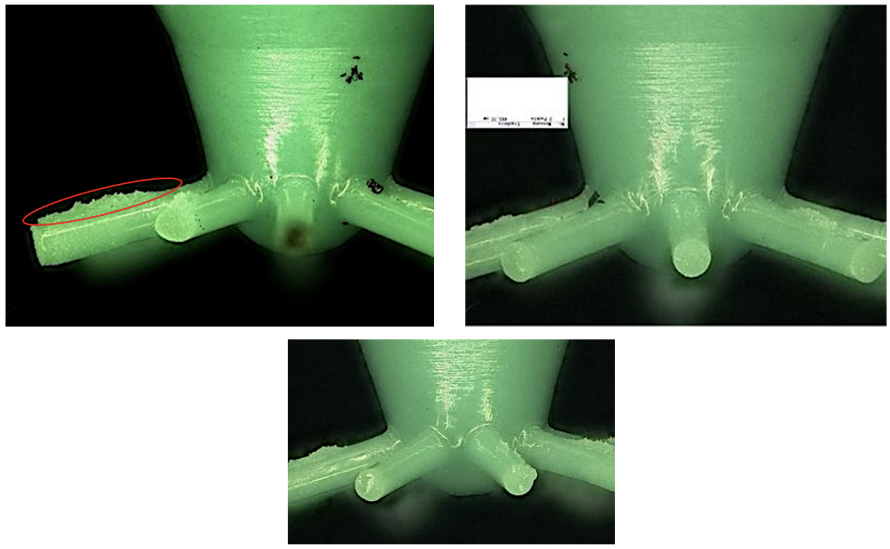

Figure 2.1: Experimental images for the high lift condition

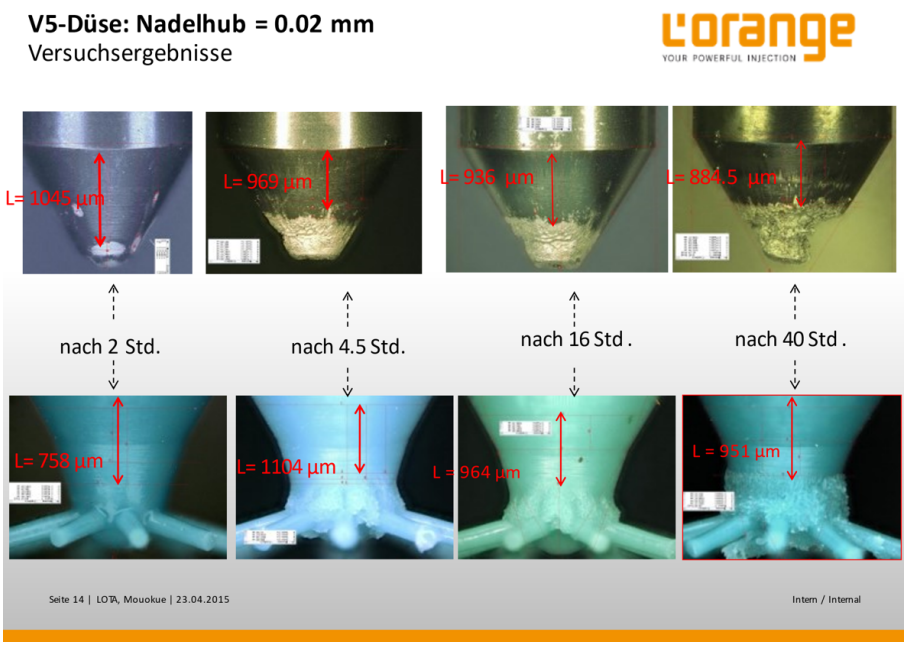

Figure 2.2: Experimental image for the low lift condition

Chapter 3

Simulation Methodology

3.1 Static Needle Simulations

Static needle simulations were planned to investigate:

- Effect of the surface geometry to the prediction of cavitation erosion for high lift condition,
- Effect of the different turbulence modeling closures (RANS/LES),
- Prediction of cavitation erosion for both high and low lift condition.

As stated in the previous section, two static lift conditions, 480 µm and 20 µm, are available. It is important to have a reliable representation of the physical geometry to accurately analyse and assess cavitation induced erosion in numerical simulations. This is even more challenging if the numerical simulations are compared directly with the experiments, since any surface irregularities may serve as location for cavitation triggering or collapse.

Geometry modeling is an important phase for CFD simulations. The CAD models offer design flexibility and simplification but may not capture real-world physics, while the Tomography Scanned (TS) models provide a high-fidelity representation with details of the actual manufactured geometry. Both the CAD and TS Models are provided by Woodward L'Orange. The models are represented in Figure 3.1, and include 8 holes as the default configuration. It is even clear from the provided figure that the surface deviations can easily be seen especially for the injector orifice holes, which are prone to cavitation erosion in high lift condition. More detailed investigations about the surface deviations will be provided in the next subsection.

The numerical simulations are divided into two main categories such as CAD Model and TS Model. These simulations aim to provide a comprehensive understanding of the differences in cavitation erosion behavior in the presence of surface deviations. It should be noted here that surface comparison simulations are kept limited only for the high lift conditions, since it has been experienced that orifice geometry plays a huge role for cavitation erosion analysis while in high lift condition. Hence, the low lift condition is only investigated with the CAD Model.

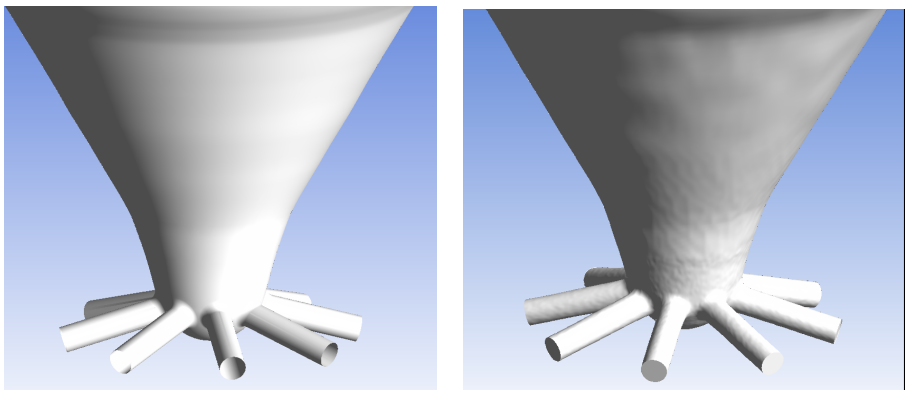

Figure 3.1: CAD (left) and TS surface model comparison

Computational domains are generated as 1-hole for the CAD Model, while for the TS Model both 8-hole and 1-hole domains are generated. The purpose of the 8-hole simulations of the TS Model is to examine the cavitation erosion performance of each orifice solely, to investigate differences between the orifices, and to check on interaction between holes. The modeling of the 8-hole is also a preliminary step for dynamic needle simulations.

Considering the cost and time requirements, LES has been employed only for 1-hole computational domains. To provide a consistent comparison with LES simulations, the same computational domains are also analyzed with the RANS approach. Figure 3.2 shows the simulation overview/tree for all static needle simulations.

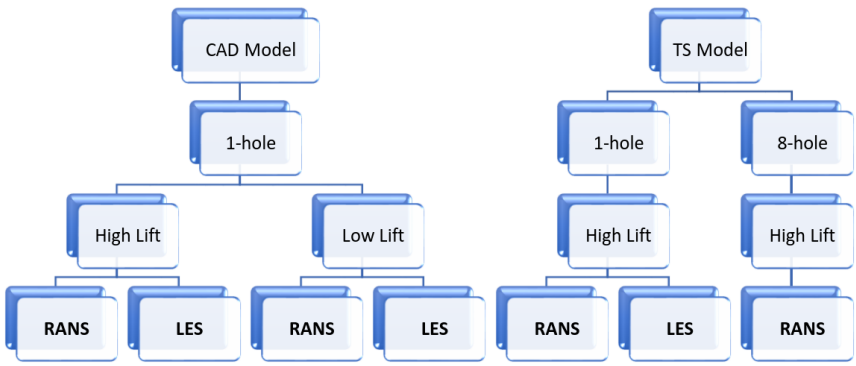

Figure 3.2: Simulation tree for static needle simulations

3.1.1 CAD Model vs TS Model

Figure 3.5, Figure 3.6, and Figure 3.7 present the surface deviation of the TS Model compared to the CAD Model when both models in Figure 3.1 are overlapped and aligned in the center. These contour plots are generated with the GOM Inspect 2022 software [18]. The focus was on analyzing surface deviations, particularly in relation to the orifices' entry dimensions and top/bottom downstream sections.

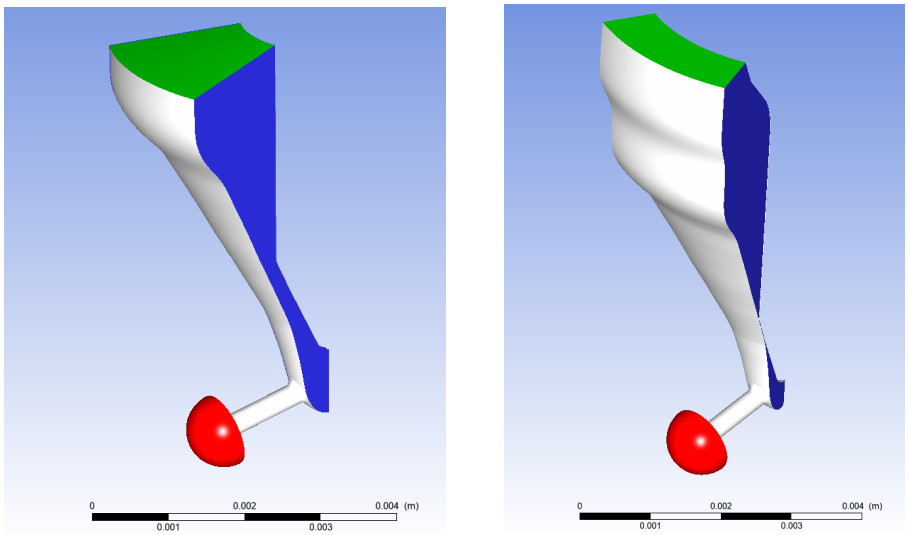

Figure 3.3: High lift (left) and low lift (right) condition, CAD Model, 1-hole

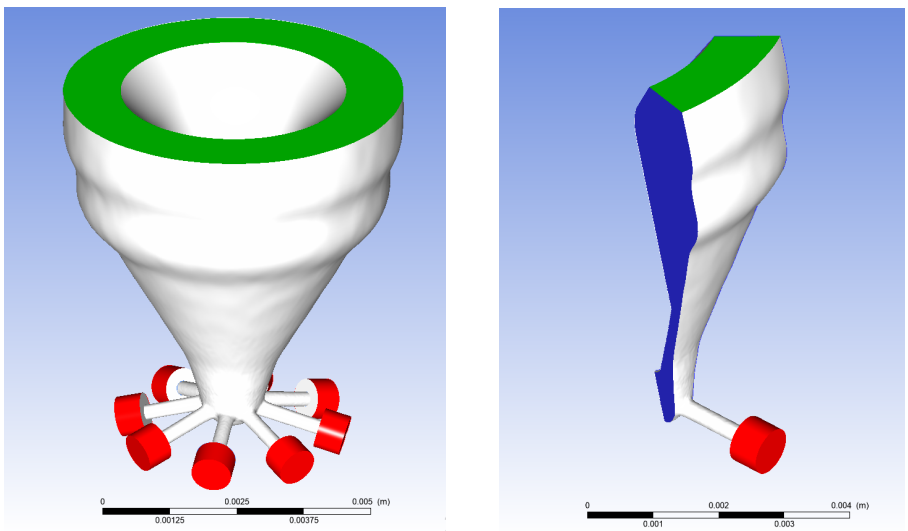

Figure 3.4: 8-hole (left) and 1-hole (right) TS Model in high lift Condition

In general, the top side of the orifices exhibited a positive deviation, while the bottom side showed a negative deviation. These dimensional properties play a crucial role in the generation of cavitation, making this observation particularly significant. The examination further indicated that the entrance diameters of the orifices deviated up to 0.02 mm, positively on the top side and negatively on the bottom side. It is also clear to see that each orifice has different surface deviations and orifice entrance dimensions when they compared with each other. This is another motivation to analyze TS Model with 8-hole configuration using the RANS approach.

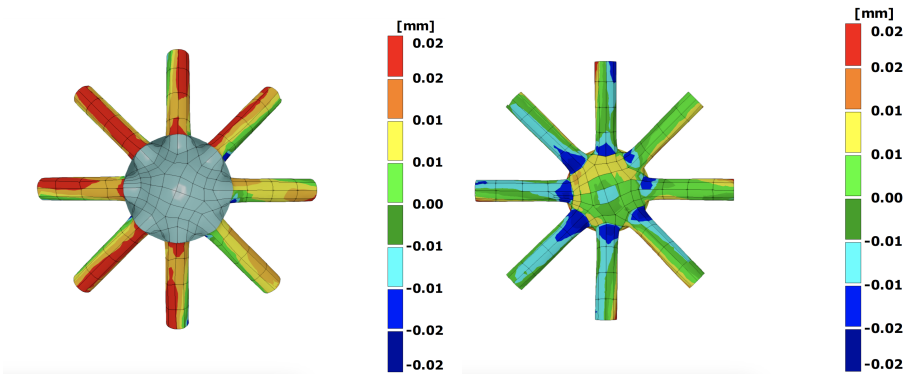

Figure 3.5: Surface deviations between TS and CAD Model injector holes
Top view (left), Bottom view (right)

Figure 3.6: Surface deviations between TS and CAD Model – Isometric view

Figure 3.8 illustrates the selected 1-hole, providing a top view of the 8-hole TS geometry with hole numbering, and a bottom view from the geometry modeller. Previous figures have shown that upstream seating surfaces exhibit surface deviations, making it more challenging to maintain consistent topology and mesh periodicity. Therefore, 'hole7' was chosen as it presents fewer issues compared to the other holes.

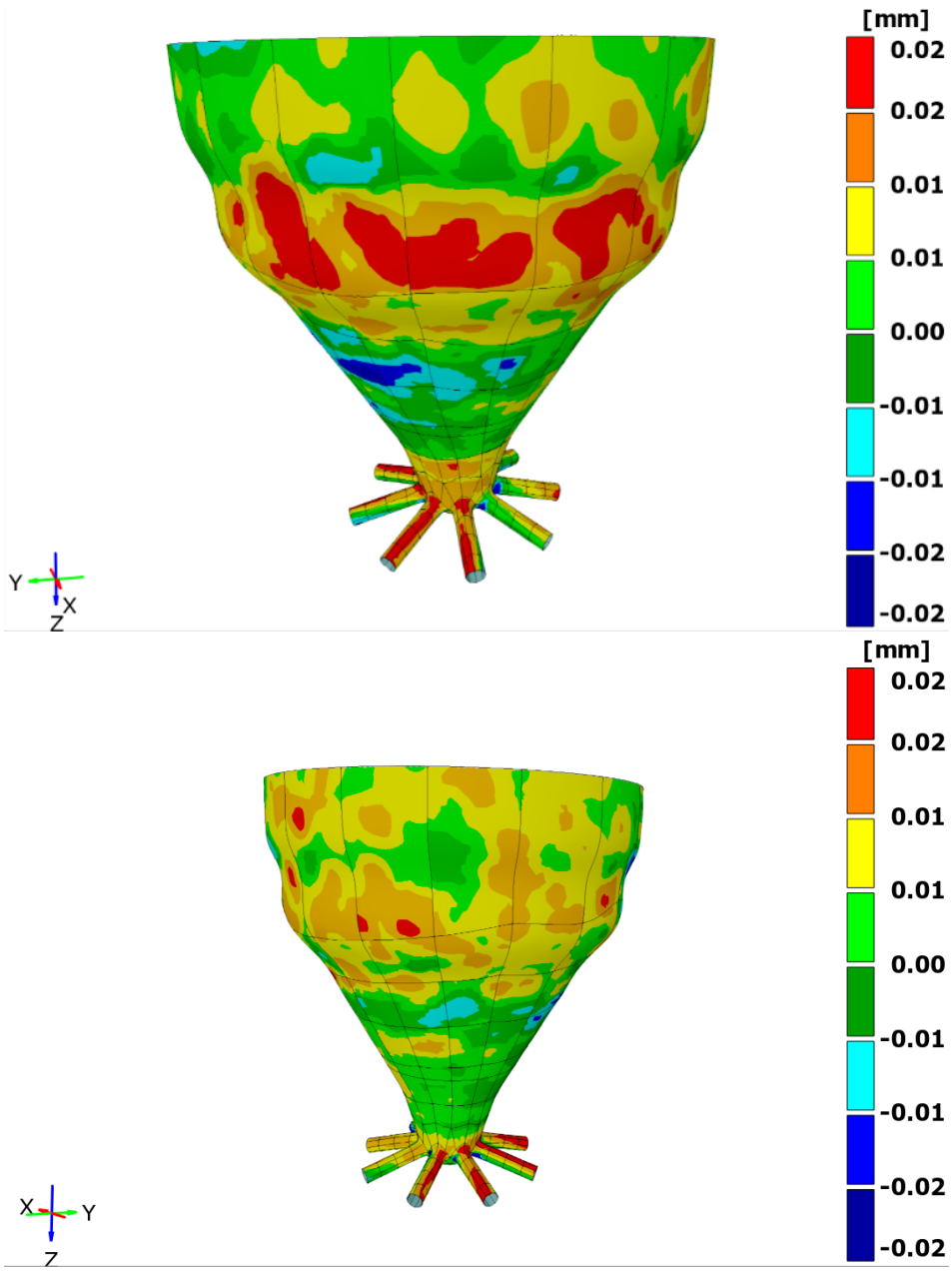

Figure 3.7: Surface deviations between TS and CAD Model – Isometric view

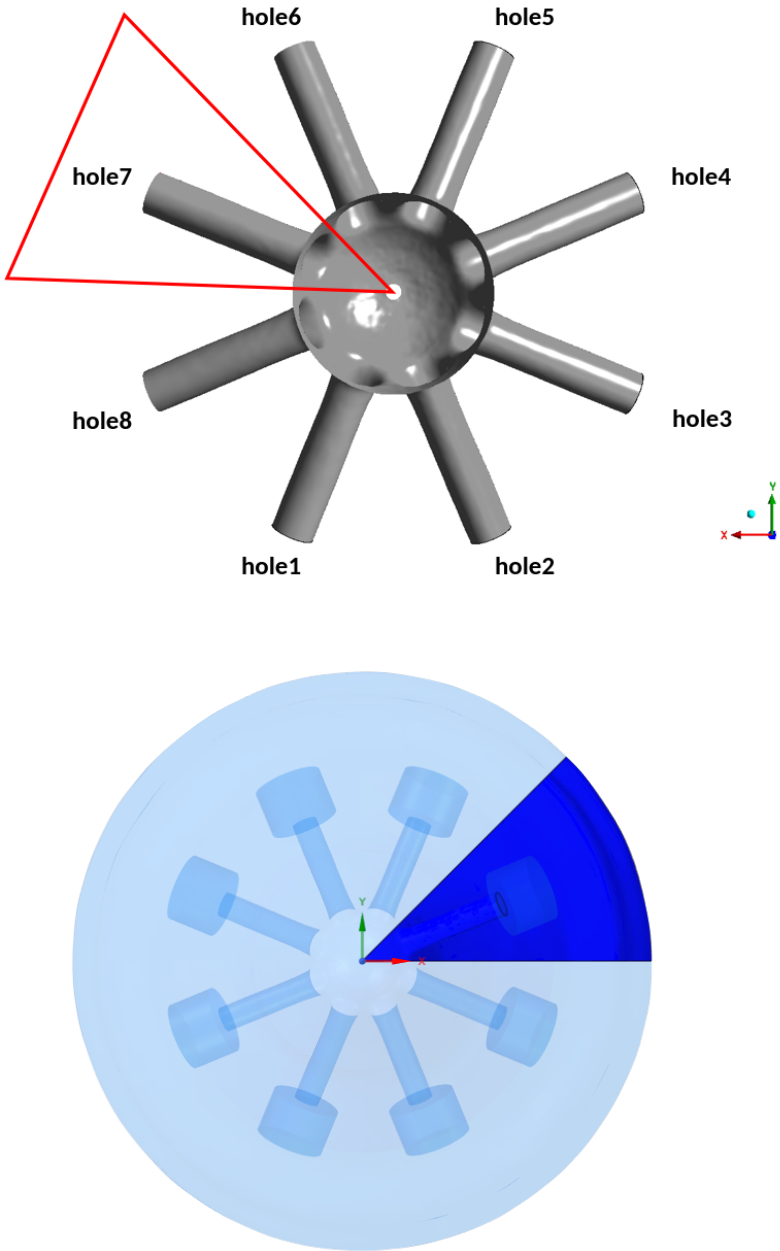

Figure 3.8: Selected hole representation with top and bottom view to the 8-hole TS geometry

3.1.2 Computational Grid and Boundary Conditions

Ansys-ICEM CFD mesh generation software is used to create fully hexahedral cells with block structured topology for all geometries. This type of topology is advantageous if both local and global grid refinement is considered to be applied in a parametric way. Hence, it is possible to apply grid refinement with a single scale value in the corresponding refinement zone.

Four computational grids are prepared. The number of cells of the computational domains are also given in Figure 3.9.

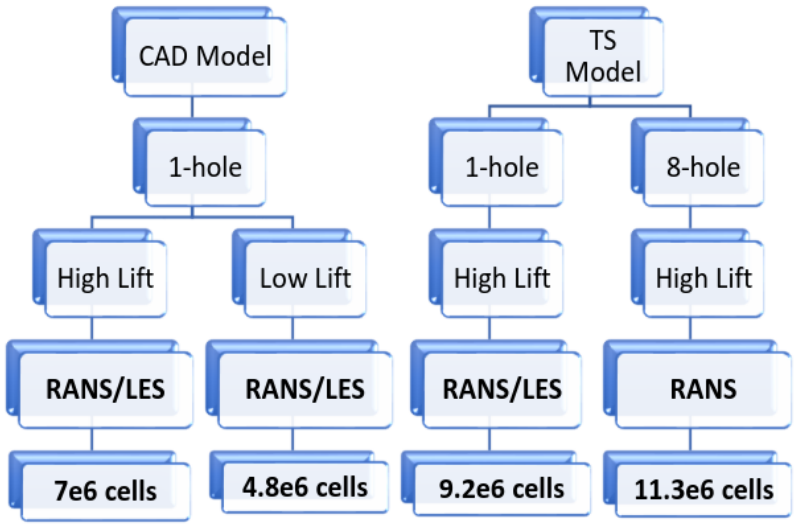

Figure 3.9: Number of cells for the corresponding computational grid

Figure 3.10 shows the block structured topology (left) and grey coloured refinement blocks (right), where high gradients and unsteadiness are expected. Here, the cells within these blocks are divided into half of their cell length for every respective dimensions. The application of the local grid refinement selected blocks resulted with fewer total number of cells for all computational domains. Cut plane of the same topology is presented in Figure 3.11.

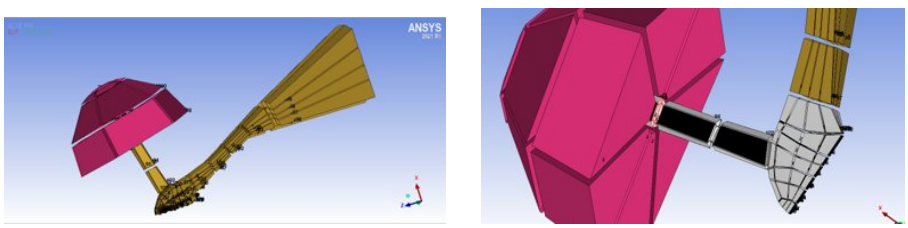

Figure 3.10: 1-hole block structured topology (left) and selected blocks for refinement (right)

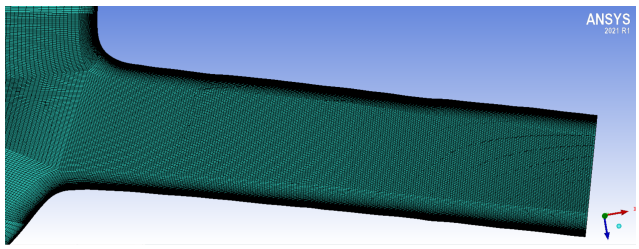

Figure 3.11: Cut plane of the mesh (High lift, 1hole, TS Model)

The computational grid should have sufficient quality due to the spatial resolution requirement of LES. There are couple of approaches to examine whether the computational grid has sufficient quality for LES [38],[39]. In this study, Celik's Index Quality [40] and Taylor length scale calculation are both used for the assessment of grid. It is suggested that by Celik et al. [40] that $LESIQ_v$ of 75% to 85% can be considered adequate for most engineering applications, where

$$LESIQ_v = \frac{1}{1 + 0.05\left(\frac{\mu+\mu_t}{\mu}\right)^{0.053}}. \tag{3.1}$$

Above the equation is used as a post processing parameter to asses the quality of the grid. So, the computational grid has been analysed (Figure 3.12) both globally and locally with several cut planes via $LESIQ_v$ parameter. It can be seen from the Figure 3.12 that the global minimum $LESIQ_v$ value is 0.83 thus the grid is acceptable for LES.

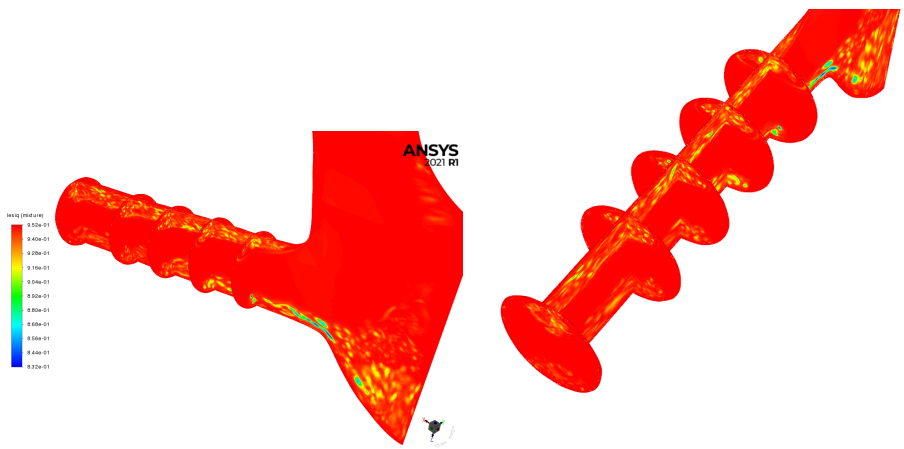

Figure 3.12: Assessment of the grid with $LESIQ_v$ in various cut planes (High lift, 1hole, TS Model)

The Taylor length scale, calculated using the equation $\lambda_g = \sqrt{10}\mathrm{Re}^{-0.5}L$, was taken into account for mesh refinement in different regions of the injector

at both low and high lift positions. The values, as shown in Tables 3.1 and 3.2, indicate the extent of refinement needed to capture the essential flow dynamics within each region, namely the needle seat, sac volume, and orifice.

Table 3.1: Low lift position

	Characteristic Length (m)	**Velocity m/s**	**Reynolds Number**	**Taylor Length Scale (m)**
Needle Seat	2×10^{-6}	700	5000	1×10^{-5}
Sac Volume	~ 0.0004	250	30000	5×10^{-6}
Orifice	0.0003	300	30000	5×10^{-6}

Table 3.2: High lift position

	Characteristic Length (m)	**Velocity m/s**	**Reynolds Number**	**Taylor Length Scale (m)**
Needle Seat	4.8×10^{-6}	200	35000	5×10^{-6}
Sac Volume	~ 0.0008	200	55000	4×10^{-6}
Orifice	0.0003	700	70000	3×10^{-6}

Flow through the geometry is driven via pressure boundary conditions with a purpose of matching experimental conditions. 2200 bar total pressure is set at the inlet, which behaves like a subsonic reservoir boundary condition. Fluctuating velocity at the inlet is not considered, since it does not have any effect on the overall flow field [41]. 10 bar static pressure is given at the outlet surface. It should be noted that the computational domain is extended from the orifice exit to a slightly more downstream position, and outlet ports located at the end of this extension. This extension aims to mitigate the impact of outlet pressure on the upstream flow field. Additionally, during the simulations, cavitation formations have been observed reaching up to the orifice exit in both high and low lift positions.

To reduce the computational cost, the 1/8 portion of the entire injection system is modelled for 1-hole only simulations. Periodicity is provided with periodic boundary conditions that are applied on the side surfaces. Boundary conditions are also represented with different colours in Figure 3.3 and Figure 3.4.

3.2 Dynamic Needle Simulations

There are previous cavitation studies investigating several types of dynamic mesh motion approaches such as Cartesian cut-cell [42], node interpolation [20] and Arbitrary Lagrangian-Eulerian (ALE) [18] methods. To the best of our knowledge, there is no study that applies the overset mesh methodology and examines cavitation erosion for wobbling needle motion. Despite the comparatively high time cost for mesh and topology construction, overset mesh technique is a promising approach as it allows to simulate very low needle positions with non-skewed cells unlike the aforementioned approaches.

Here, needle lift and off-axis motion effects are investigated with the overset mesh methodology This technique employs multiple, overlapping grids that allow for the dynamic simulation of complex movements, such as the needle's wobble and lift in a fuel injector system. The primary advantage of using an overset mesh is its ability to handle the motion of the needle without distorting the computational grid, thereby improving computational efficiency.. To analyze the effect of wobbling motion which is due to the off-axis motion, two cases have been prepared as lift only motion and wobbling motion.

Unlike the static needle simulations, the inlet section of the three-dimensional TS Model is completely closed from the upstream position. The geometrical representation of the studied model is presented in Figure 3.13, below. The moving part here is the needle, colored red, inside the stationary sac, which is colored dark grey. 2200 bar inlet pressure (green surface) and 10 bar static pressure (blue surfaces) conditions are employed and kept constant throughout the dynamic needle simulations. To reduce the computational cost, outlet ports are just located at the orifice exit. Hence, the additional volumes (after orifice exit), which exist in the static needle simulations, are not included in dynamic needle simulations.

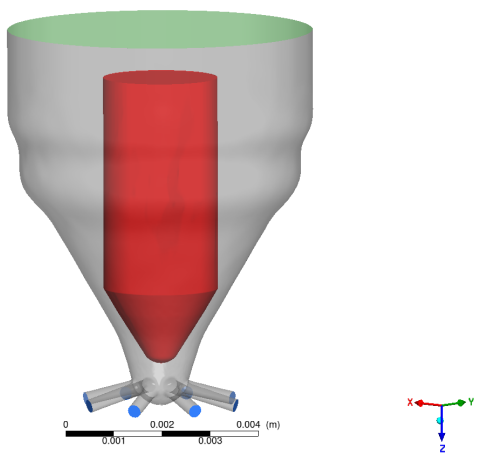

Figure 3.13: Model representation of the dynamic needle simulations

Needle lift and off-axis grid motion profiles, shown in Figure 3.15, are superimposed/adapted from ECN Spray-A wobbling study [42]. The off-axis profile has been slightly changed compared with the reference to set the needle to its initial position.

During the off-axis motion, the needle moves in both the negative y and x directions, following the profile given in Figure 3.15. The direction of the combined off-axis motion is visualized in Figure 3.14 with a red arrow, along with the corresponding hole numbers. Consequently, the needle moves towards the area between hole2 and hole3 with the off-axis motion.

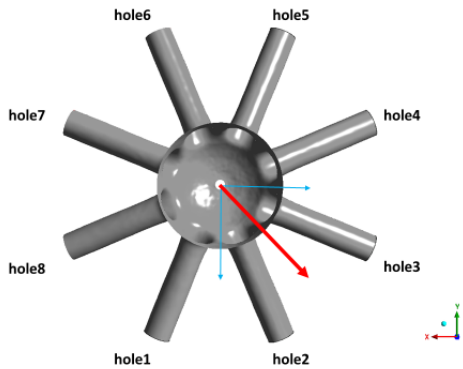

Figure 3.14: Direction of the off-axis motion

For cavitation erosion assessment, lift only motion and wobbling motion configurations are separately simulated during a time of 4000 µs, which corresponds to 2 cycles of the given profiles in Figure 3.15. For lift only motion configuration only the lift profile is employed, while for the wobbling motion both lift and off-axis profiles are imposed together.

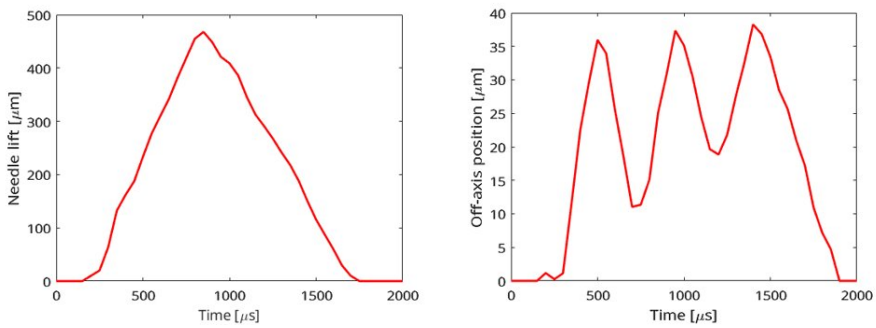

Figure 3.15: Lift (left) and off-axis (right) profiles

At the beginning of the simulation, the needle is seated with 20 µm distance to the sac to achieve simulation times with reasonable level. Cut plane representation of the overset mesh for lowest and highest lift position presented in Figure 3.16. With the overset mesh approach, a dynamic "cutting and blanking" process is continuously employed. As the needle moves, the mesh updates in real-time, ensuring that the overlapping grids accurately reflect the changing geometry. This method is crucial for capturing the needle's motion while maintaining a high-quality mesh in regions of interest.

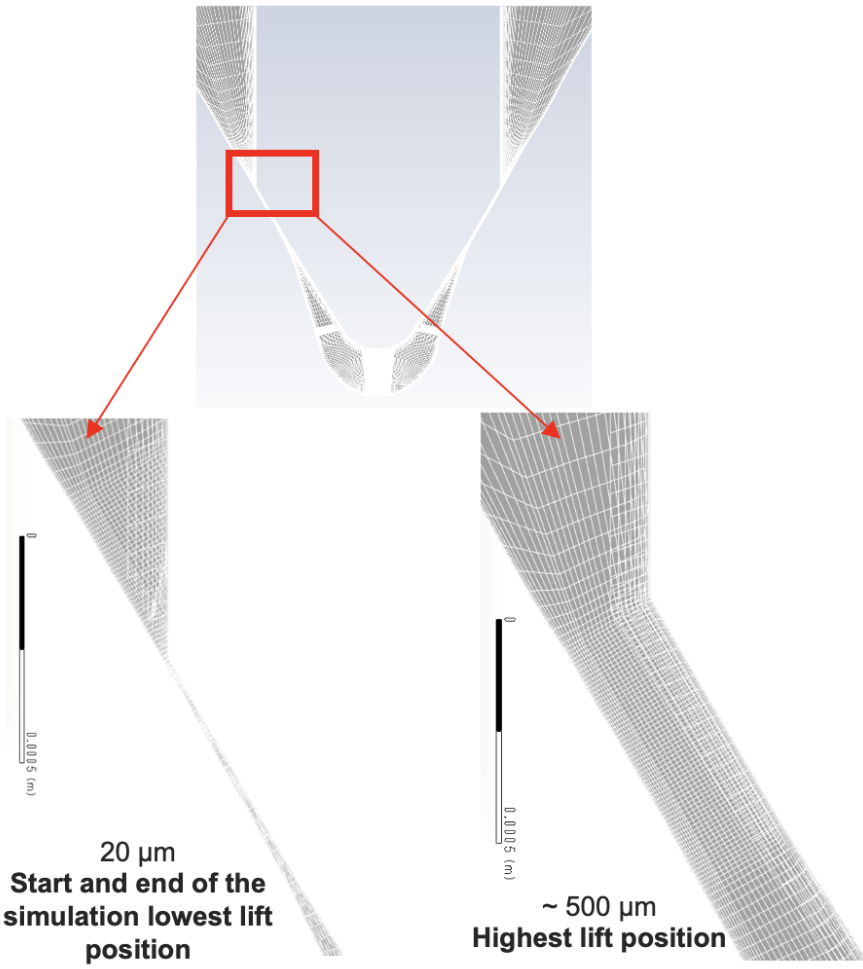

Figure 3.16: Cut plane mesh representation of the overset mesh for lowest and highest lift position

3.3 Numerical Setup

The simulations are performed with the Ansys FLUENT CFD solver. The pressure-based formulation has been used for all studies. Pressure and Velocity are coupled with "Coupled" algorithm, which is known as more robust compared to the segregated algorithms [43].

Pressure equation is discretized with "Body Force Weighted" scheme, while for the momentum equations "Bounded 2^{nd} Order" numerical scheme is used. 2^{nd} Order Upwind scheme is applied to the density, volume fraction and turbulent scalars transport equations.

A residual convergence of 1×10^{-5} for all flow variables was achieved within a maximum of 50 inner iterations. Additionally, the mass transfer rate was used as an extra convergence control parameter, requiring a minimum convergence value of 1×10^{-5} at each time step. Additional simulations were also conducted with a higher convergence criteria of 1×10^{-8} for all flow variables. However, these simulations did not produce any significant differences in the results.

Time is discretized with the 2^{nd} order implicit formulation for static needle simulations. For the dynamic needle simulations 1^{st} order approximation is selected since Ansys FLUENT does not provide higher order time integration schemes for the overset mesh technique.

For static lift simulations, adaptive time stepping is selected. Hence, the CFL number is set to 2 for RANS and 1 for LES simulations. This leads to varying time step around 2 ns for RANS and 1 ns for LES simulations. All flow statistic has been collected at least 5 flow-throughs for each simulation after the initial washout/transients disappeared.

Taking into consideration of excessive cost of the moving mesh simulations, 50 ns of fixed time step has been employed for the dynamic needle simulations. This corresponds to 80000 time steps for each "lift only" and "wobbling motion" simulation setup for the desired 2 cycles of given profiles (Figure 3.15). Before activating the mesh motion, the simulation has been run several flow-thorough with initial low lift condition (20 µm) to get a well evolved flow field.

3.4 Multi-phase Modeling

Assuming a homogeneous mixture environment, multi-phase flow is modelled with "Mixture Model". Liquid and vapor phases behave as they are in local equilibrium over short spatial length scales [43].

The continuity equation for the mixture is given by,

$$\frac{\partial}{\partial t}\left(\rho_m\right) + \nabla \cdot \left(\rho_m \overrightarrow{V_m}\right) = 0, \tag{3.2}$$

where V_m and ρ_m are the mass averaged velocity and mixture density, which are given in detail below. α_k is the volume fraction of phase k,

$$V_m = \frac{\sum_{k=1}^{n} \alpha_k \rho_k \overrightarrow{V_k}}{\rho_m}, \tag{3.3}$$

$$\rho_m = \sum_{k=1}^{n} \alpha_k \rho_k. \tag{3.4}$$

Summation of the individual momentum equation for all phases can represent the momentum equation for the mixture. In the form given below, the effect of gravity and body force are neglected.

$$\frac{\partial}{\partial t}\left(\rho_m \overrightarrow{V_m}\right) + \nabla \cdot \left(\rho_m \overrightarrow{V_m}\overrightarrow{V_m}\right) = -\nabla p + \nabla \cdot \left[\mu_m \left(\nabla \overrightarrow{V_m} + \nabla \overrightarrow{V_m^T}\right)\right] \quad (3.5)$$

Here, μ_m is the viscosity of the mixture and given by,

$$\mu_m = \sum_{k=1}^{n} \alpha_k \rho_k \ . \quad (3.6)$$

Although there are elevated temperature rises during a cavitation collapse event, time and length scale of these instances are limited and it has a negligible effect on the global fluid properties [44]. So, it should be noted that the effect of temperature is not taken into consideration. Hence, the energy equation is not being solved.

3.5 Cavitation Modeling

Vapor transport equation relates mass transfer between the liquid and vapor phases with the equation,

$$\frac{\partial}{\partial t}\left(\alpha\ \rho_v\right) + \nabla \cdot \left(\alpha\ \rho_v\ \overrightarrow{V_v}\right) = R_e - R_c. \quad (3.7)$$

Here, ρ_v is vapor density, α is vapor volume fraction, and $\overrightarrow{V_v}$ represents vapor phase velocity field. R_e and R_c are the mass transfer source terms, which represent evaporation and condensation, respectively.

Zwart-Gerber-Belamri (ZGB) model is selected to model mass transfer. The ZGB model uses the following rates of mass transfers, first described by Zwart et al [45]:

$$\text{if } \ P \leq P_v: \qquad R_e = F_v \frac{3\alpha_{nuc}\left(1-\alpha_v\right)\rho_v}{R_b}\sqrt{\frac{2}{3}\frac{P_v - P}{\rho_l}}, \quad R_c = 0, \quad (3.8)$$

$$\text{if } \ P \geq P_v: \qquad R_c = F_c \frac{3\alpha_{nuc}\ \alpha_v\ \rho_v}{R_b}\sqrt{\frac{2}{3}\frac{P - P_v}{\rho_l}}, \quad R_e = 0. \quad (3.9)$$

The default mass transfer rate constants are provided in Table 3.3. Additional sensitivity simulations (Section 3.9) have been carried out to see the effect of different evaporation and condensation coefficients.

Table 3.3: ZGB Mass transfer coefficients

Description of the coefficient	Numerical value
R_b: Bubble radius [m]	1×10^{-6}
α_{nuc}: Nucleation site volume fraction	5×10^{-4}
F_v: Evaporation coefficient	50
F_c: Condensation coefficient	0.01
P_v: Vaporization pressure [Pa]	6000

3.6 Thermodynamic Modeling

Diesel is modelled as a compressible liquid and represented with the Tait equation. The barotropic formulation enables to model the liquid phase without nonphysical pressure spikes under high-pressure conditions. It is represented as in the simplified form with the following set of equations [43]:

$$\left(\frac{\rho}{\rho_0}\right)^n = \frac{K}{K_0} \tag{3.10}$$

$$K = K_0 + n\Delta p \tag{3.11}$$

$$\Delta p = p - p_0. \tag{3.12}$$

Relevant description of the parameters and values are given in Table 3.4. Diesel vapor is modelled as an incompressible fluid with physical properties given in Table 3.5 below. Although the vapor phase is incompressible, the mixture still can be considered as compressible [46].

Table 3.4: Diesel liquid properties

Description	Value
p_0 = Reference Pressure [Pa]	0
ρ_0 = Reference Density [kg/m^3]	771.13
K_0 = Reference Bulk Modulus [Pa]	8.179023×10^8
n = Density Exponent	7.15
Max. Density Ratio Limit	5
Min. Density Ratio Limit	0.1

Table 3.5: Diesel vapor properties

Description	Value
Density [kg/m^3]	0.89457
Viscosity [kg/(ms)]	8×10^{-6}

3.7 Turbulence Modeling

3.7.1 RANS $k-\omega$ SST Model

The shear-stress transport $k-\omega$ turbulence model ($k-\omega$ SST) [35] is employed within unsteady (RANS) formulation. It effectively blends $k-\omega$ and $k-\epsilon$ model, in the regions of near-wall and free-stream, respectively. Hence, robustness and accuracy are provided with the help of blending function [43].

A special treatment is applied to the turbulent viscosity, μ_t, which is previously proposed by Reboud et al. [37]. It is an *ad hoc* method to reduce eddy viscosity in the mixture to allow for a more dynamic flow behaviour. The correction is expressed as

$$\mu_t = \frac{\rho^{'} k}{\omega} \frac{1}{\max\left[\frac{1}{\alpha^*}, \frac{S\ F_2}{a_1 \omega}\right]}, \tag{3.13}$$

$$\rho^{'} = \rho_v + \frac{(\rho_m - \rho_v)^n}{(\rho_l - \rho_v)^{n-1}}, \tag{3.14}$$

$$\rho_m = \alpha \rho_v + (1-\alpha)\rho_l. \tag{3.15}$$

Here, the proposed density function $\rho^{'}$ returns a value in the mixture, including the corresponding phase contributions. In this way, high values of the turbulent viscosity is prevented and an unsteadiness of cavitation is achieved [47]. Effect of this correction is also particularly investigated within the concept of sensitivity analysis in Section 3.9.

This correction is applied via User Defined Function (UDF) implementation.

3.7.2 LES Wale Model

In the Wall-Adapting Local Eddy-Viscosity (WALE) model [36] the turbulent viscosity, μ_t, is expressed as

$$\mu_t = \rho L_s^2 \frac{\left(S_{ij}^d S_{ij}^d\right)^{3/2}}{\left(\overline{S}_{ij}\overline{S}_{ij}\right)^{5/2} + \left(S_{ij}^d S_{ij}^d\right)^{5/4}}. \tag{3.16}$$

Here, ρ represents the density, L_s denotes the mixing length for subgrid scales, S_{ij}^d is the modified rate-of-strain tensor, S_{ij} corresponds to the resolved rate-of-strain tensor, and $\overline{S}_{ij}$ is the rate-of-strain tensor for the resolved scale.

$$S_{ij}^d = \frac{1}{2}\left(\overline{g}_{ij}^2 + \overline{g}_{ji}^2\right) - \frac{1}{3}\delta_{ij}\overline{g}_{kk}^2, \tag{3.17}$$

$$\overline{g}_{ij} = \frac{\partial \overline{u}_i}{\partial x_j}, \tag{3.18}$$

$$\overline{S}_{ij} = \frac{1}{2}\left(\frac{\partial \overline{u}_i}{\partial x_j} + \frac{\partial \overline{u}_j}{\partial x_i}\right). \tag{3.19}$$

The mixing length, L_s, in the WALE model is determined using

$$L_s = \min\left(\kappa d, C_w V^{1/3}\right). \tag{3.20}$$

Within this equation, κ represents the von Kármán constant, d is the distance to the closest wall, C_w stands for the WALE constant (with a default value of 0.325), and V denotes the volume of the computational cell.

3.8 Cavitation Erosion Modeling

To examine the effect of the cavitation erosion, four variables are tracked each time step. These variables are pressure (P), material derivative of pressure divided by cell volume $(DP/Dt)/V_{cell}$, square of material derivative of pressure $(DP/Dt)^2$ and second derivative of potential power density ($PPD2$). For the effective analysis of these variables, a User-Defined Function (UDF) implementing MAX1 and MAX2 algorithms is utilized. The MAX1 algorithm focuses on identifying the maximum value of the tracked parameters, providing a simplified yet insightful view into the peak conditions that may lead to erosion. Conversely, the MAX2 algorithm offers a more nuanced approach, considering the prevention of the fake collapses due to the surrounding cells and applying specific criteria to identify potential cavitation collapse cells. This dual-algorithm approach enables a robust examination of cavitation phenomena, offering insights into both the instantaneous and evolving conditions that contribute to erosion.

3.8.1 Tracked Variables

1. Pressure (scaled with V_{cell}/V_{ref})

   - This variable represents the pressure within the system, scaled with the ratio of cell volume to reference volume. The reason behind this scaling is to prevent linear dependency of maximum pressure with the relevant cell size [6]. Pressure serves as a fundamental parameter in assessing cavitation erosion, as it directly influences the formation and collapse of vapor structures.

2. Material Derivative of Pressure divided by Cell Volume: $(DP/Dt)/V_{cell}$

   - This variable quantifies the material derivative of pressure divided by the cell volume itself. The material derivative provides insights into the rate of change of pressure over time, offering valuable information about the occurrence and intensity of cavitation erosion. Material derivative is given by,

$$\frac{DP}{Dt} = \frac{\partial P}{\partial t} + U \cdot \nabla P. \tag{3.21}$$

3. Square of Material Derivative of Pressure: $(DP/Dt)^2$

   - This variable represents the square of the material derivative of pressure, reflecting the magnitude of pressure fluctuations. Monitoring the squared material derivative helps us understand the intensity and rapid changes in pressure, which are linked to cavitation erosion.

4. Second Derivative of Potential Power Density [24] : $PPD2$

   - It measures the second derivative of potential power density, indicating the rate of change of power density with respect to pressure. This variable provides insights into the energy transfer and potential for damage caused by cavitation erosion and given by,

$$PPD2 = (p_v - P)\frac{\rho}{\rho_l - \rho_v}\nabla \cdot \mathbf{U} \quad . \tag{3.22}$$

3.8.2 Tracking Methodologies: MAX1 and MAX2 algorithm

To capture the behaviour of these variables, a post-processing User-Defined Function (UDF) was implemented. There are two sets of algorithms, MAX1 and MAX2, implemented. MAX1 is already studied by previous researchers [21], [23]. In MAX1 algorithm, only the maximum value of the tracked parameter (Table 3.6) is considered. MAX2 algorithm relies on the prevent mechanism of the fake collapses. The idea has been first introduced by Mihatsch et al. [48] and then it has been reformulated by Mouvanal [34].

Table 3.6: Description of the variables in MAX1 algorithm

Description	Value
Tracked parameter at current time step	F_{t_n}
Tracked parameter at previous time step	$F_{t_{n-1}}$

Figure 3.17: MAX1 algorithm

The MAX2 algorithm loops over all cells at the end of each time step. There are 3 conditions that need to be satisfied to determine the cell as the "collapse cell". These conditions are listed in Figure 3.18.

First condition is necessary to distinguish whether there are transported vapor clouds from neighbouring cells. Moreover, collapse due to the rebound is particularly examined with zero vapor volume fraction . This procedure has been first used by Mihatsch et. al [48] with a density-based solver.

Second condition is checking the tracked parameter value of the current time step with the previous time step, with a physical insight that a collapse will occur with a higher tracked parameter value. Mouvanal [34] set this tracked parameter as pressure, solely. In this study, additional tracked parameters ($(DP/Dt)/V_{cell}$, $(DP/Dt)^2$, $(PPD2)$) are introduced alongside with the Pressure (P). Finally, third condition ensures that a condensation happened in that cell.

So, once these 3 conditions are satisfied in that loop, maximum value for the each tracked parameter is updated within a cell loop that works at the end of each time step using UDF.

Volume fraction of 2 previous time step	$\alpha_{t_{n-2}}$	Condition1 $\alpha_{t_{n-2}} > 0$ $\alpha_{t_{n-1}} = 0$ $\alpha_{t_n} = 0$	If 3 conditions are satisfied ⬇ Update maximum value for the tracked parameter
Volume fraction of previous time step	$\alpha_{t_{n-1}}$		
Volume fraction of current time step	α_{t_n}		
Tracked parameter at current time step	F_{t_n}	Condition2 $F_{t_n} > F_{t_{n-1}}$	
Tracked parameter at previous time step	$F_{t_{n-1}}$		
Mass transfer rate	R	Condition3 $R < 0$	

Figure 3.18: MAX2 algorithm and description of the variables

3.9 Sensitivity Analysis

In this section, sensitivity simulation are carried out by taking into consideration of first mass transfer rate coefficient and Reboud's Correction with a base computational mesh "Grid1" with 1.1×10^6 cells. Then, the analysis has been further expanded to provide grid independent solution by locally refine the grid via block refinement approach, constructed "Grid2" with 4.8×10^6 cells.

Here, the static high lift condition is examined with aforementioned RANS turbulence modelling.

3.9.1 Mass transfer rate and Reboud's Correction

A sensitivity analysis was conducted to evaluate the effects of mass transfer rate coefficients and Reboud's Correction. By increasing evaporation and condensation coefficients and by selectively applying turbulent viscosity correction, the analysis isolates the impact of these factors while holding other parameters steady. The setup configurations for this analysis, including the variations in ZGB coefficients and the application of Reboud's Correction, are detailed in Table 3.7.

Table 3.7: Configuration of sensitivity analysis

Simulations	ZGB Coefficients	Reboud's Correction
Setup1	Default	No
Setup2	Default	Yes
Setup3	$10F_e$, $10F_c$	No
Setup4	$10F_e$, $10F_c$	Yes
Setup5	$100F_e$, $100F_c$	No
Setup6	$100F_e$, $100F_c$	Yes

Figure 3.19 and Figure 3.20 represent the MAX2 pressure distribution on the orifice nozzle wall for the corresponding configurations.

Two important outcomes can be deduced from the simulations:

- Reboud's correction plays a key role in the distribution of MAX2 pressure. A comparison between Figure 3.19 and Figure 3.20 indicate that without Reboud's correction, the observed experimental patterns are not replicated. This discrepancy can be attributed to the dynamic behavior of the cavity which must be captured in the simulation to assess erosion risk adequately.

- Increasing the ZGB coefficients results in a better correlation with experimental data. Setups 4 and 6, in particular, show good agreement with experimental observations when higher magnitude pressure cells, indicative of erosion regions in experiments are present. Higher coefficients bring the mass transfer model closer to a barotropic relationship, and this seems to enhance the condensation rate, which is crucial for accurately simulating cavitation behavior.

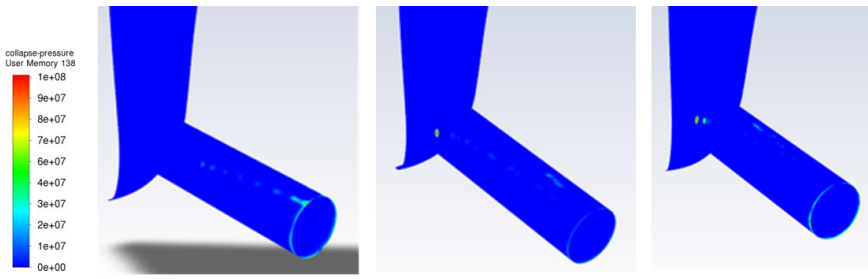

Figure 3.19: MAX2 P [Pa] contour on orifice for Grid1. From left to right, Setup1 (Default F_e and F_c), Setup3 ($10F_e$ and $10F_c$) and Setup5 ($100F_e$, $100F_c$)

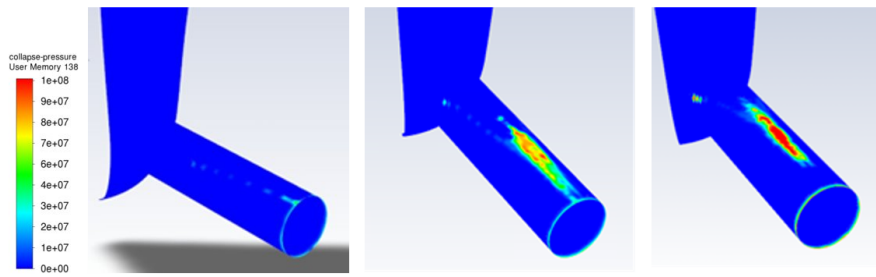

Figure 3.20: MAX2 P [Pa] contour on orifice for Grid1. From left to right, Setup2 (Default F_e and F_c), Setup4 ($10F_e$ and $10F_c$) and Setup6 ($100F_e$, $100F_c$)

3.9.2 Reproducibility of configurations with grid refinement

The configurations Setup4 and Setup6 are further simulated with a refined grid, Grid2. The purpose of this additional investigation is to achieve a consistent solution alongside the chosen configuration set. MAX2 pressure distribution on the orifice wall is presented in Figure 3.21.

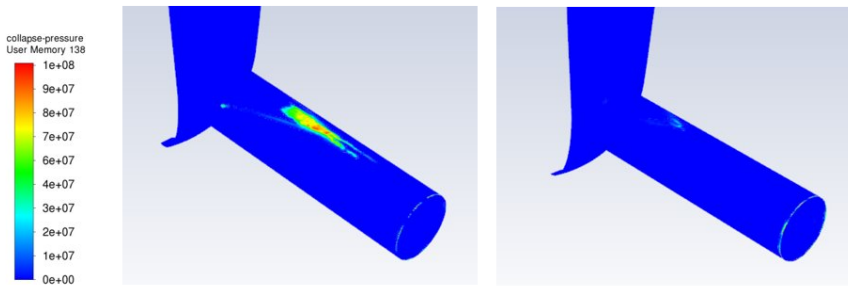

Figure 3.21: MAX2 P [Pa] contour on orifice for Setup4 (left) and Setup6 (right) - Grid2

Direct comparison of Figure 3.20 and Figure 3.21 shows the effect of local grid refinement for each configuration. It can be concluded that a similar collapse distribution can be achieved with Setup4. However, grid refinement on Setup6 resulted in a completely different distribution.

ZGB coefficients set for Setup6 are 10 times higher than for Setup4. Increasing mass transfer coefficients promises asymptotic behavior which moves the phase change process closer to thermodynamic equilibrium [46]. However, once the mass transfer coefficients are increased, a high level of numerical instability is introduced to the simulations. In transient simulation, these sudden numerical instabilities can contaminate the instantaneous flow field, and they can be challenging to eliminate, even when instabilities are suppressed with under-relaxation parameters. Hence, Setup4 configuration is considered to be sufficient for this study.

Therefore, ZGB coefficients 10 times greater have been applied to all RANS and LES simulations, and Reboud's correction has been enabled for all RANS simulations.

Chapter 4

Results

4.1 Static Needle Results

In this subsection, the results obtained from the static needle simulations are presented. For the high lift needle position, the results are first organized into CAD Model and TS Model results, then each design's different turbulence modeling performance (RANS and LES) is presented. To analyze the identical surface characteristics of each hole, an 8-hole TS Model result is provided in high lift position. Furthermore, the performance of the turbulence model is also investigated for the low lift needle position, featuring only CAD Model surfaces.

For each simulation configuration, first the flow statistics are introduced, then the turbulent structures are presented alongside the vapor formations. Each subsection is then concluded with erosion assessment results.

4.1.1 CAD Model

4.1.1.1 High lift, RANS, 1-hole

The vapor volume percentage change in time for this configuration is presented in Figure 4.1, which presents a low magnitude oscillatory pattern in vapor volume throughout the selected time interval. This type of locally dynamic cavitation process is mainly due to the attached sheet cavity on the top side of the injector. This vapor formation is presented with volume fraction (α) iso-vapor surfaces in Figure 4.2 (left) alongside with the turbulent structures, created by iso-surfaces of λ_2 criterion. It is clearly seen that the attached sheet cavity is split into two cores, as observed by the previous studies [49],[50] in similar conditions. Here, the vapor starts to form near the orifice inlet due to the surface curvature and it has an overall smooth shape except the region, where coherent turbulent structure exist in more downstream position of the inlet and extends to the middle of the orifice. There are also turbulent structures on the bottom side of the orifice inlet, but these are not strong enough to create low pressure regions, hence cavitation.

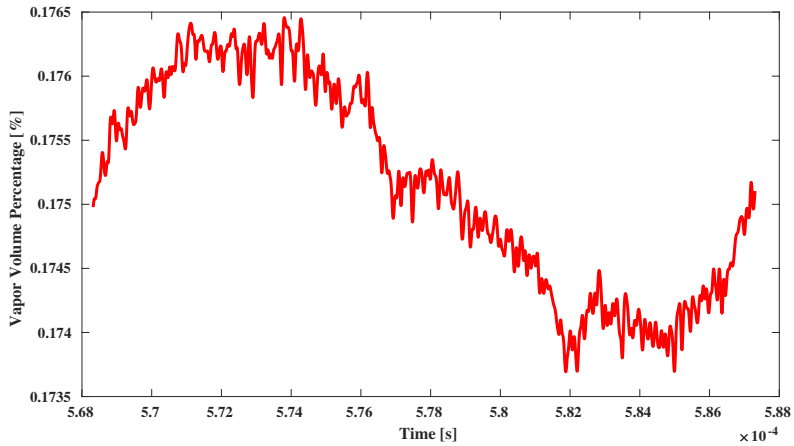

Figure 4.1: Vapor volume percentage change in time

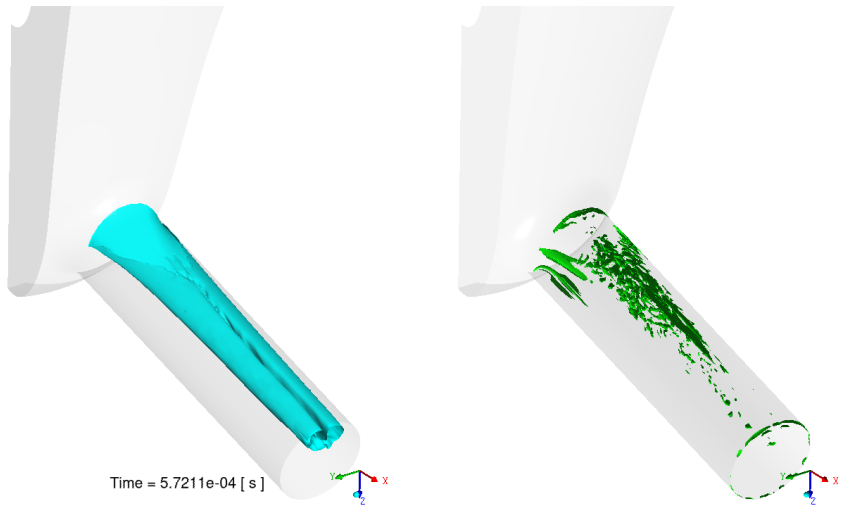

Figure 4.2: Vapor formations ($\alpha = 0.5$) and turbulent structures ($\lambda_2 = 5 \times 10^{13}$) - CAD Model, high lift, RANS

Figure 4.3 presents spatial mass transfer rate distribution on the orifice walls and cut plane volume fraction together with the surface mesh representation of the CAD Model. As previously mentioned, the vapor generated near the orifice inlet can be identified here as well with red colored mass transfer rate contour values on the wall. In more downstream position, where the turbulent activity is high (see Figure 4.2 - right), both vapor generation and condensation patterns are present. It is also clear from the cut plane volume fraction that the vapor is separated from the top side of the orifice and convected downstream.

The force history across the entire injector walls (needle, needle seat and

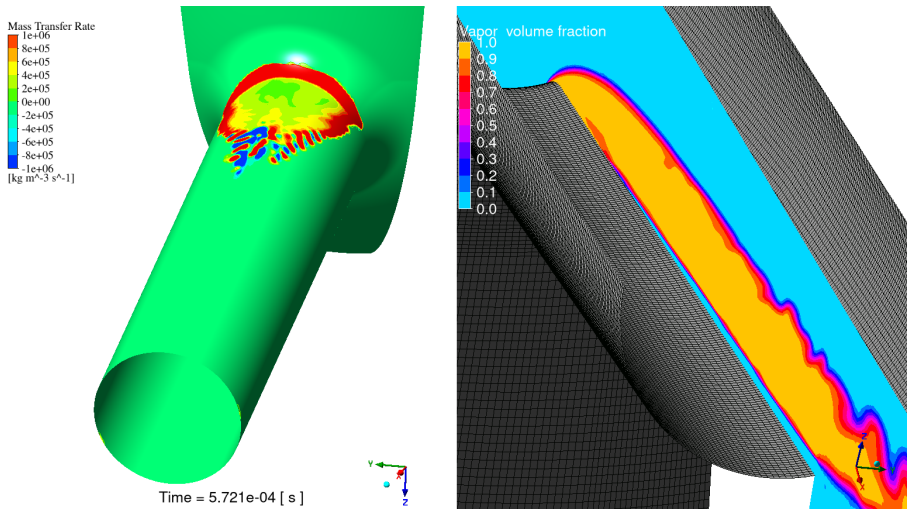

Figure 4.3: Mass Transfer Rate contour plot on the walls (left) and CAD Model surface mesh representation with cut plane volume fraction (right)

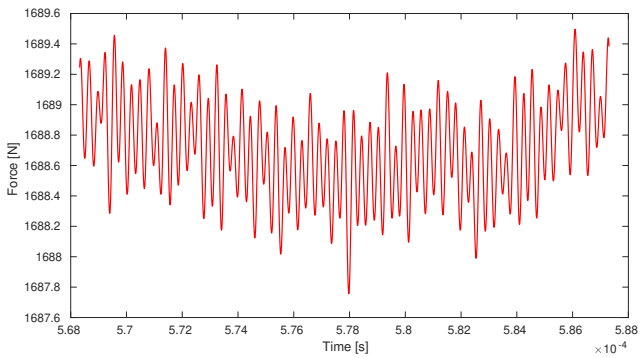

Figure 4.4: Force plot history of the overall injector wall surfaces

orifice) is depicted in Figure 4.4. The relative change in force is very small since the pressure integration surfaces covers the entire injector walls. Nevertheless, there are still unsteady dynamics visible, as also shown in Figure 4.1.

Erosion assessment using the MAX1 and MAX2 algorithms are illustrated in Figure 4.5 and Figure 4.6, respectively. Here, it should be mentioned that red colored region is a candidate for the high risk of cavitation erosion.

Orifice entrance is the region where the flow is constricted by a reduced cross-sectional area with respect to the upstream sac volume/cavity. This constriction leads to a reduction in flow velocity, causing the kinetic energy of the fluid to be converted into pressure energy. This increase in pressure referred to as a stagnation pressure rise and it exists over the orifice entrance. It is possible to see this stagnation pressure effect on all erosion indicators with

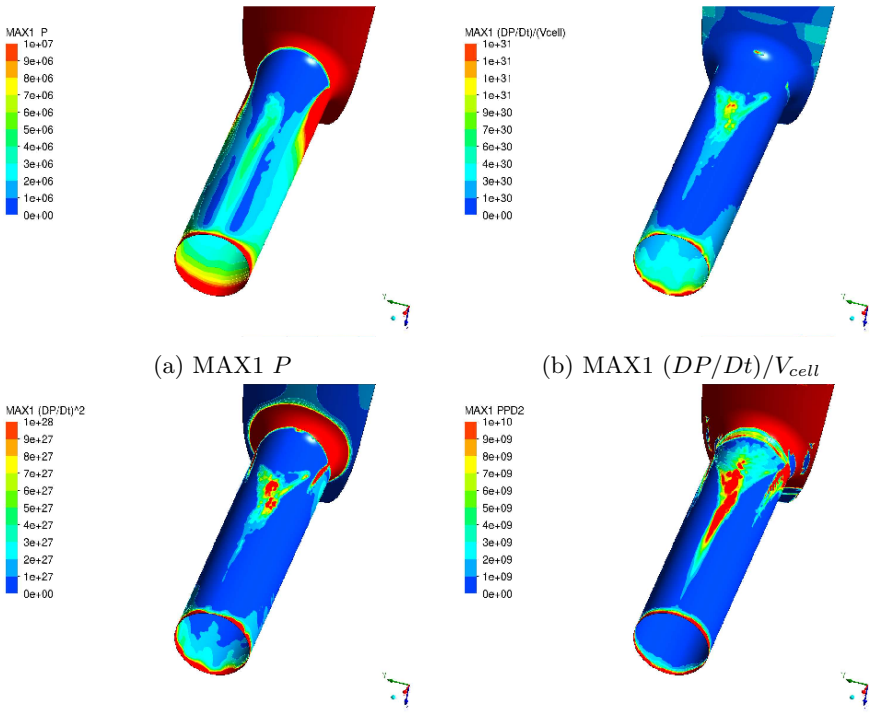

(a) MAX1 P

(b) MAX1 $(DP/Dt)/V_{cell}$

(c) MAX1 $(DP/Dt)^2$

(d) MAX1 $PPD2$

Figure 4.5: Erosion assessment results - CAD Model, high lift, RANS

MAX1 algorithm in Figure 4.5, whereas for MAX2 algorithm in Figure 4.5 this effect has been overcome with the help of additional conditions in MAX2 algorithm. Apart from this effect, for both algorithms $(DP/Dt)^2$ and $PPD2$ erosion indicator patterns are located at the top side of the orifice as observed in high lift experiments (Figure 2.1). However, the length of the erosion pattern in simulations are much shorter compared to the experiments.

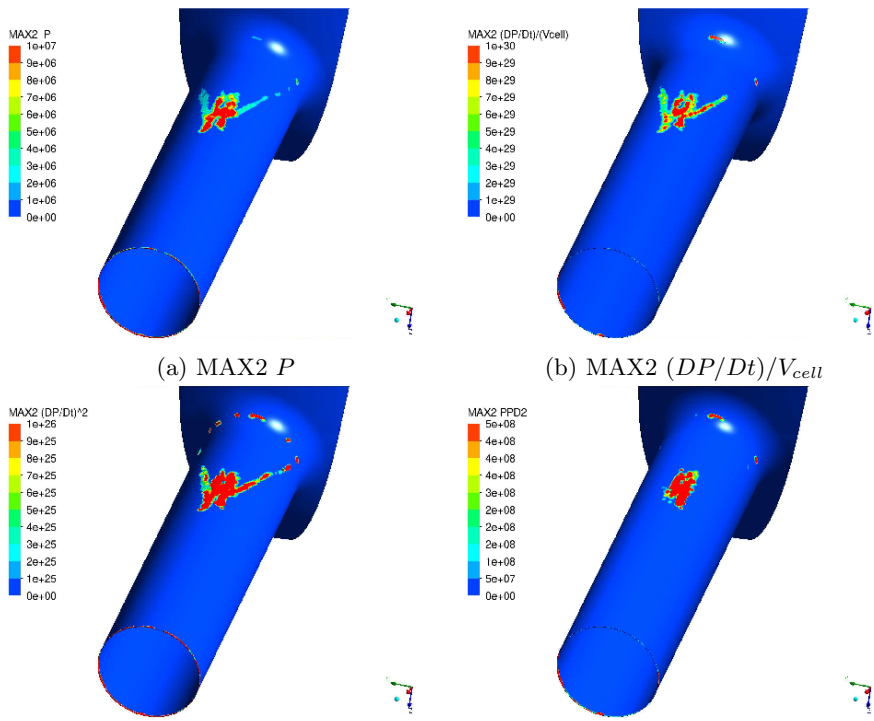

(a) MAX2 P

(b) MAX2 $(DP/Dt)/V_{cell}$

(c) MAX2 $(DP/Dt)^2$

(d) MAX2 $PPD2$

Figure 4.6: Erosion assessment results - CAD Model, high lift, RANS

4.1.1.2 High lift, LES, 1-hole

The plot presented in Figure 4.7 exhibits a more random pattern in the vapor volume change over time compared to RANS results, which is in line with ability with the ability of the LES model to capture larger and more dynamic range of eddies and flow structures. The significant difference between global minimum (t1) and maximum (t3) suggests the presence of additional cavitation structures.

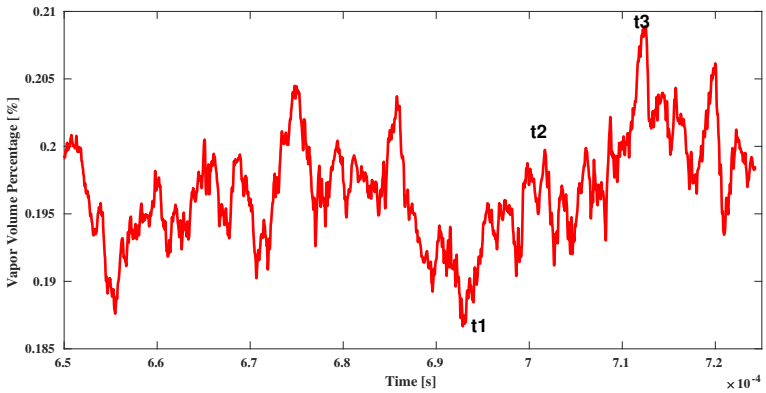

Figure 4.7: Vapor volume percentage change in time

The transient nature of cavitation and its interaction with the turbulent flow within the injector is show in Figure 4.8 for three time instants (t1, t2, t3). As observed in Figure 4.7, overall vapor structures show more dynamic behavior, unlike the RANS results. On the bottom half of the orifice, vortex cavitation is present and it grows and changes its shape over time. This structure was not present in the RANS results. The general form of the top side vapor formation is almost similar with the RANS results, hence it is split in two parts. The attachment region surface between the attached sheet cavity and (top side) orifice wall shows more intermittent behavior as the flow progress in downstream position.

Turbulent structures (λ_2 criterion) on the right side of the Figure 4.8 reveals more information about the attached cavity region. High shear activity in that region between the vapor and liquid is present in all time instants. Besides that there are two additional turbulent structures visible: One is in the orifice bottom side near inlet which is mainly responsible of generating the bottom side vapor structures by creating low pressure regions. The other one stays inside the sac region and is basically a part of the re-circulation region, which is more clearly seen from the right side of the Figure 4.10. On the left side of this figure, high vorticity regions correlate with zones of intense turbulence and cavitation structures.

Figure 4.10 presents spatial mass transfer rate distribution on the orifice walls and cut plane volume fraction together with the surface mesh representation. Both of the results shows quite similar patterns with RANS. It should

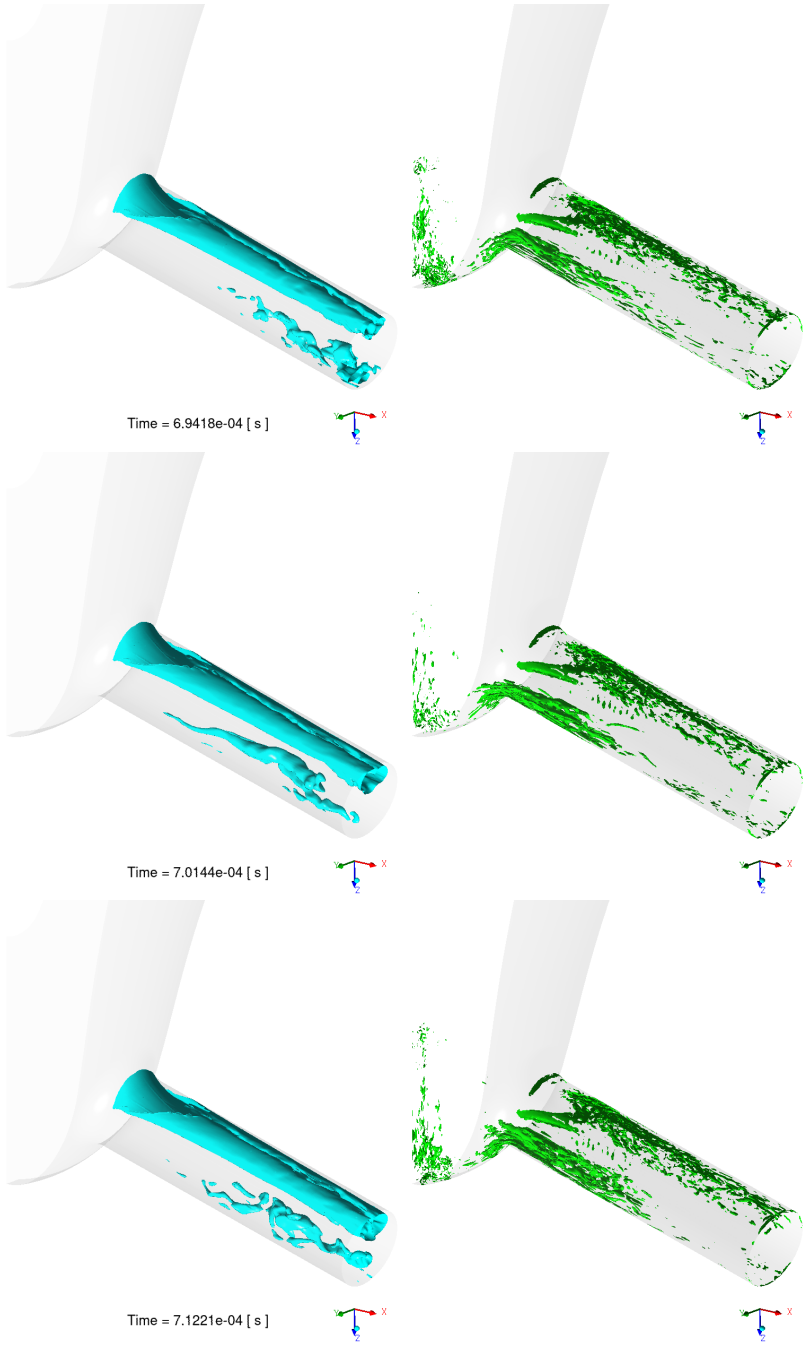

Figure 4.8: Vapor formations ($\alpha = 0.5$) and turbulent structures ($\lambda_2 = 5 \times 10^{13}$) t1, t2, t3 - CAD Model, High lift, LES

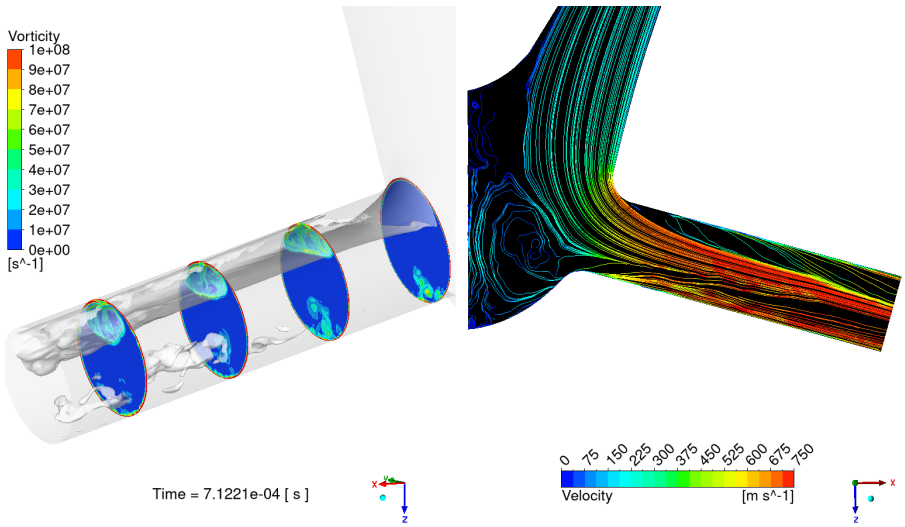

Figure 4.9: Vorticity fields on cross section cut planes together with transparent vapor structures (left) and velocity colored streamlines on injector mid-plane (right)

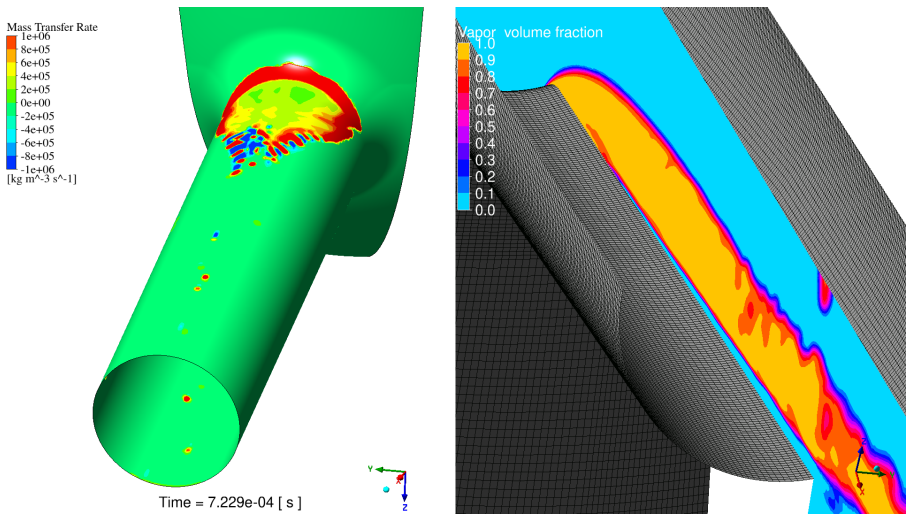

Figure 4.10: Mass Transfer Rate contour plot on the walls (left) and CAD Model surface mesh representation with cut plane volume fraction (right)

be noted here that the cut plane on the right side of Figure 4.10 is limited up to the half of the whole orifice. Hence, this is why the bottom side vapor formations are not completely visible.

The force plot history of the overall orifice surfaces, depicted in Figure 4.11, displays more pronounced fluctuations with broader ranges compared

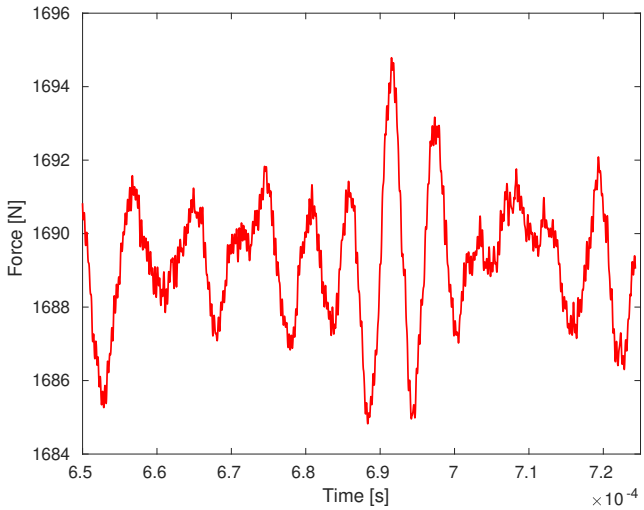

Figure 4.11: Force plot history of the overall orifice surfaces

to the RANS results. The distinction mainly arises from having additional cavitation dynamics and vapor structures in the LES model. The presence of vapor formations along the wall creates regions of low pressure, which are reflected in the force calculations as low values. Conversely, when these vapor structures collapse, they result in high-pressure spikes.

Erosion assessment using the MAX1 and MAX2 algorithms are illustrated in Figure 4.12 and Figure 4.13, respectively. Stagnation effects are still present near the orifice entrance in MAX1 algorithm for all erosion indicators. While for the MAX2, these effects are not present and cavitation erosion risk is more localized over the top and bottom of the orifice wall. Here, only the indicator "MAX2 P" (Figure 4.13) differentiate from others via suggesting that the risk is higher on the top side than the bottom side of the orifice. In experiments, only the top side of the orifice is expected to be eroded along the orifice length. The extent of the erosion pattern in these results is much longer when compared with RANS results (Figure 4.6). Therefore, for this specific region, LES performs better than RANS.

The bottom side erosion pattern for LES in both MAX1 and MAX2 is mainly due to the collapse of the vortex cavitation formations at the bottom half side of the orifice. There is no further information from the experiments if the bottom side vapor formation is physical or not. This will be elaborated more in upcoming sections.

Apart from the bottom side erosion pattern and stagnation effect, material derivative formulated erosion indicators $(DP/Dt)/V_{cell}$ and $(DP/Dt)^2$ in MAX1 predict well the erosion pattern on the top side of the orifice. For all indicators in MAX2, there is a clear erosion pattern on the top side of the of the orifice that agrees well with experiments.

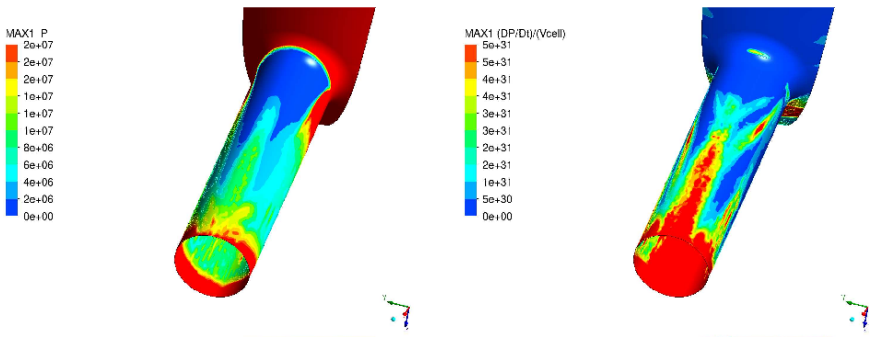

(a) MAX1 P

(b) MAX1 $(DP/Dt)/V_{cell}$

(c) MAX1 $(DP/Dt)^2$

(d) MAX1 $PPD2$

Figure 4.12: Erosion assessment results - CAD Model, high lift, LES

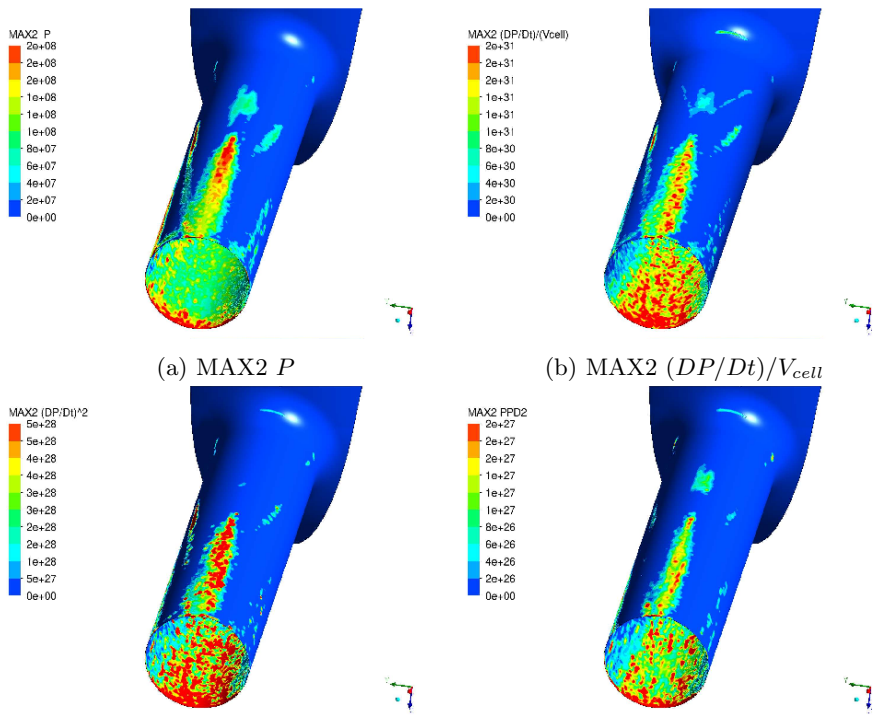

(a) MAX2 P

(b) MAX2 $(DP/Dt)/V_{cell}$

(c) MAX2 $(DP/Dt)^2$

(d) MAX2 $PPD2$

Figure 4.13: Erosion assessment results - CAD Model, high lift, LES

4.1.1.3 Low lift, RANS, 1-hole

Figure 4.14 presents the vapor volume percentage change in time for the low lift condition. At time instant t1 the amount of the total vapor volume is largest and there should be less amount of vapor inside the whole injector at t2 and t3 time instants. Here, three time instants are presented in Figure 4.15 with snapshots of vapor formations and turbulent structures.

For all time instants vapor forms in two distinct regions; one stands between the needle and the needle seat, characterized by shedding patterns, and the other one is inside the orifice, where larger, more stable vapor structures are observed. In Figure 4.14, the total vapor volume in the whole injector is recorded. So it is challenging to determine which vapor formation did change its shape from t1 to t2.

The identified turbulent structures within the region of dominant shedding vapor formations suggest a significant level of shear activity. This finding aligns with previous research on low lift conditions [18], [46] , which has similarly highlighted the presence of intense shear forces in these regions.

Before presenting assessment results it is worthwhile to mention that the examination of whole injector geometry is split into two parts as needle and sac (orifice included) surfaces. This is because the fact that both needle and orifice entrance seem to be eroded at the end of the experiment (Figure 2.2). The progression of the erosion pattern is not taken into consideration, since having the total simulation time as in the experiment is unrealistic. Additionally, the initial geometry changes during the experiment.

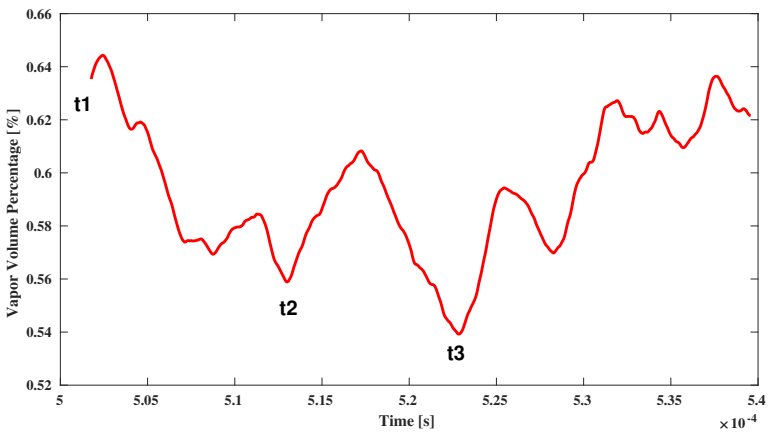

Figure 4.14: Vapor volume percentage change in time

The numerical cavitation erosion assessment with both MAX1 and MAX2 algorithms on the needle surface is given in Figure 4.16 and 4.17 respectively. MAX1 algorithm still suffers from the high stagnation value in upstream needle surfaces. Similarly as in high lift simulations, material derivative indicators are more successful than the others, especially $(DP/Dt)^2$. The erosion pattern given in the bottom left image in the Figure 4.16 agrees well with low lift

erosion experiments. The repetitive pitting behavior forms in a distinctive way in localized regions in MAX2 for all indicators. Hence, a sharper contrast is generated between the eroded and non-eroded region. However, in MAX1, the pitting behavior is more scattered due to the transportation of the surrounding vapor collapses.

For the sac and orifice part, the numerical cavitation erosion assessment with both MAX1 and MAX2 algorithms is given in Figure 4.18 and 4.19 respectively. Two important conclusions can be deducted from the low lift experiments (Figure 2.2). One is that there is an erosion pattern that starts from near the orifice inlet and reaches an upstream position in the needle seat. The second consideration is that, there should not be any damage on the orifice wall (especially in downstream positions).

In MAX1 (Figure 4.18), the predicted damaged location is almost identical for all erosion indicators, but that location stand more upstream than in the experiments. There are also signs of damages in on the top of the orifice, but they are low in magnitude. In MAX2, the erosion patterns are more localized but located in the same region as with MAX1.

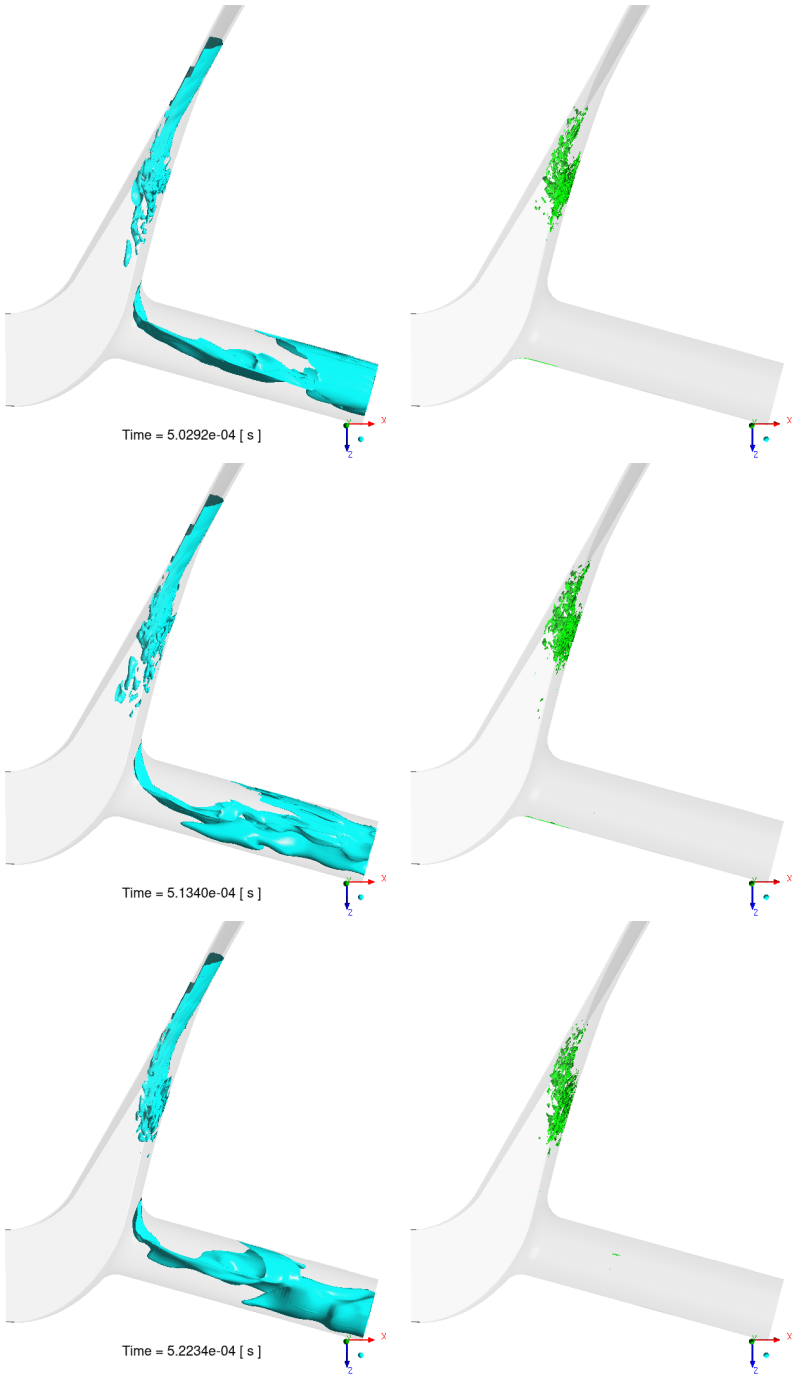

Figure 4.15: Vapor formations ($\alpha = 0.5$) and turbulent structures ($\lambda_2 = 5 \times 10^{13}$) t1, t2, t3 - CAD Model, low lift, RANS

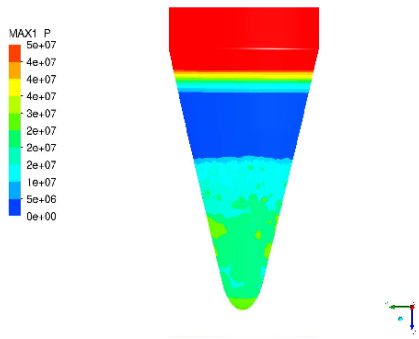

(a) MAX1 P

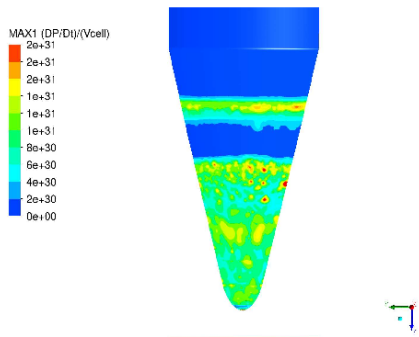

(b) MAX1 $(DP/Dt)/V_{cell}$

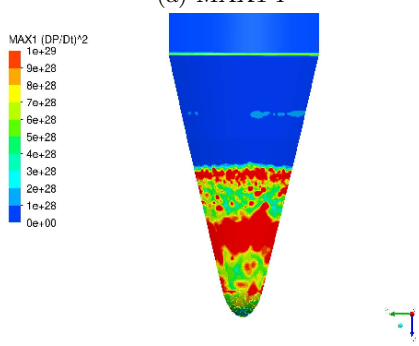

(c) MAX1 $(DP/Dt)^2$

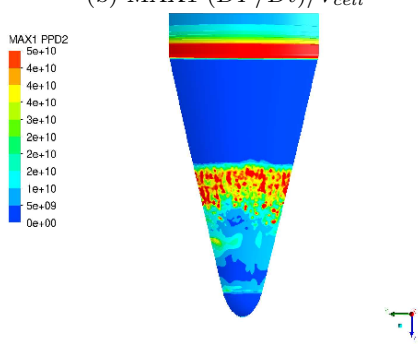

(d) MAX1 $PPD2$

Figure 4.16: Erosion assessment results - CAD Model, low lift, RANS

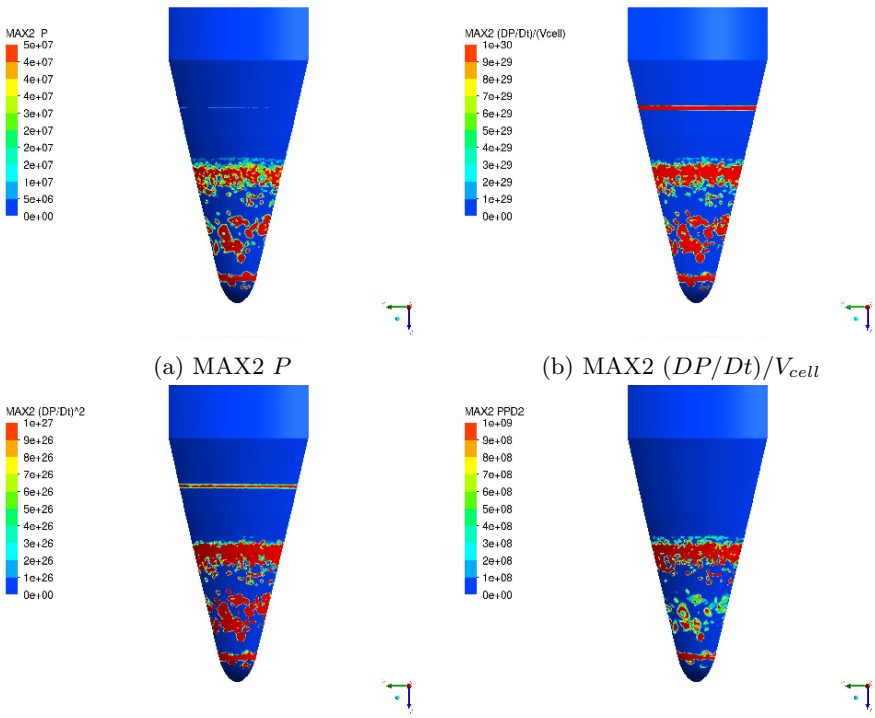

(a) MAX2 P

(b) MAX2 $(DP/Dt)/V_{cell}$

(c) MAX2 $(DP/Dt)^2$

(d) MAX2 $PPD2$

Figure 4.17: Erosion assessment results - CAD Model, low lift, RANS

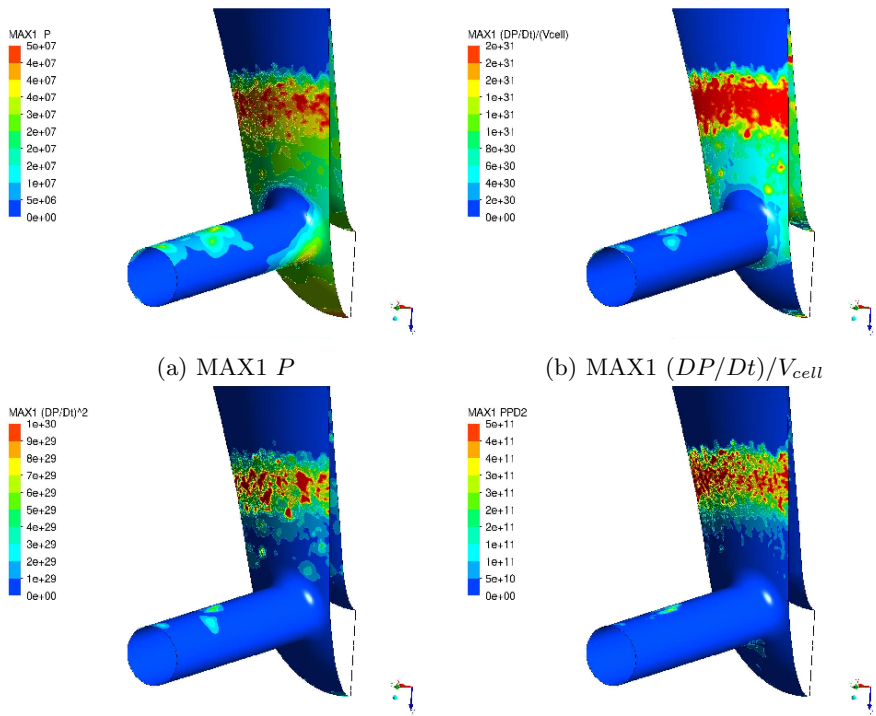

(a) MAX1 P

(b) MAX1 $(DP/Dt)/V_{cell}$

(c) MAX1 $(DP/Dt)^2$

(d) MAX1 $PPD2$

Figure 4.18: Erosion assessment results - CAD Model, low lift, RANS

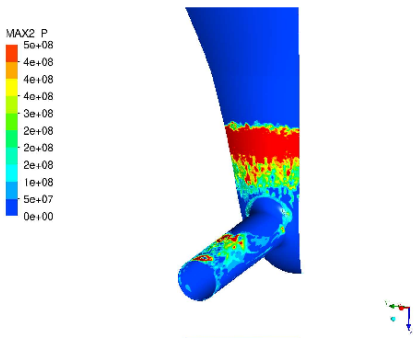

(a) MAX2 P

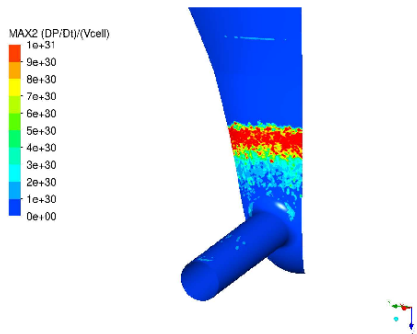

(b) MAX2 $(DP/Dt)/V_{cell}$

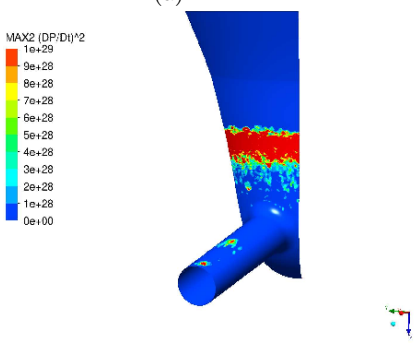

(c) MAX2 $(DP/Dt)^2$

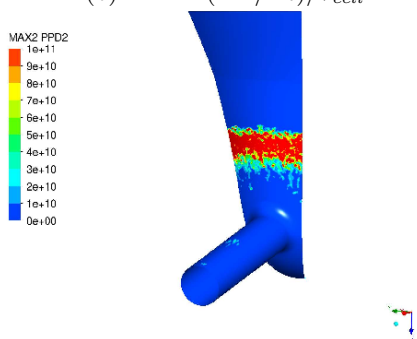

(d) MAX2 $PPD2$

Figure 4.19: Erosion assessment results - CAD Model, low lift, RANS

4.1.1.4 Low lift, LES, 1-hole

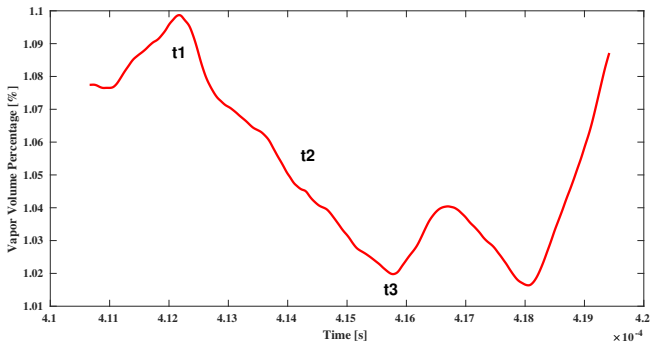

Figure 4.20: Vapor volume percentage change in time

Figure 4.20 presents the total vapor volume change in time for the low lift condition with the LES model. The average amount of vapor volume is much higher compared with the RANS results in previous section. Three time instants are presented in Figure 4.8 with snapshots of vapor formations and turbulent structures.

The shedding vapor structure between the needle and the needle seat in the RANS results seem to be separated from that region and convected to the downstream position and reach up to the orifice inlet. Thus, the size of the attached shedding vapor between the needle and needle seat is much smaller in this case. And of course, there are more dynamic vapor structures visible from t1 to t2 inside the orifice, due to larger range of flow scales resolved in LES.

Aforementioned high shear activity is only present at t1 time instant and gets dissipated in upcoming t2 and t3 time instants. There are two additional turbulent structures in all time instants: One stands near the bottom side of the inlet lip, the other one just stands close to the tip curvature of the needle.

As in the previous section, the erosion assessment is provided separately for both needle and sac surfaces, and both is presented with MAX1 and MAX2 algorithms.

Erosion assessments for the needle surface are presented in Figure 4.22 and 4.23. Similar erosion patterns are observed compared with the RANS results. Increased pitting activity near the needle tip is the only minor difference.

However for the sac surface, the LES and RANS damage locations are different. Figure 4.24 and 4.25 present erosion assessment for the sac and orifice surfaces. Here the damage is visible near the orifice entrance for both algorithms. As it is seen in the experiments, the initial damage (before the geometry changes completely) occurs near the orifice inlet.

It should be noted that the hole to hole interaction and surface deviation effects are not extensively investigated due to simulation cost, but the effect of those to the numerical results should be taken into consideration. The low lift erosion experiments (Figure 2.2) show that there are identical damage patterns just before the each hole's entry.

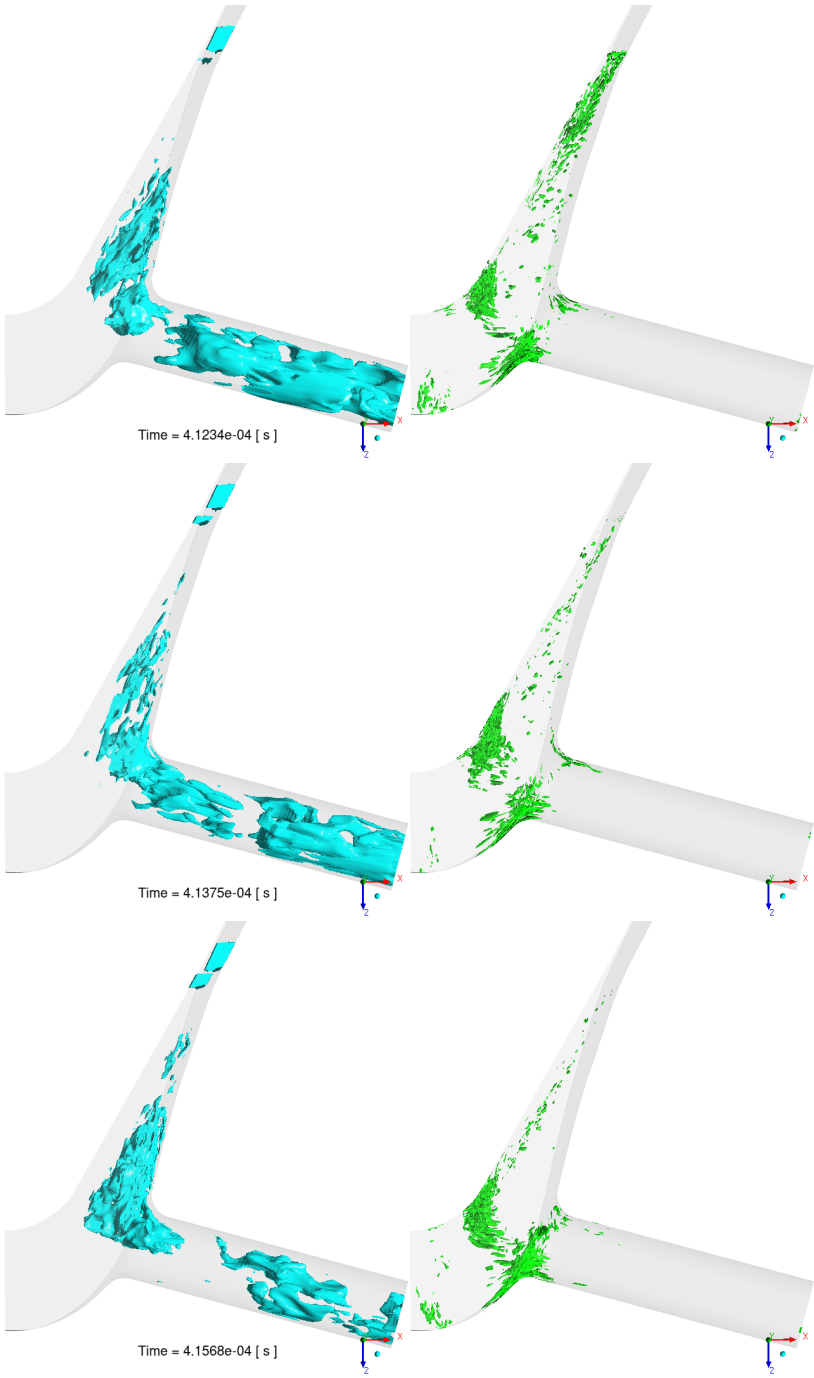

Figure 4.21: Vapor formations ($\alpha = 0.5$) and turbulent structures ($\lambda_2 = 5 \times 10^{13}$) t1, t2, t3 - CAD Model, Low lift, LES

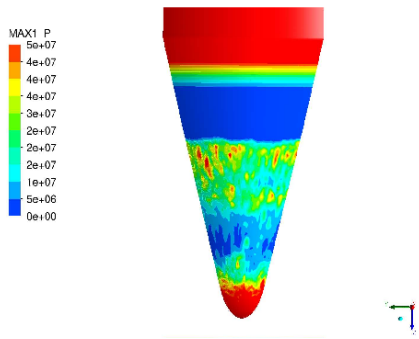

(a) MAX1 P

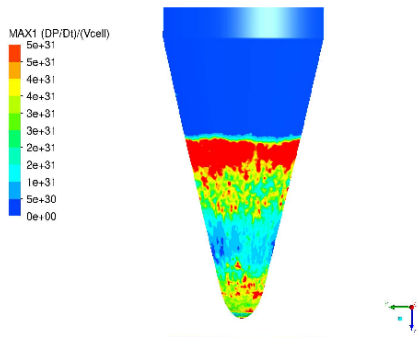

(b) MAX1 $(DP/Dt)/V_{cell}$

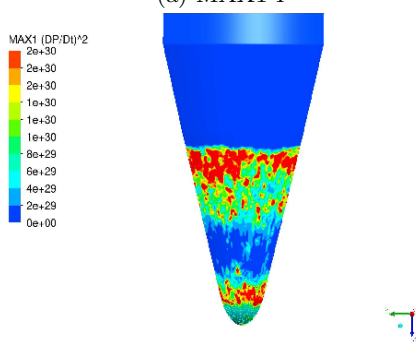

(c) MAX1 $(DP/Dt)^2$

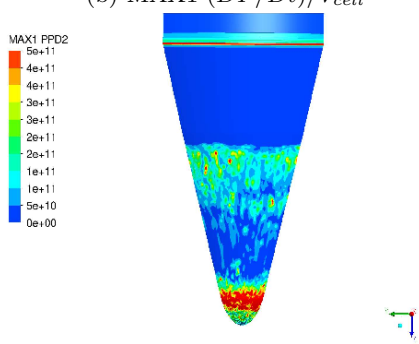

(d) MAX1 $PPD2$

Figure 4.22: Erosion assessment results - CAD Model, low lift, LES

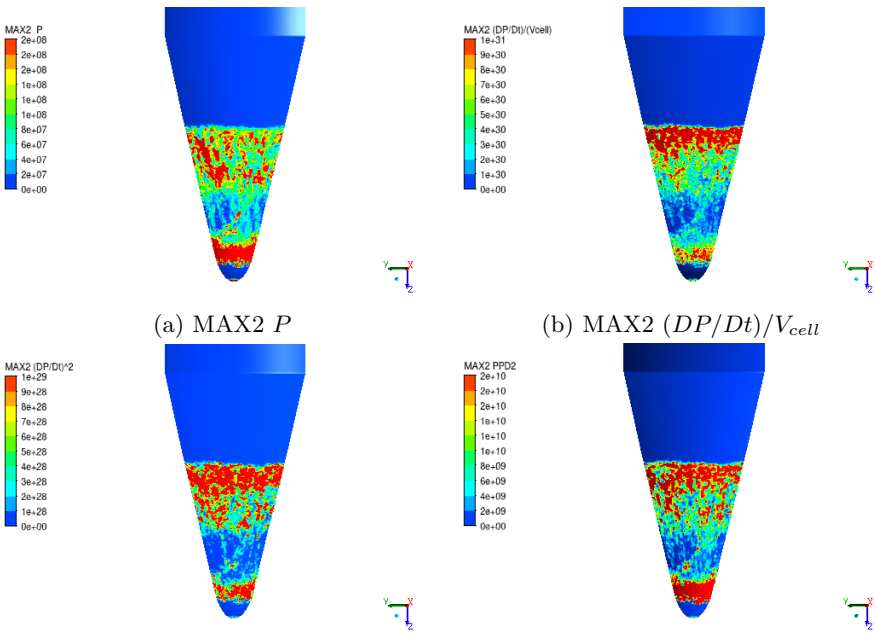

(a) MAX2 P

(b) MAX2 $(DP/Dt)/V_{cell}$

(c) MAX2 $(DP/Dt)^2$

(d) MAX2 $PPD2$

Figure 4.23: Erosion assessment results - CAD Model, low lift, LES

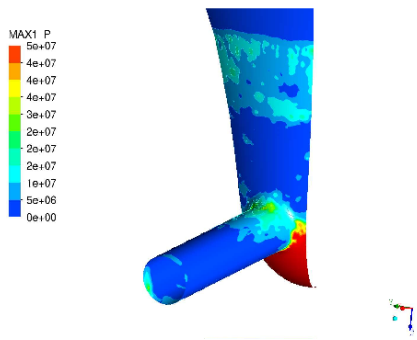

(a) MAX1 P

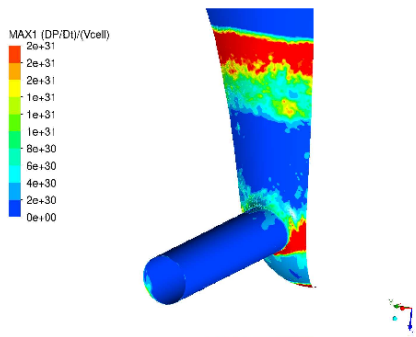

(b) MAX1 $(DP/Dt)/V_{cell}$

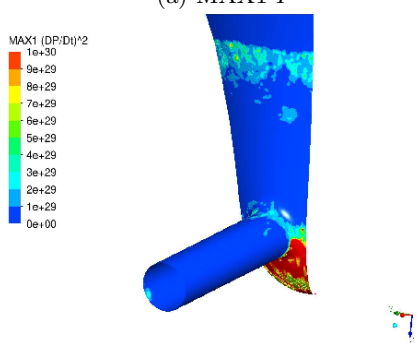

(c) MAX1 $(DP/Dt)^2$

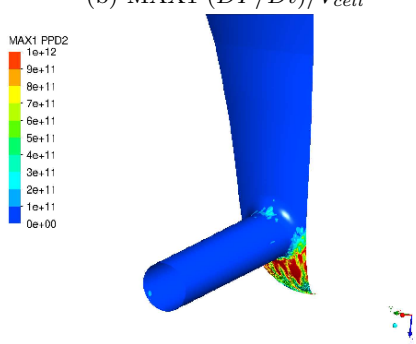

(d) MAX1 $PPD2$

Figure 4.24: Erosion assessment results - CAD Model, low lift, LES

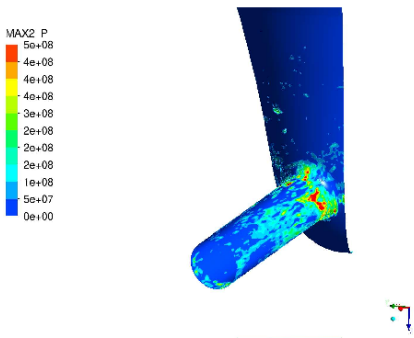

(a) MAX2 P

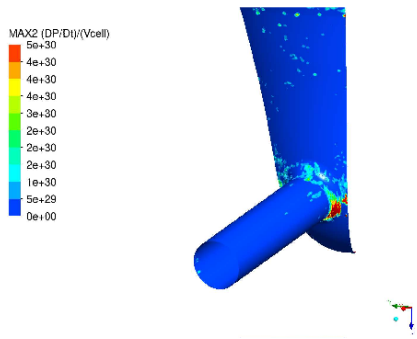

(b) MAX2 $(DP/Dt)/V_{cell}$

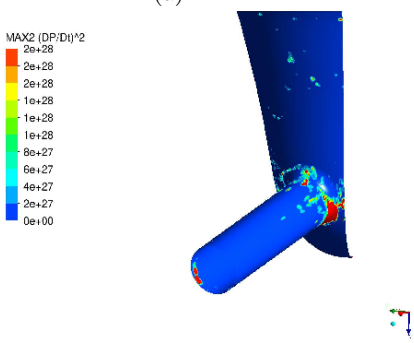

(c) MAX2 $(DP/Dt)^2$

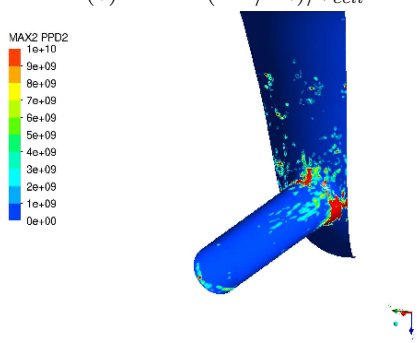

(d) MAX2 $PPD2$

Figure 4.25: Erosion assessment results - CAD Model, low lift, LES

4.1.2 TS Model

In this section, we present the results of the TS Model in high lift position (1-hole) and highlight the primary distinctions from the CAD Model (section 4.1.1). Then, TS Model 8-hole RANS results will be presented.

4.1.2.1 High lift, RANS, 1-hole

The vapor volume percentage change in time, plotted in Figure 4.26 with a short duration to show the intermittent changes in simulation. The average vapor volume percentage is 0.0735 %, while in CAD Model this value was around 0.175 %. Hence, there is a reduction in total vapor volume once the surface deviation features are taken into account with TS Model. A further insight is provided by Figure 4.27, where the presence of additional vapor structures due to surface deviations is evident. A direct comparison with the RANS CAD Model indicates a reduced volume of the attached sheet cavity at the top side of the injector in the TS Model. This reduction is apparent on the left side of Figure 4.27, where the sheet cavity begins at the orifice inlet and extends to the outlet but is narrower throughout the flow path. The turbulent structures on the right side of Figure 4.27 shows that small turbulent structures (near orifice sides) can be directly created by the surface deviations. Compared with the RANS CAD Model results, there is higher turbulent activity on the top side of the orifice, with turbulent structures extending up to the orifice exit.

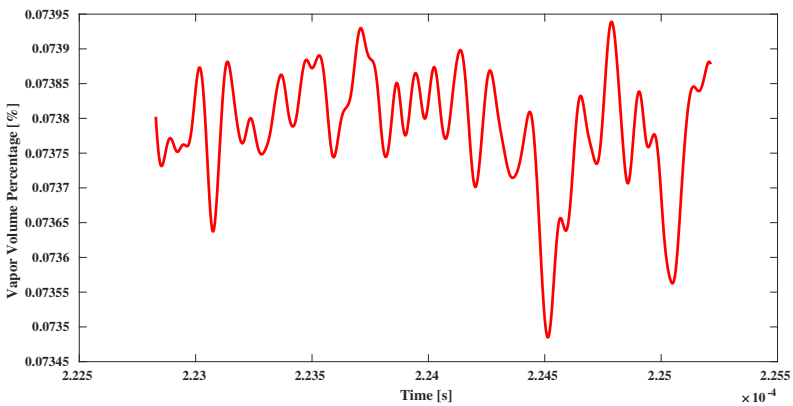

Figure 4.26: Vapor volume percentage change in time

In Figure 4.28, it is evident from the cut plane that surface deviations creates additional vapor structures on the top side of the orifice wall as well. Here, Figure 4.29 is a good example to show that this vapor generation mechanism is valid across the whole orifice wall surfaces, unlike the RANS CAD Model results (see Figure 4.3).

The force comparison plot, provided in Figure 4.30, for the "top" and "bottom" orifice surfaces shows the respective forces acting on these regions over

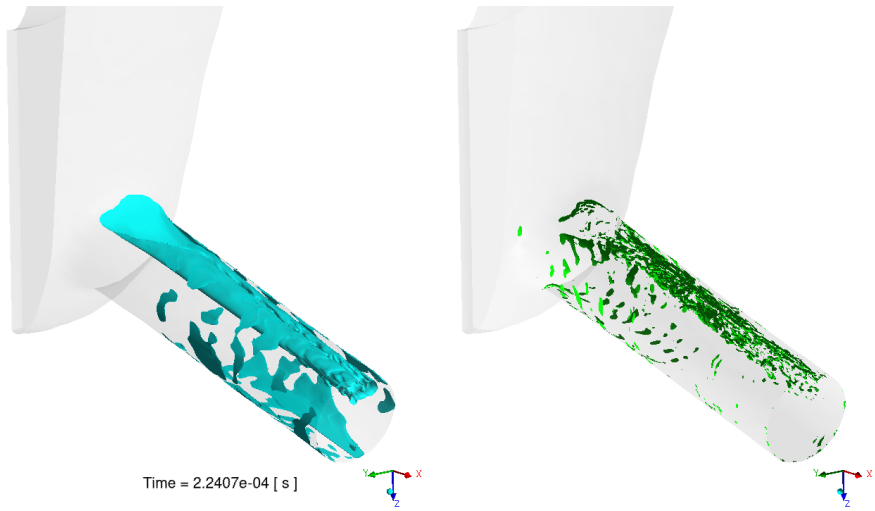

Figure 4.27: Vapor formations ($\alpha = 0.5$) and turbulent structures ($\lambda_2 = 5 \times 10^{13}$) - TS Model, high lift, RANS

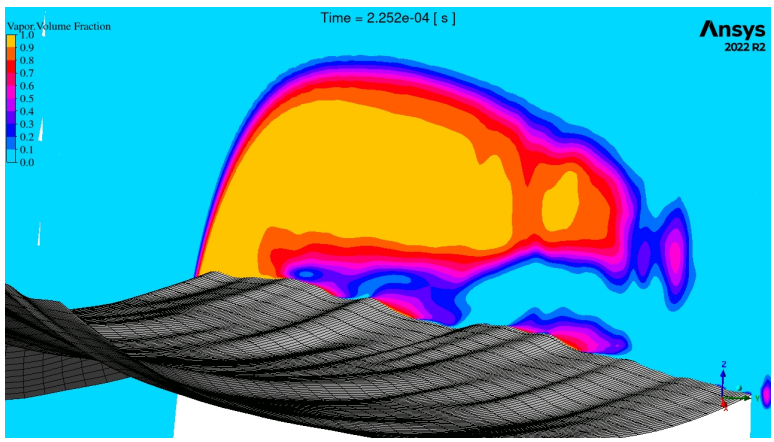

Figure 4.28: Surface mesh representation with cut plane volume fraction

time. The spikes in force could be indicative of cavitation bubble collapse events that exert impulse loads on the injector surfaces, leading to potential erosion. The variation between top and bottom forces also suggests an asymmetric distribution of cavitation within the orifice. Moreover, the consistent amplitude of force on the bottom surface could be interpreted as a sign of less aggressive or less frequent cavitation occurrences, or possibly a more stable cavitation that does not result in strong impulsive loads. The presence of higher force magnitudes on the top surface indicates that this region is more prone to cavitation erosion and subjected to more severe cavitation events, due to impulsive behavior of the attached sheet cavity in that area.

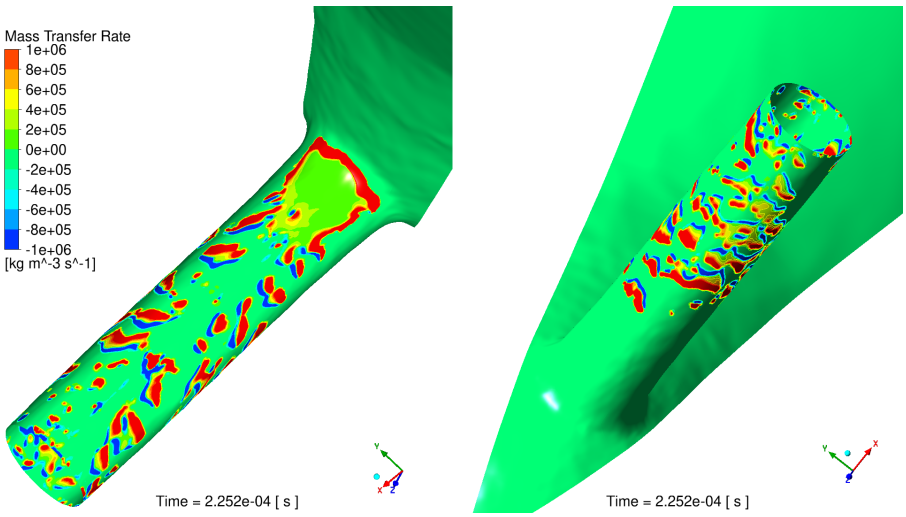

Figure 4.29: Mass Transfer Rate contour plot on the walls

The visualizations provided in Figures 4.31 and 4.32 present the potential erosion areas within the injector orifice for the TS Model using the MAX1 and MAX2 algorithms. These results can easily be compared with the RANS CAD Model results to understand the effect of the surface deviations to the erosion assessment results.

For MAX1, a stagnation effect is still present and affecting almost all erosion indicators, but the in this case high values are more persistent for material derivative indicators ($(DP/Dt)/V_{cell}$, $(DP/Dt)^2$). Hence, the erosion pattern is located on the top side of the orifice, similarly as in CAD Model result, but the extent of the erosion pattern is much longer than the RANS CAD Model results. For MAX2, there is a good agreement with experiment for almost all erosion indicators. Hence it can be concluded that in overall agreement with experiment is much better with the presence of surface deviations with RANS.

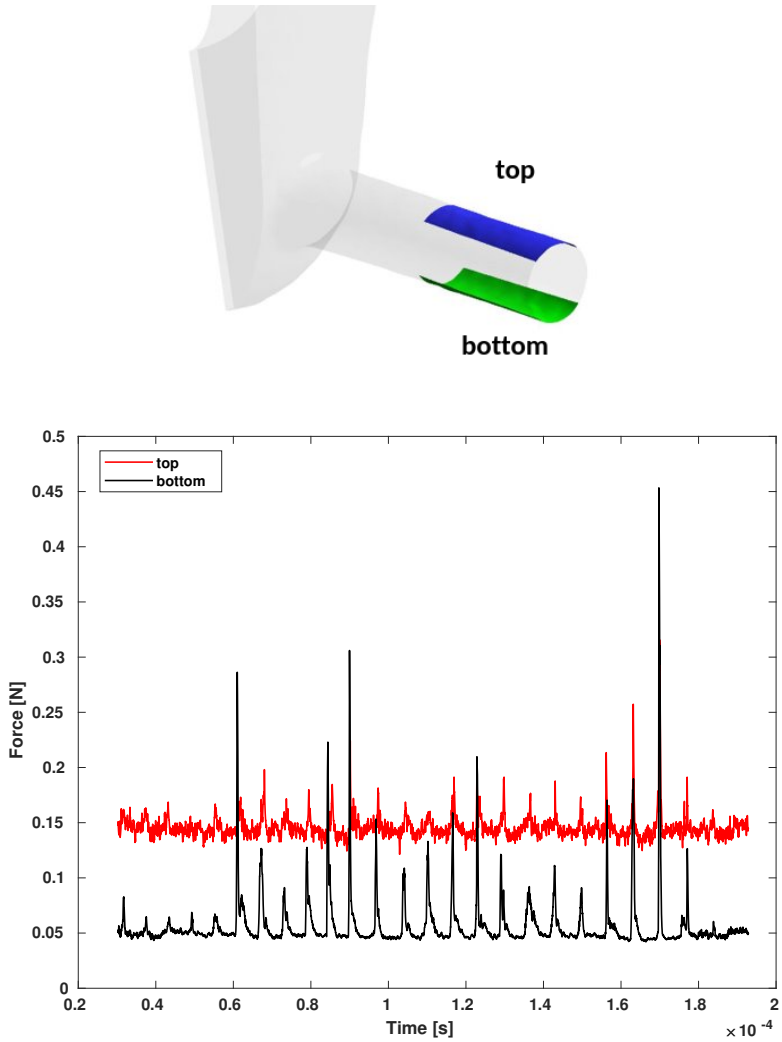

Figure 4.30: Force plot comparison history of the selected "top" and "bottom" orifice surfaces

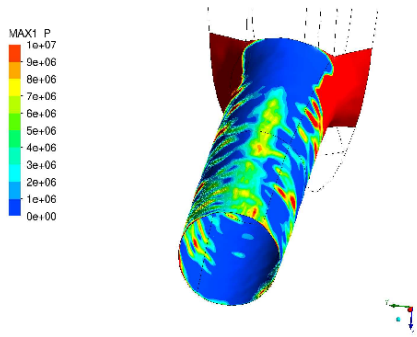

(a) MAX1 P

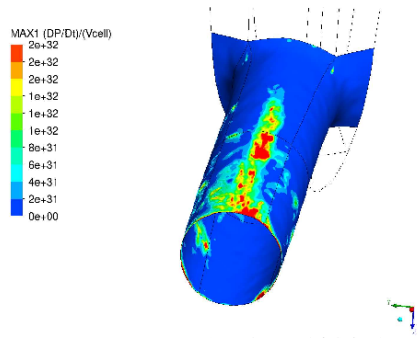

(b) MAX1 $(DP/Dt)/V_{cell}$

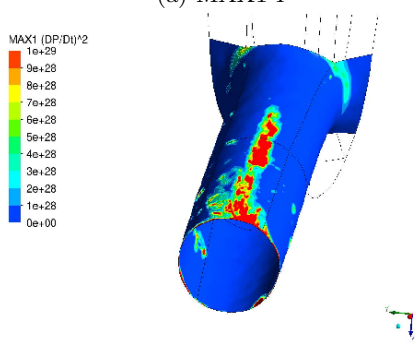

(c) MAX1 $(DP/Dt)^2$

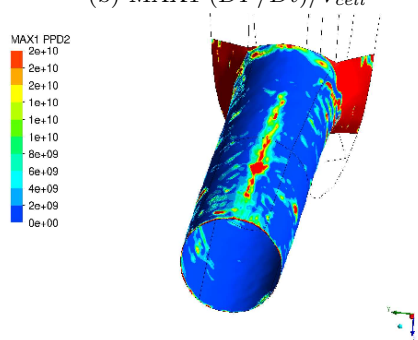

(d) MAX1 $PPD2$

Figure 4.31: Erosion assessment results - TS Model, high lift, RANS

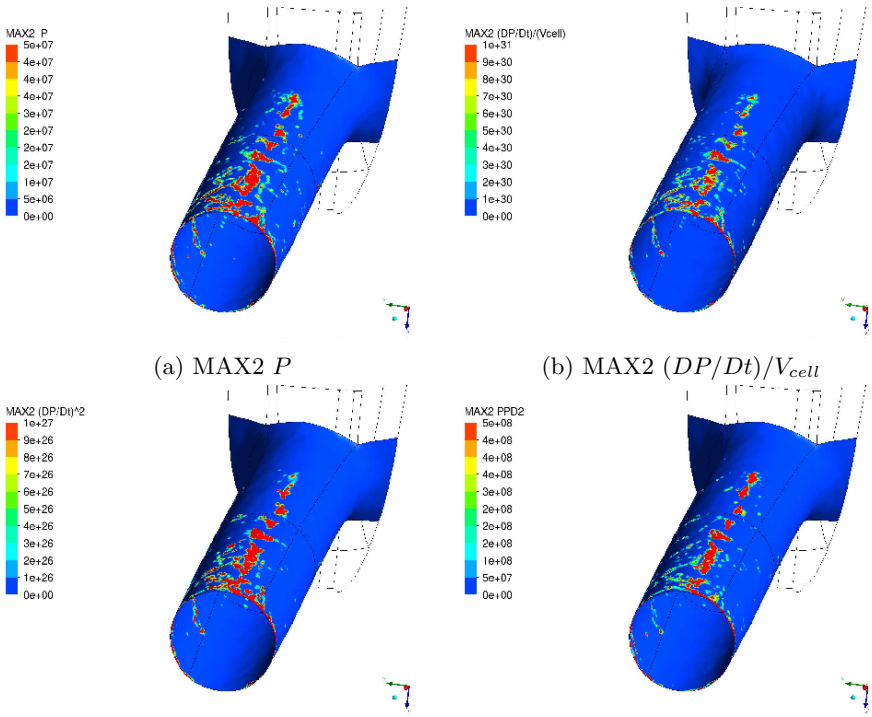

(a) MAX2 P

(b) MAX2 $(DP/Dt)/V_{cell}$

(c) MAX2 $(DP/Dt)^2$

(d) MAX2 $PPD2$

Figure 4.32: Erosion assessment results - TS Model, high lift, RANS

4.1.2.2 High lift, LES, 1-hole

Figure 4.33 illustrates the change in vapor volume percentage in time. The average vapor volume percentage here is 0.075 %, while in the LES - CAD Model results this value was around 0.2 % . The global minimum (t1) and maximum (t5) values are also less than the LES CAD Model results. It has been shown in previous section that this is due to the surface deviations.

Six selected (and labelled in Figure 4.33) snapshots for the vapor and turbulent structures are presented in Figure 4.34 and 4.35 with their corresponding time instants. Similarly as in previous results, the left side of these figures show the vapor formations and turbulent structures are provided in the right side. This is evident from the images of vapor structures at the t1 instant, where the attached sheet cavity does not reach the orifice exit. At t1, the stream-wise length of the split two core vapor is shorter compared to what is observed in the subsequent time instants t2 to t5. From t5 to t6 the vapor volume get condensates back to the liquid, hence collapses. Apart from the attached sheet cavity on the top side, vortex cavitation structure on the bottom half changes its shape through time t1-t6.

For all time instants, the turbulent activity is high and turbulence generation due to the surface deviations are more visible compared with RANS TS Model results. The turbulent structures near the bottom side of the orifice entrance persist and undergo changes in their overall shape over time. The size and number of the iso-surfaces increased from t1 to t2, then get back to its same size in t3. On the top side of the orifice high shear activity due the attached sheet cavity is apparent.

The time instant t6 is further examined in Figure 4.36 with vortical structures and cut plane streamline to provide an insight about cavitation and turbulence relationship. Here on the left side, the presence of strong vortices enhance the cavitation process in especially bottom half by lowering the pressure in that region. Additionally, it's worth noting the vortices created by surface deviation near the exit of the orifice. On the right side, the flow is accelerating in pure liquid region since the vapor structures are narrowing down the orifice hole passage transporting in lower velocity. Hence, the difference in velocity creates shear layer regions inside the orifice.

Figure 4.38 presents a sequence of snapshots depicting the collapse of vapor formations alongside corresponding pressure distributions on the top and bottom sides of the injector orifice over time. The selected time interval here is from t5 to t6. As the time progress, on the top side of the orifice, attached sheet cavity shrinks and collapse near the orifice outlet and create wall pressure with a magnitude of at least 200 bar. The bottom side vapor formation (vortex cavitation) on the other hand, does not create such an high wall pressure values although it changes its shape.

The similar mechanism can be examined in Figure 4.37, which provides the force history of selected "top" and "bottom" orifice surfaces. The sharp peaks, particularly on the top surface (red line), suggest moments when cavitation bubbles collapse near the wall, causing high-pressure impacts. These impacts can be strong enough to damage the material over time. The relative height

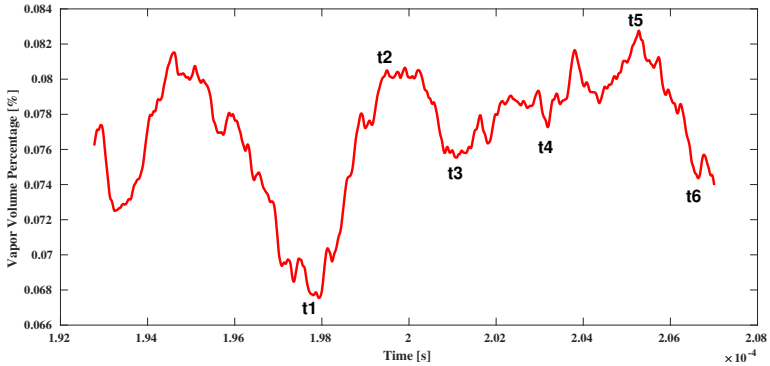

Figure 4.33: Vapor volume percentage change in time

and frequency of the peaks could indicate the severity and rate of cavitation events. Higher and more frequent peaks on the top surface suggest more intense cavitation erosion activity compared to the bottom.

In the MAX1 algorithm, all erosion indicators show higher values on the top side of the orifice than on the bottom side. Excluding the aforementioned stagnation effect, there is a good agreement with high lift experiments. This also agrees well with previous conclusions from a force history comparison (Figure 4.37) and the collapse mechanism illustrations (Figure 4.38).

In contrast, the MAX2 algorithm displays damage on the bottom side, as seen in the LES CAD Model results, and it is more dispersed across the entire orifice surface. The extent of the damage, indicated by the red-colored areas, is slightly greater on the top surface but not to the extent shown by the MAX1 algorithm. A direct comparison of the $(DP/Dt)^2$ erosion indicator between both algorithms highlights these differences.

In Figure 4.41, orifice wall surfaces for the erosion assessment are offset (towards internal domain) with a distance of 10 µm. In this way, the effect of the surface deviations is considered to be limited. Here, the top side damage is dramatically higher than the bottom side. Comparing these results with those where no offset was applied (as shown in Figure 4.39 (a)) reveals a substantial difference in the patterns and extent of erosion damage.

Therefore, these findings suggest that the LES simulation of TS Model using MAX2 algorithm is highly sensitive to surface deviations, since mass transfer rate directly is enriched by LES. Hence, the enriched mass transfer rate condition (Condition3 in MAX2 algorithm in Table 3.18) makes MAX2 algorithm vulnerable to those surface deviations and manipulate the overall erosion pattern.

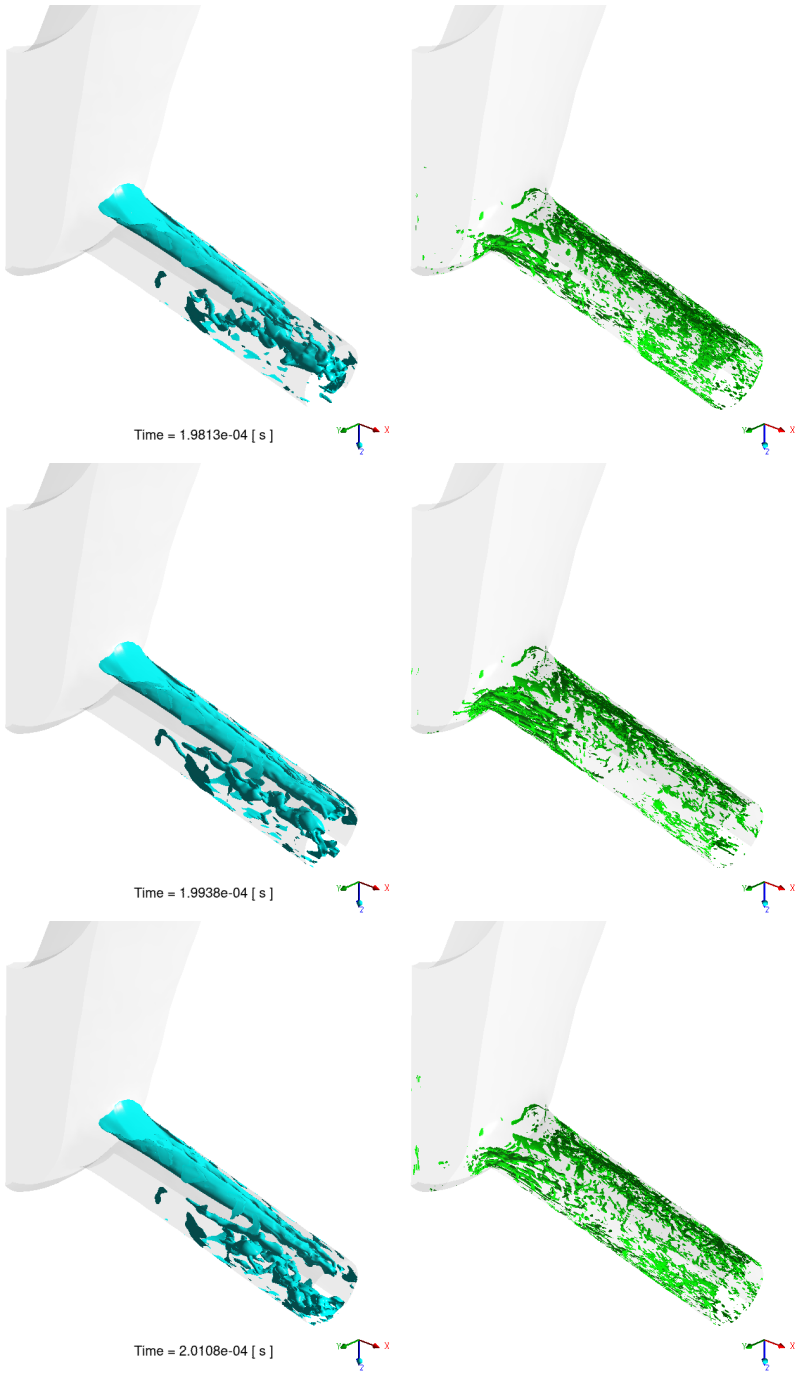

Figure 4.34: Vapor formations ($\alpha = 0.5$) and turbulent structures ($\lambda_2 = 5 \times 10^{13}$) t1, t2, t3 - TS Model, high lift, LES

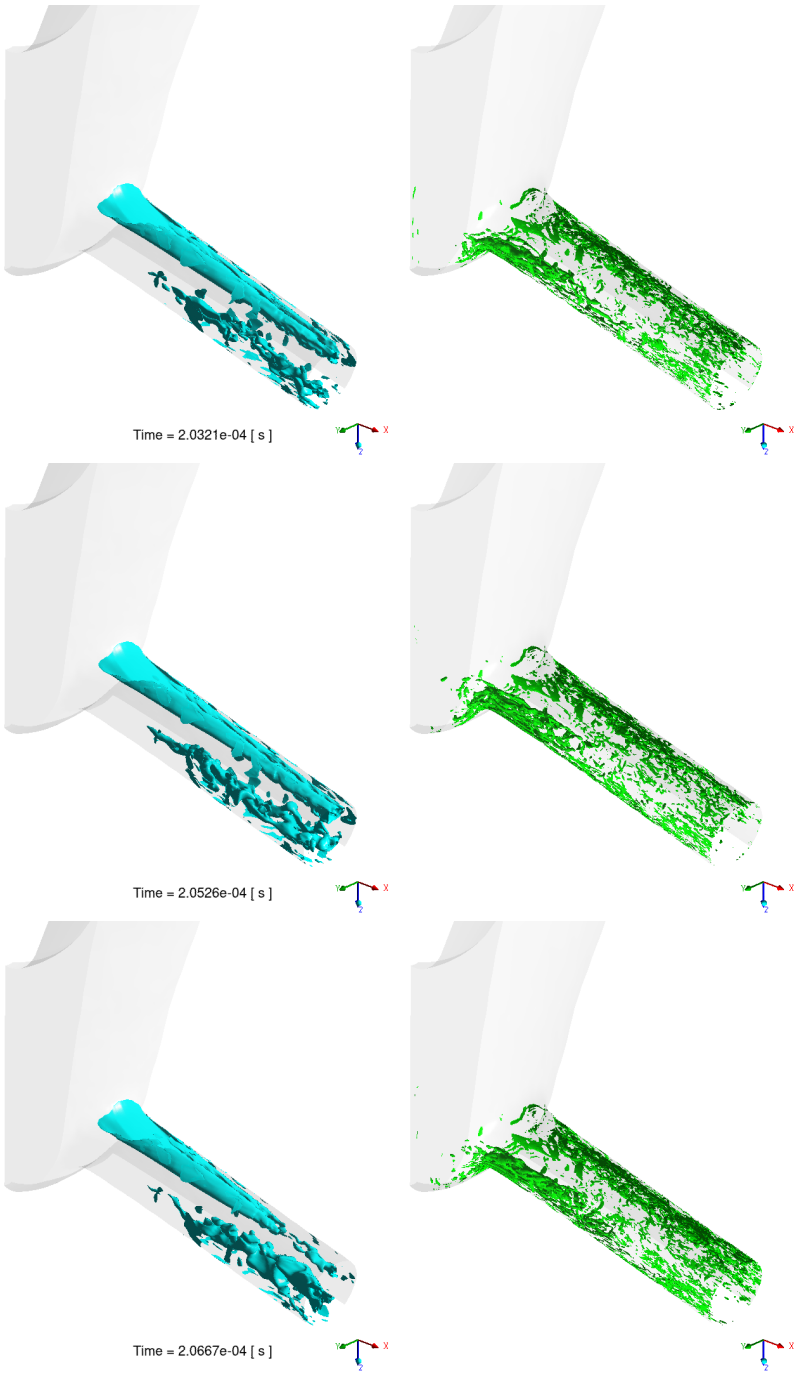

Figure 4.35: Vapor formations ($\alpha = 0.5$) and turbulent structures ($\lambda_2 = 5 \times 10^{13}$) t4, t5, t6 - TS Model, high lift, LES

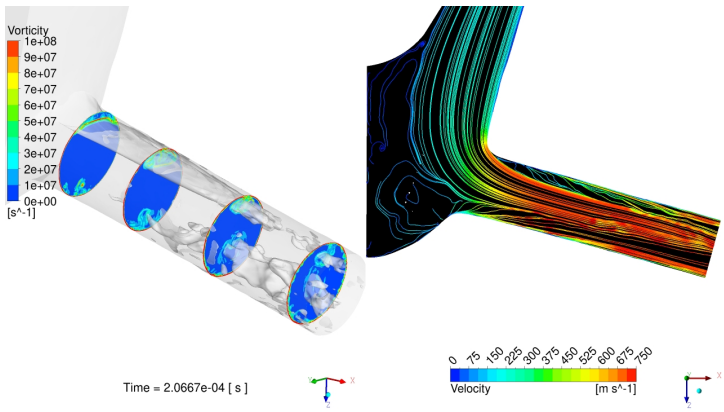

Figure 4.36: Vorticity fields on cross section cut planes together with transparent vapor structures (left) and velocity colored streamlines on injector mid-plane (right)

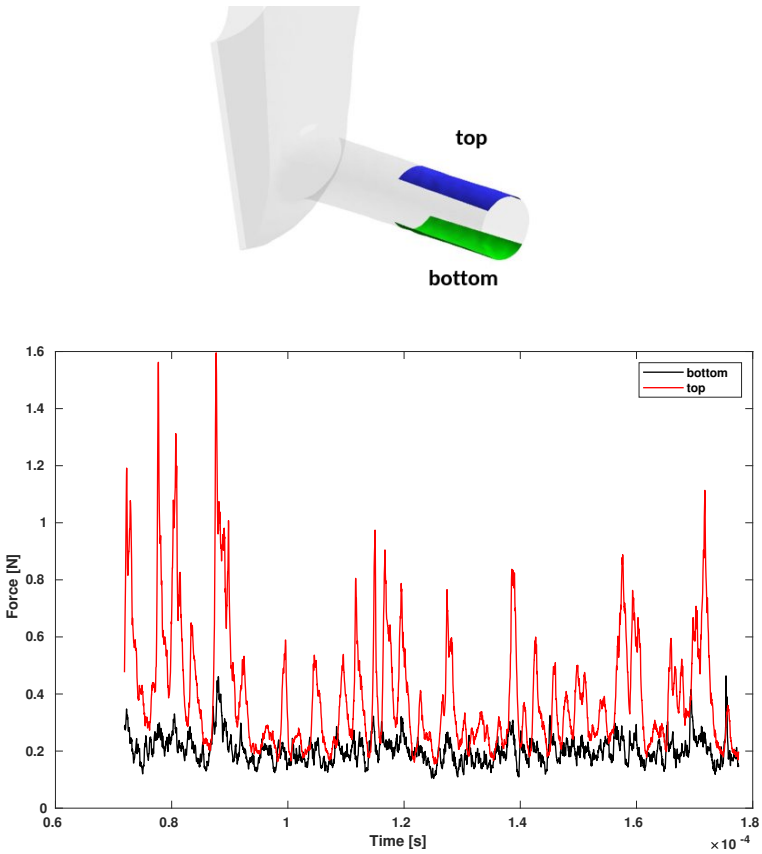

Figure 4.37: Force plot comparison history of the selected "top" and "bottom" orifice surfaces

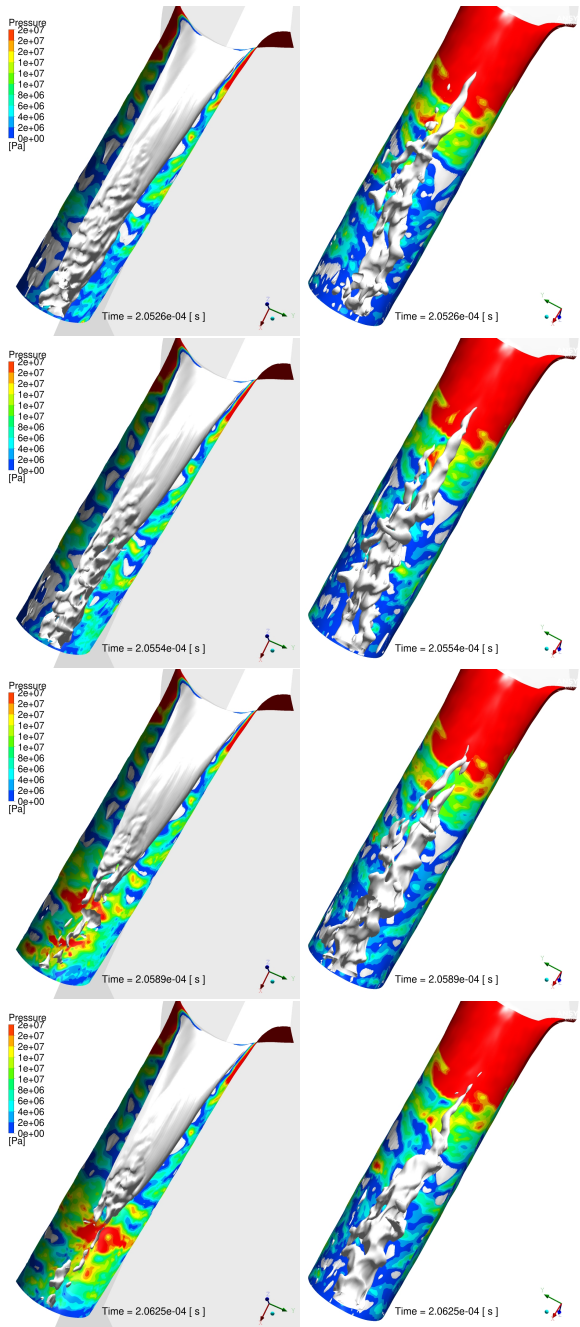

Figure 4.38: Collapse mechanism representation with vapor formations and wall pressure snapshots on the top (left) and bottom (right) side of the orifice

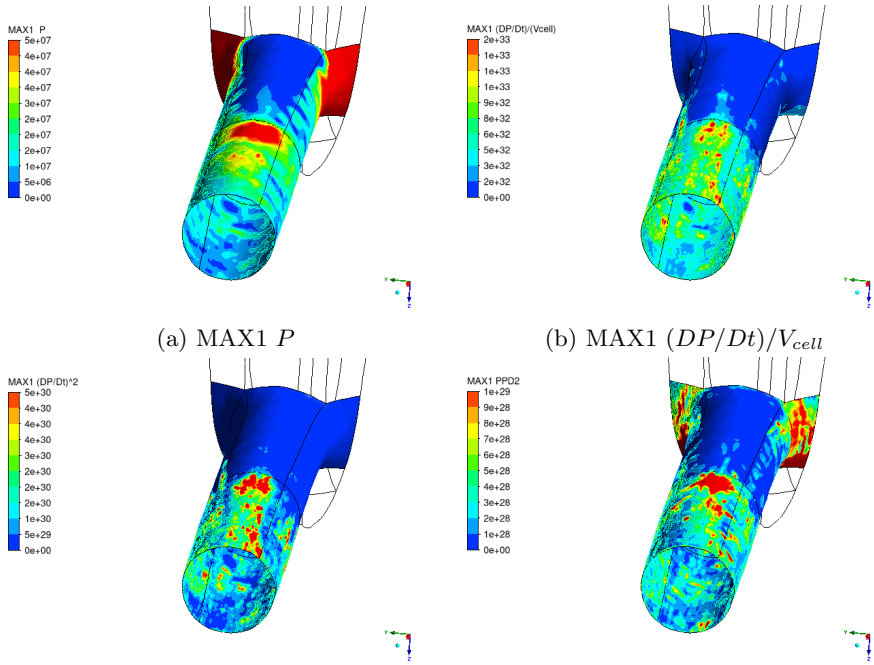

(a) MAX1 P

(b) MAX1 $(DP/Dt)/V_{cell}$

(c) MAX1 $(DP/Dt)^2$

(d) MAX1 $PPD2$

Figure 4.39: Erosion assessment results - TS Model, high lift, LES

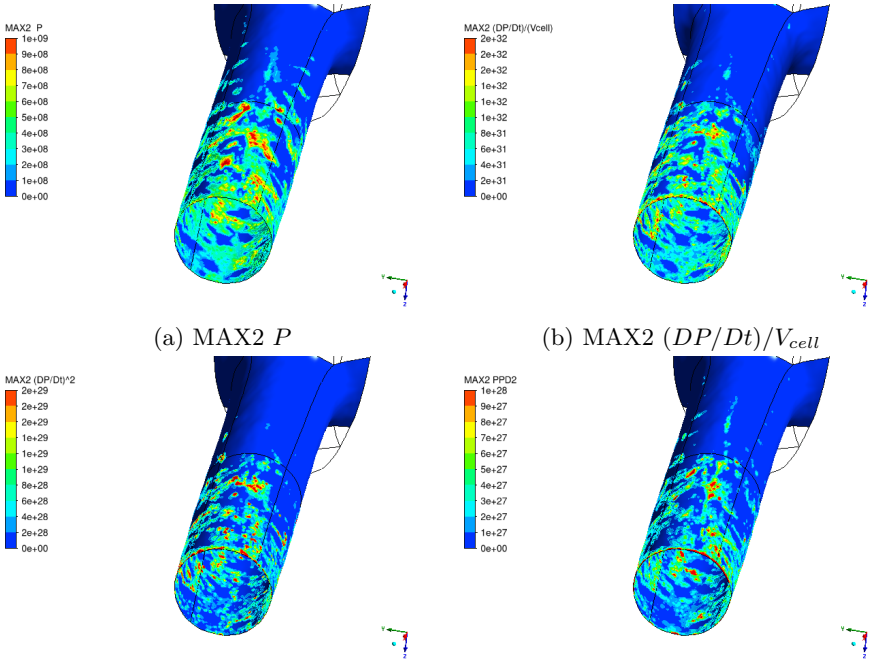

(a) MAX2 P

(b) MAX2 $(DP/Dt)/V_{cell}$

(c) MAX2 $(DP/Dt)^2$

(d) MAX2 $PPD2$

Figure 4.40: Erosion assessment results - TS Model, high lift, LES

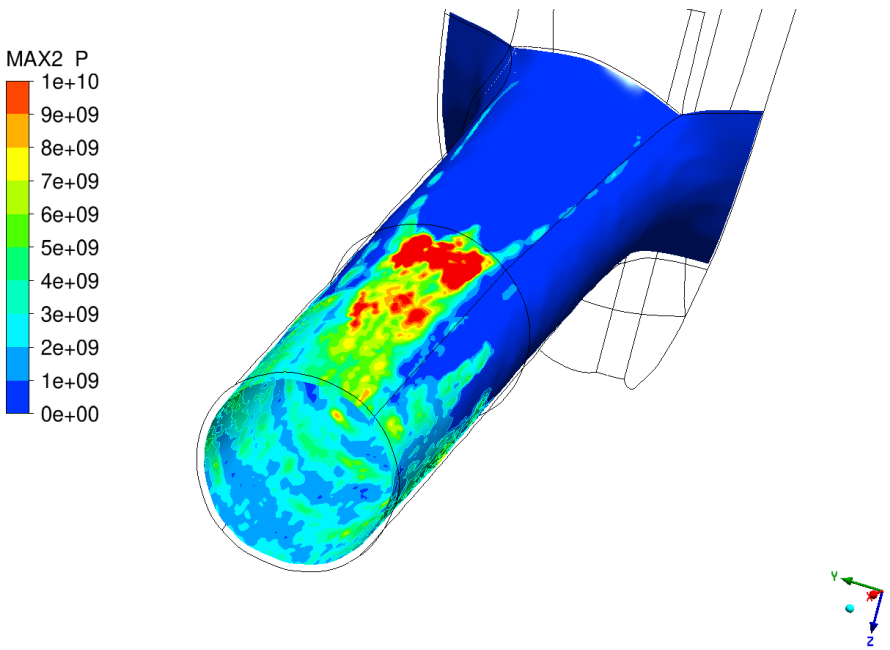

Figure 4.41: Erosion assessment of 10 μm offset surface - MAX2 P

4.1.2.3 High lift, RANS, 8-hole

In Figure 4.42, vapor formations and turbulent structures snapshots are presented. On the top of the Figure 4.42, the overall shape of cavitation structures is similar, but characteristics of attached sheet cavity on the top side of the each hole may vary for some particular holes in downstream positions. Additionally, some holes have bottom half vapor formations, which are not captured in the RANS TS Model 1-hole simulations, only with LES turbulence modeling.

On the bottom side of the Figure 4.42, it is possible to see hole to hole interactions between the holes. Again, these are not seen in TS Model 1-hole simulations, even with LES TS Model results. This might be due to the limitation of the periodic boundary conditions [17].

For any particular hole, the number of cells and level of resolution is different between TS Model 1-hole and 8-hole simulations. To achieve the same level of mesh resolution in the 1-hole for the 8-hole simulation, a high cost is estimated that around 55 million cells are needed. Nevertheless, these results further points out the importance of hole to hole interactions and effect of each hole's identical surface deviations

Figure 4.43 and Figure 4.44 present the erosion assessment results in both MAX1 and MAX2 algorithms respectively. Here, the results are presented only with $(DP/Dt)^2$ erosion indicator, which was the most reliable for both algorithms in the 1-hole RANS - TS Model (section 4.1.2.1) erosion assessment

Overall, the results are in good agreement with experiments. Maximum values take place on the top side of each hole. Similarly as in previous results, MAX2 prevents fake collapses, and this eliminates the bottom side erosion patterns that weakly exist in MAX1 algorithm. Numerical results further support that having identical surface deviations for each hole creates distinct erosion patterns. This makes the overall erosion assessment much more complicated.

As previously mentioned in methodology section that hole7 had been selected for TS Model 1-hole simulations among the other injector holes. In both of the Figures 4.43 and 4.44, this hole is specially marked. A direct comparison between these results and RANS TS Model 1-hole results states that asymmetric top side erosion pattern is consistently apparent despite different mesh resolutions.

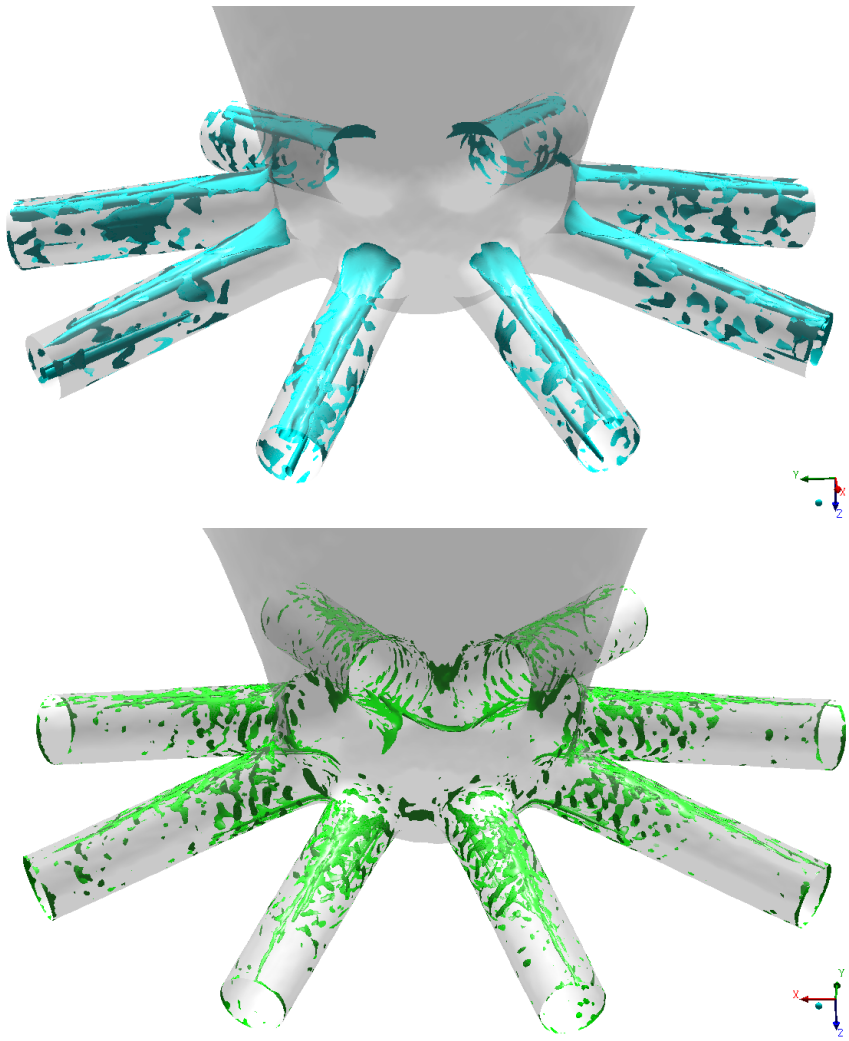

Figure 4.42: Vapor formations ($\alpha = 0.5$) and turbulent structures ($\lambda_2 = 5 \times 10^{13}$) - TS Model 8-hole, high lift, RANS

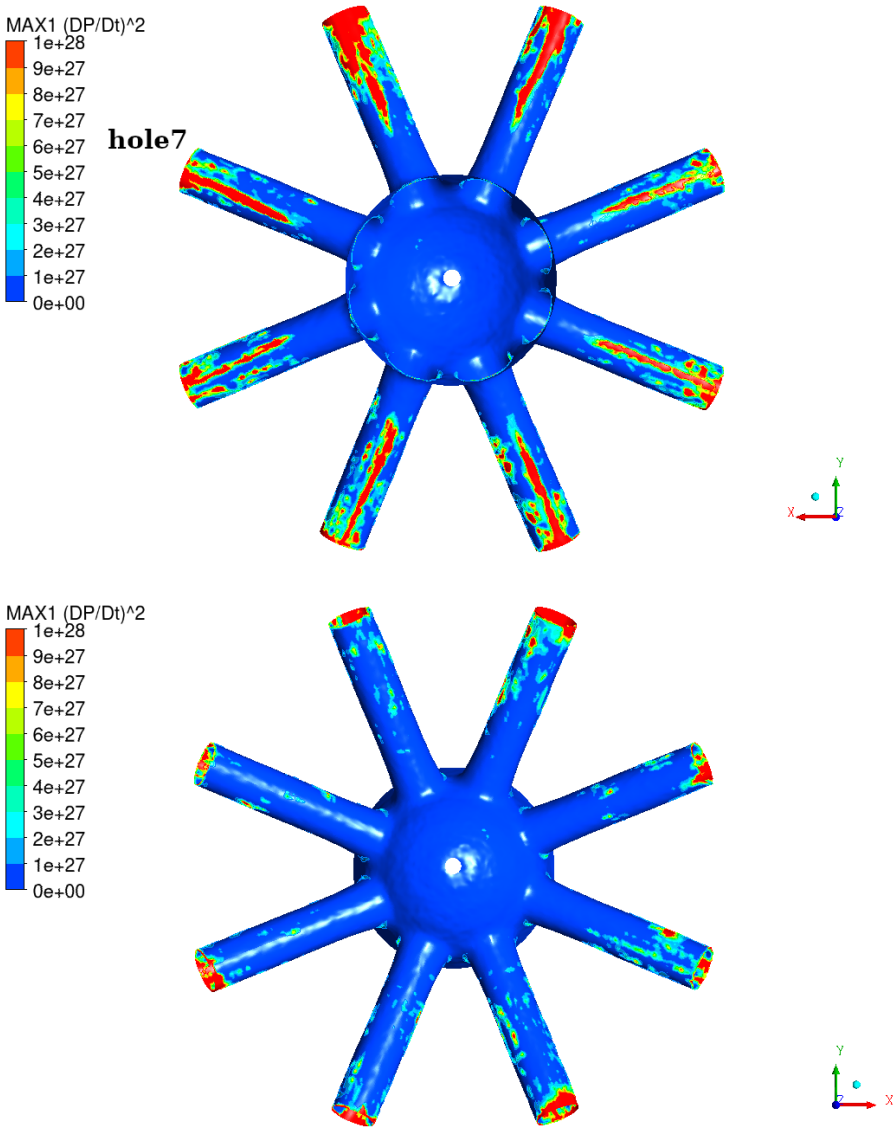

Figure 4.43: Erosion assessment with MAX1 $(DP/Dt)^2$, top and bottom view to the 8-hole injector

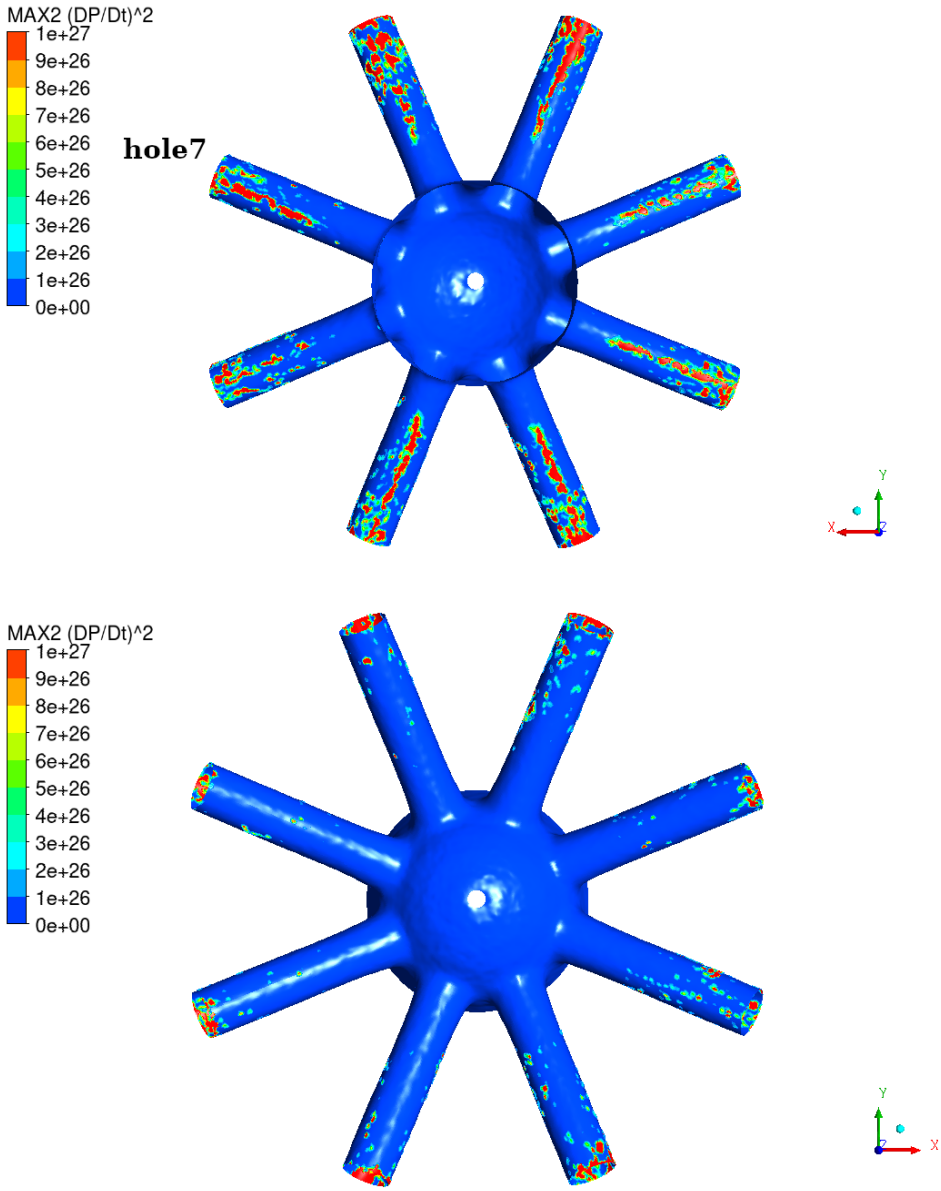

Figure 4.44: Erosion assessment with MAX2 $(DP/Dt)^2$, top and bottom view to the 8-hole injector

4.1.3 Predictive capability of the numerical method and erosion model

In previous sub-sections, various computational approaches and erosion indicators are investigated for complete erosion assessment. The analysis covered scenarios with both RANS and LES models, considering different lift conditions and surface models. This subsection offers recommendations based on the performance of the computational approach and erosion model.

The stagnation effects and prevention of the fake collapses made MAX2 algorithm more reliable than MAX1. Here, the MAX2 algorithm is providing more accurate and localized erosion patterns in all cases. The MAX2 algorithm shows good agreement with experimental data across various simulation scenarios. Material derivative erosion indicators, and $(DP/Dt)^2$ erosion indicator in particular, demonstrate more reliable performance and captures erosion patterns. Hence, for accurate and reliable erosion assessment in cavitation simulations, it is recommended to employ the MAX2 algorithm along with the $(DP/Dt)^2$ erosion indicator. This combination is likely to provide a more accurate representation of cavitation erosion patterns and improve the overall agreement with experimental data.

In both static lift positions, LES captured more dynamic flow structures than RANS, as expected, providing a more dynamic representation of cavitation structures compared to RANS simulations. The ability of LES to capture larger and more dynamic range of eddies and flow structures is evident in the results, showcasing its superiority in resolving complex flow phenomena.

It's vital to recognize that LES is significantly more computationally expensive than RANS due to its need for a finer spatial grid, smaller time steps, and longer simulation times. The computational cost of LES is roughly 32 times higher than that of RANS. Therefore, the choice between LES and RANS should be carefully made, taking into account the available computational resources and the specific needs of the study.

In the presence of surface deviations (TS Model) in the high lift condition, RANS showed reliable performance. Surface deviations in the TS Model influenced vapor structures, providing a more realistic representation. This sensitivity to surface deviations was particularly noticeable when using the MAX2 algorithm, where RANS demonstrated reliable performance compared to LES. Hence, this makes RANS still a powerful tool especially for this type of industrial cases.

4.2 Dynamic Needle Results

4.2.1 Flow Statistics

Mean mass flow rates of each hole for “lift only” and “wobbling” simulations are presented in Table 6. Based on the listed data, it is possible to say that mean mass flow rates for lift only motion and wobbling motion vary for different hole numbers. Individual surface deviation characteristics, which are distinct for each hole, could be influencing the variations in mean mass flow rates.

Table 4.1: Mean mass flow rates of each hole for ”lift only” and ”wobbling” motion

Hole number	**Mean mass flow rate (g/s) lift only motion**	**Mean mass flow rate (g/s) Wobbling motion**
1	21.9	21.2
2	22.2	22.4
3	21.8	22.6
4	21.5	21.2
5	21.4	21.4
6	24.1	23.4
7	21.0	21.4
8	21.4	21.6
Average	21.9	21.9

In addition to the mean mass flow rates, Figure 4.45 displays the mass flow history of each hole. The results are presented in a manner that allows for a direct comparison of the instantaneous mass flow rates between lift only motion and wobbling motion.

As previously mentioned, the needle moves towards the area between hole 2 and hole 3 during the off-axis (wobbling) motion, as shown in Figure 3.14. It is evident from Figure 4.45 that the mass flow rate values of hole 2 and hole 3 are significantly influenced by the wobbling motion, exhibiting higher gradients compared to the mass flow rate plots in the lift only motion.

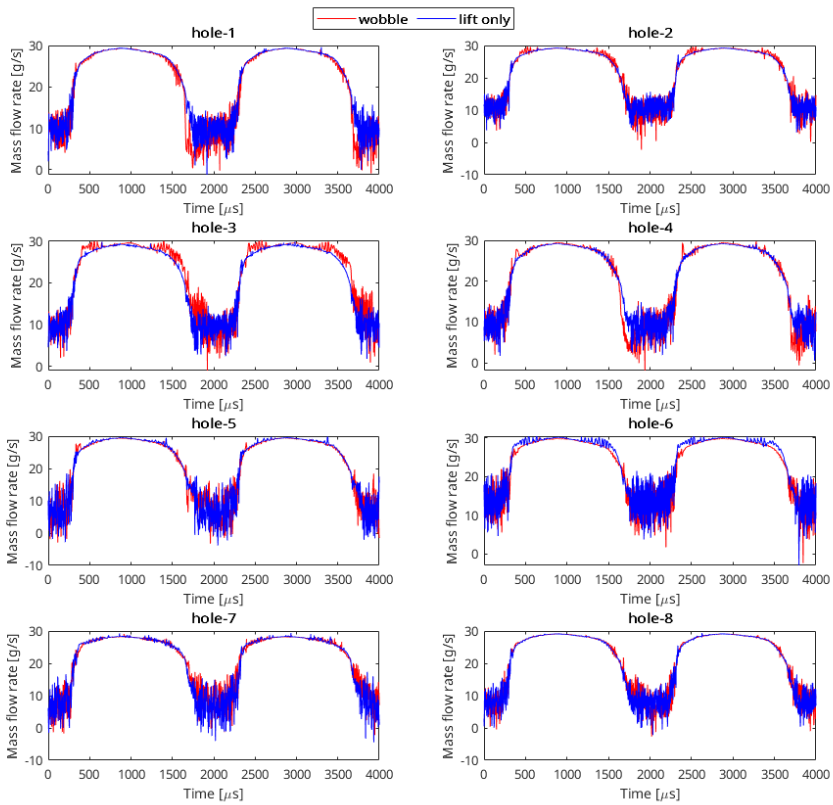

Figure 4.45: Mass flow rate comparison for each hole during simulation time

To further discuss the effect of the off-axis motion, normalized total vapor volume change during the two cycles is plotted in Figure 4.46 for both simulations. During the two cycles of mesh motion, the needle remains at its lowest lift condition at the beginning, middle, and end times (0, 2000, and 4000 μs). Comparing it to the lift-only motion simulation, we observe higher total vapor volume gradients in the wobbling motion simulation. This is because the needle remains close to the sac during the corresponding low lift time instants, and off-axis displacement becomes an important parameter as the vapor forms between the needle and sac.

However, in the high lift condition, off-axis displacement does not significantly affect the flow field since the vapor primarily forms within the injector holes.

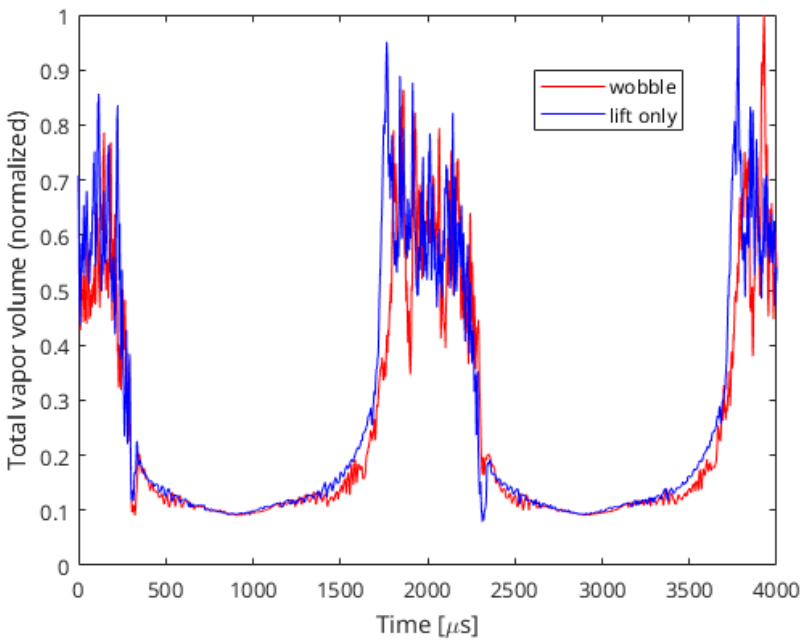

Figure 4.46: Comparison of total vapor volume change during simulation time

4.2.2 Erosion assessment: Comparison of lift only motion and wobbling motion

In this section, erosion assessment is carried out for dynamic needle simulations. Erosion pattern contours and vapor formations are presented at four consecutive time instants (t1, t2, t3, t4) as 875, 2000, 2875 and 4000 μs. The selected times correspond to the highest and lowest lift condition of each cycle. Figure 4.47 demonstrates selected time instants on the lift and off-axis profile plot with dashed lines. 2000 μs corresponds to one cycle of each simulation.

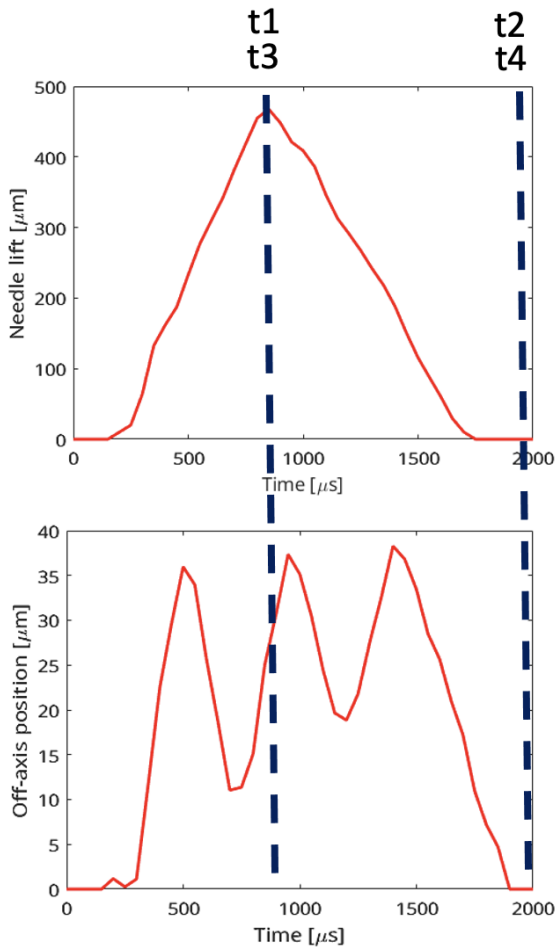

Figure 4.47: Selected time instants for the erosion assessment

Figure 4.48 and Figure 4.49 present the erosion patterns over the surfaces and vapor formations for corresponding lift only and wobbling motions. In each figure results are presented four time instants from top (t1) to the bottom (t4).

Before commenting on the results, it is worth to mention that there are not any moving needle experiments for this geometry. Besides, direct comparison with static needle experiments is challenging. When the needle is moving, it spends a very short time in high lift condition. However, at the beginning and end of each cycle, it remains in low lift condition for some time. Therefore, it is still possible to make a careful comparison with low lift experiments.

At time instant t1 (shown in top snapshots of both figures), for both lift only and wobbling motions, the sac and needle surfaces are getting damage at the early stages of the 1^{st} cycle. The damage patterns are similar, which might be because of the surface deviations. It should be reminded that the surface deviations do not exist only for the injector holes/orifices and there are large deviation regions in the upstream location of the sac. Figure 3.7 can be revisited to examine these surfaces. It is also evident for both of the cases that the damage patterns widen for all surfaces due to the continuous pitting behaviour with upcoming time.

To compare the final accumulated maximum erosion indicator values (erosion patterns) for both motions, the final time of both simulations is represented in Figure 4.50. Interestingly, the maximum values for the wobbling motion cover a smaller area compared to the lift only motion case. This leads us to consider the possibility of using wobbling profiles to enhance surface durability and reduce cavitation erosion.

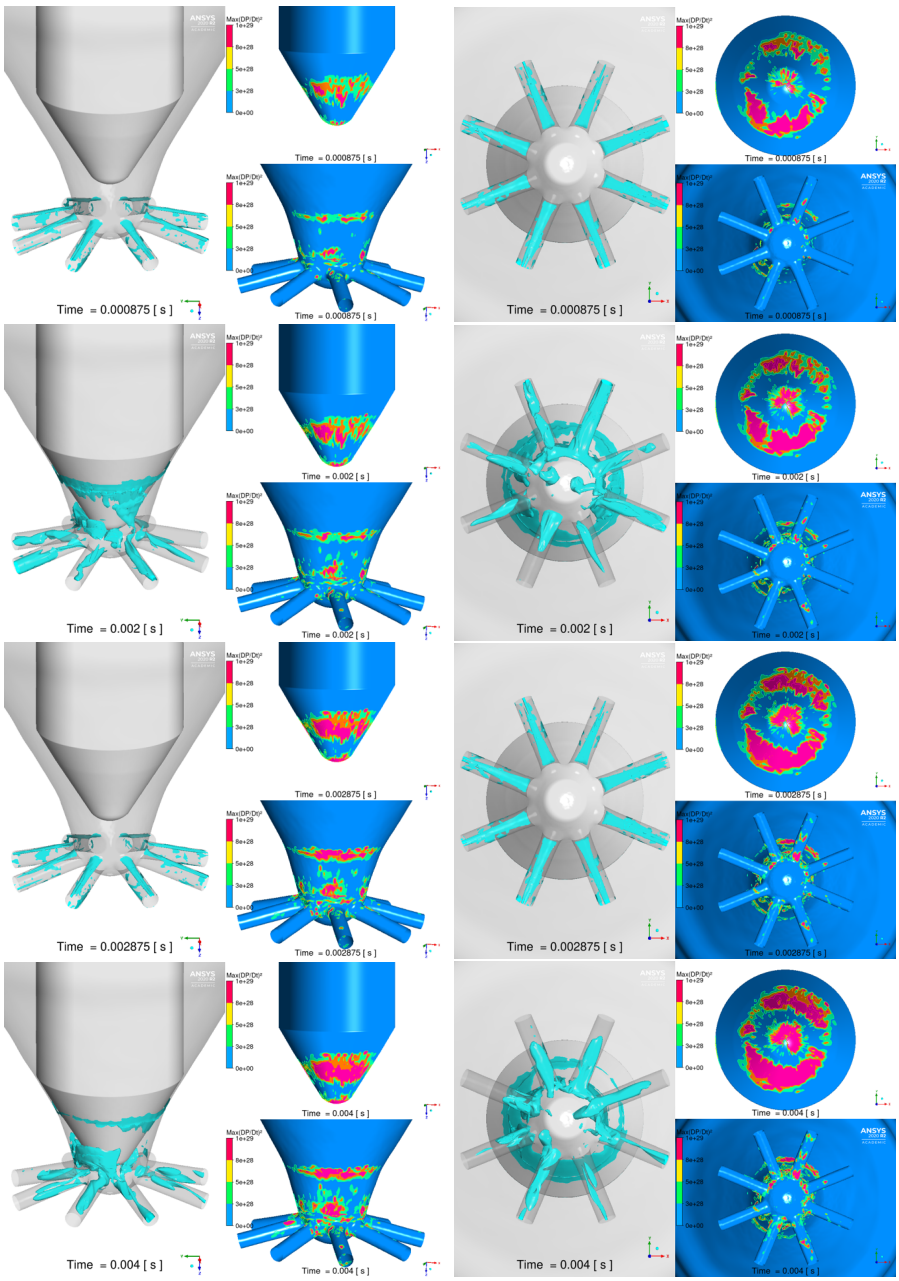

Figure 4.48: Erosion patterns over the surfaces and vapor formations, lift only motion, top to bottom t= t1, t2, t3, t4
Isometric (left) and Top (right) view

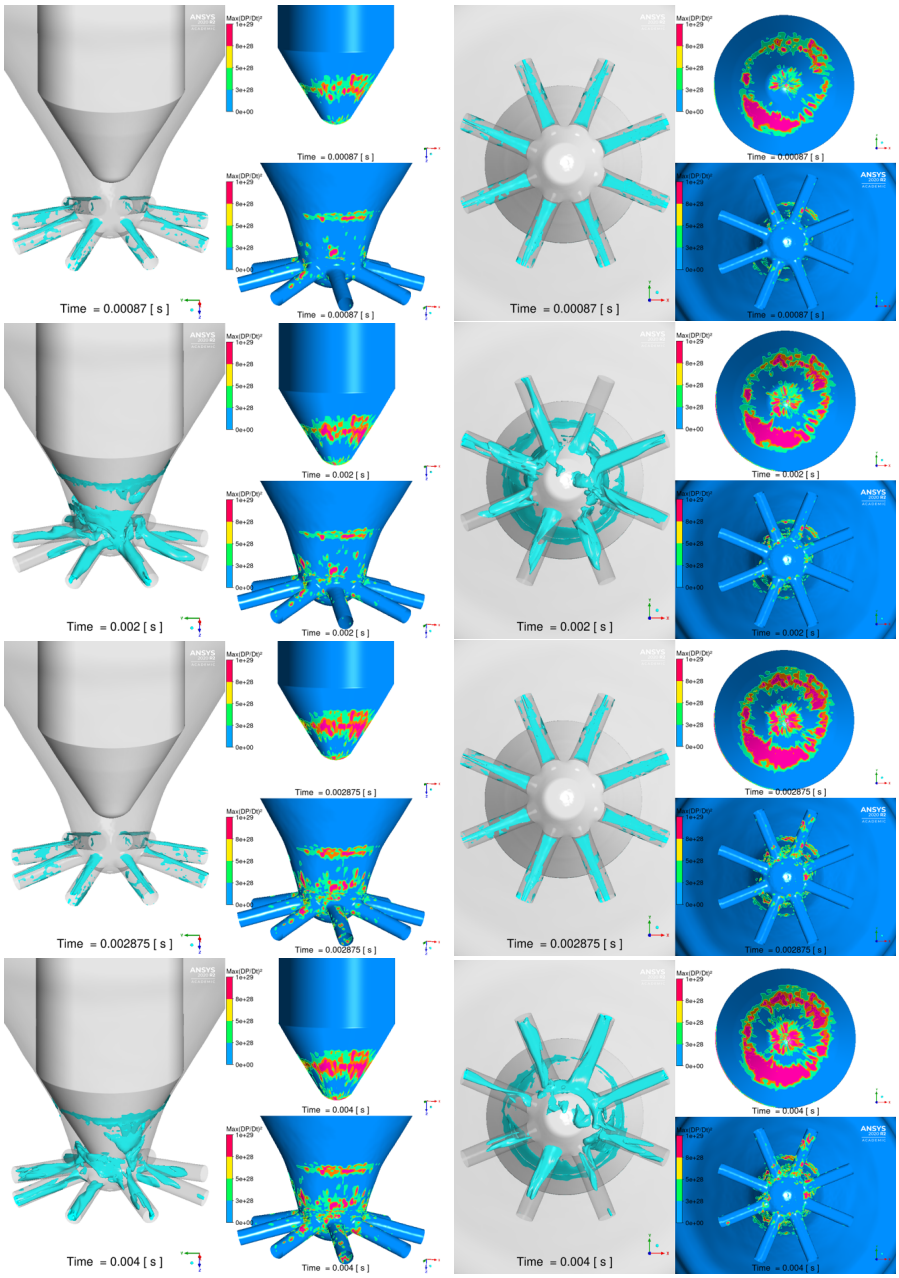

Figure 4.49: Erosion patterns over the surfaces and vapor formations, Wobbling Motion Motion, top to bottom t= t1, t2, t3, t4 Isometric (left) and Top (right) view

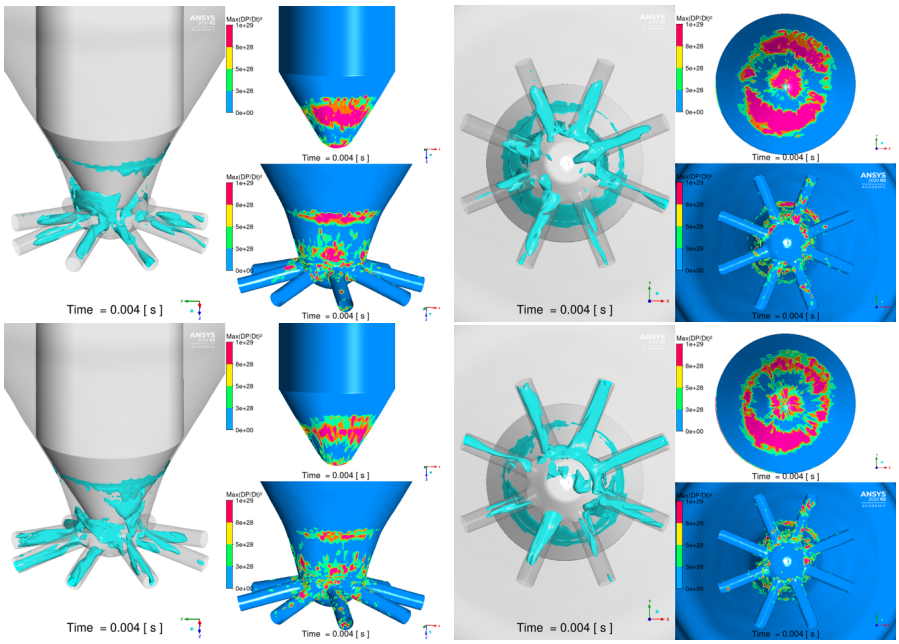

Figure 4.50: Erosion patterns over the surfaces and vapor formations at t = t4 top – Lift Only Motion, bottom - Wobbling Motion

Chapter 5

Conclusions and Future Work

This study explores the numerical assessment of cavitation-induced erosion in high-pressure fuel injectors using computational fluid dynamics (CFD). Reynolds-averaged Navier-Stokes (RANS) and Large Eddy Simulation (LES), are employed with specific sub-models. Cavitation is modeled using the mixture transport of modified Zwart-Gerber-Belamri approach. The investigation takes into consideration both low and high lift static needle positions, comparing the results with experimental data to gain insight into erosion behaviour. To examine the effect of the surface deviations to erosion patterns, static high lift condition is modeled with Computer Aided Design (CAD) and Tomography Scan (TS) Models separately. Finally, the effect of needle motion is carried out by implementing "wobbling" and "lift only" motion profiles using RANS.

Erosion assessment
The study employs MAX1 and MAX2 algorithms alongside four key variables — pressure (P), material derivative of pressure divided by cell volume $(DP/Dt)/V_{cell}$, square of material derivative of pressure $(DP/Dt)^2$, and second derivative of potential power density ($PPD2$) — to analyze cavitation erosion. Utilizing a User-Defined Function (UDF), MAX1 algorithm identifies peak conditions potentially leading to erosion by tracking maximum values of these parameters. While, MAX2 algorithm enhances analysis by preventing fake collapses with a refined criteria for potential cavitation collapse cells, offering a more detailed view on erosion dynamics. The results demonstrate the MAX2 algorithm's effectiveness in generating precise and localized erosion patterns that correspond well with experimental findings. The material derivative erosion indicators, especially $(DP/Dt)^2$, is highly reliable for identifying erosion patterns. Using the MAX2 algorithm together with $(DP/Dt)^2$ is advised for accurate cavitation erosion assessment in fuel injector simulations.

Turbulence modeling
When RANS and LES approaches are compared, the LES simulations provide a more dynamic and realistic representation of vapor structures and turbulence within the injector. The LES model captures a broader range of eddies and

flow structures, leading to more pronounced vapor formations and fluctuations in force dynamics. This enhanced dynamic behavior is noticeable in both lift positions, where LES predicts more significant changes in vapor volume and erosion patterns. Despite that the results are case specific, a good level of accuracy is provided with RANS, especially in the presence of TS Model. Considering the cost and time differences with LES, RANS is still an important and primary tool to assess the cavitation erosion.

Surface deviations
This study reveals that surface deviations significantly impact cavitation dynamics and erosion patterns. In the TS Model with high lift condition, the inclusion of surface deviations results in a reduction of the total vapor volume and alterations in erosion patterns, suggesting a more realistic replication of experimental conditions. The TS Model indicates more pronounced erosion patterns and demonstrating the importance of accurate surface modeling for predicting erosion in fuel injectors.

The wobbling motion
The dynamic needle simulations, especially those involving wobbling motion, exhibit distinct flow characteristics and erosion patterns compared to static needle simulations. The wobbling motion influences mass flow rates and vapor volume gradients. Notably, erosion patterns during wobbling motion are more localized and cover a smaller area than in lift-only simulations. This finding suggests the potential of wobbling motion to reduce cavitation erosion, enhancing the durability of the injector surfaces.

Overall Implications
The research underscores the significance of advanced modeling techniques and accurate geometric representation in predicting cavitation dynamics and erosion in fuel injectors. The insights gained from the LES model and the consideration of surface deviations offer a more comprehensive understanding of the cavitation phenomenon, which is crucial for the design and optimization of fuel injection systems. The findings also create new perspectives to explore dynamic needle motions as a strategy to mitigate erosion, which could lead to more durable and efficient fuel injectors.

In future work, the following topics will be investigated in detail, including their particular effect on erosion results:

- The surface deviations in low lift position,
- Wobbling only motion with different off-axis displacements,
- 8-hole LES simulations in both Low and high lift position.

Lastly, the proposed erosion model's accuracy and reliability for the MAX2 algorithm will be enhanced by introducing new erosion indicators based on the material derivative square, $(DP/Dt)^2$.

Bibliography

[1] International Maritime Organization, *2023 imo strategy on reduction of ghg emissions from ships*, 2023.

[2] J. Nouri, N Mitroglou, Y. Yan and C Arcoumanis, "Internal flow and cavitation in a multi-hole injector for gasoline direct-injection engines," SAE Technical Paper, Tech. Rep., 2007.

[3] R. Prasetya, A. Sou, J. Oki, A. Nakashima, K. Nishida, Y. Wada, Y. Ueki and H. Yokohata, "Three-dimensional flow structure and string cavitation in a fuel injector and their effects on discharged liquid jet," *International Journal of Engine Research*, vol. 22, no. 1, pp. 243–256, 2021.

[4] T. Cao, Z. He and J. Wang, "Investigation of cavitation phenomenon with different fuel temperatures in diesel nozzles," *Advances in Mechanical Engineering*, vol. 15, no. 10, 2023.

[5] J. Piehl and L. Bravo, "Assessment of cavitation models for computational fluid dynamics analysis of erosion risk in a hydrocarbon-fueled nozzle," *US Army Research Laboratory: Adelphi, MD, USA*, 2018.

[6] S. J. Schmidt, M. S. Mihatsch, M. Thalhamer and N. A. Adams, "Assessment of erosion sensitive areas via compressible simulation of unsteady cavitating flows," *Advanced experimental and numerical techniques for cavitation erosion prediction*, pp. 329–344, 2014.

[7] M. Dular, B. Stoffel and B. Širok, "Development of a cavitation erosion model," *Wear*, vol. 261, pp. 642–655, 2006.

[8] M. Dular and O. Coutier-Delgosha, "Numerical modelling of cavitation erosion," *International Journal for Numerical Methods in Fluids*, vol. 61, 2009.

[9] R. E. Bensow and G. Bark, "Implicit LES Predictions of the Cavitating Flow on a Propeller," *Journal of Fluids Engineering*, vol. 132, no. 4, Apr. 2010.

[10] Z. ru Li, M. Pourquié and T. V. Terwisga, "Assessment of cavitation erosion with a urans method," *Journal of Fluids Engineering-transactions of The Asme*, vol. 136, 2014.

[11] M. Mihatsch, S. Schmidt and N. Adams, "Cavitation erosion prediction based on analysis of flow dynamics and impact load spectra," *Physics of Fluids*, vol. 27, 2015.

[12] A. Peters, H. J. Sagar, U. Lantermann and O. E. Moctar, "Numerical modelling and prediction of cavitation erosion," *Wear*, vol. 338, pp. 189–201, 2015.

[13] A. Peters and O. el Moctar, "Numerical assessment of cavitation-induced erosion using a multi-scale Euler–Lagrange method," *Journal of Fluid Mechanics*, vol. 894, 2020.

[14] S. Schenke and T. V. Terwisga, "An energy conservative method to predict the erosive aggressiveness of collapsing cavitating structures and cavitating flows from numerical simulations," *International Journal of Multiphase Flow*, 2019.

[15] M. Arabnejad, U. Svennberg and R. Bensow, "Numerical assessment of cavitation erosion risk using incompressible simulation of cavitating flows," *Wear*, 2021.

[16] M. Arabnejad, U. Svennberg and R. Bensow, "Numerical assessment of cavitation erosion risk in a commercial water-jet pump," *Journal of Fluids Engineering*, 2021.

[17] F. Örley, S. Hickel, S. J. Schmidt and N. A. Adams, "Large-eddy simulation of turbulent, cavitating fuel flow inside a 9-hole diesel injector including needle movement," *International Journal of Engine Research*, vol. 18, no. 3, pp. 195–211, 2017.

[18] K. Kolovos, N. Kyriazis, P. Koukouvinis, A. Vidal, M. Gavaises and R. M. McDavid, "Simulation of transient effects in a fuel injector nozzle using real-fluid thermodynamic closure," *Applications in Energy and Combustion Science*, vol. 7, 2021.

[19] S. Falsafi, M. Blume, T. Klaua, M. Indrich, J. Wloka and R. Skoda, "Numerical simulation of cavitating flow in maritime high-pressure direct fuel injection nozzles and assessment of cavitation-erosion damage," *International Journal of Engine Research*, vol. 24, pp. 393 –407, 2021.

[20] E. Gomez Santos, J. Shi, R. Venkatasubramanian, G. Hoffmann, M. Gavaises and W. Bauer, "Modelling and prediction of cavitation erosion in gdi injectors operated with e100 fuel," *Fuel*, vol. 289, 2021.

[21] P. Koukouvinis, M. Gavaises, J. Li and L. Wang, "Large eddy simulation of diesel injector including cavitation effects and correlation to erosion damage," *Fuel*, vol. 175, pp. 26–39, 2016.

[22] P. Koukouvinis, I. K. Karathanassis and M. Gavaises, "Prediction of cavitation and induced erosion inside a high-pressure fuel pump," *International Journal of Engine Research*, vol. 19, no. 3, pp. 360–373, 2018.

[23] M. Brunhart, "Cavitation and the application of methods for erosion prediction in high pressure fuel injection systems," Ph.D. dissertation, City, University of London, 2020.

[24] R. F. Patella, A. Archer and C. Flageul, "Numerical and experimental investigations on cavitation erosion," in *IOP Conference Series: Earth and Environmental Science*, IOP Publishing, vol. 15, 2012.

[25] M. Cristofaro, W. Edelbauer, F. Koukouvinis and M. Gavaises, "Large eddy simulation of the internal injector flow during pilot injection," 2018.

[26] "A numerical study on the effect of cavitation erosion in a diesel injector," *Applied Mathematical Modelling*, vol. 78, pp. 200–216, 2020.

[27] M. Cristofaro, W. Edelbauer, P. Koukouvinis and M. Gavaises, "Influence of diesel fuel viscosity on cavitating throttle flow simulations under erosive operation conditions," *ACS Omega*, vol. 5, no. 13, pp. 7182–7192, 2020.

[28] A. Morozov and U. Iben, "Experimental analysis and simulation of cavitating throttle flow," International Conference on Heat Transfer, Fluid Mechanics and Thermodynamics, 2008.

[29] L. Zhang, Z. He, W. Guan, Q. Wang and S. Som, "Simulations on the cavitating flow and corresponding risk of erosion in diesel injector nozzles with double array holes," *International Journal of Heat and Mass Transfer*, vol. 124, pp. 900–911, 2018.

[30] A. Kumar, A. Ghobadian and J. Nouri, "Numerical simulation and experimental validation of cavitating flow in a multi-hole diesel fuel injector," *International Journal of Engine Research*, vol. 23, no. 6, pp. 958–973, 2022.

[31] C. Wang, M. Adams, T. Luo, T. Jin, F. Luo and M. Gavaises, "Hole-to-hole variations in coupled flow and spray simulation of a double-layer multi-holes diesel nozzle," *International Journal of Engine Research*, vol. 22, no. 10, pp. 3233–3246, 2021.

[32] G. M. Magnotti, M. Battistoni, K. Saha and S. Som, "Development and validation of the cavitation-induced erosion risk assessment tool," *Transportation Engineering*, vol. 2, 2020.

[33] F. Mariasiu, "Numerical investigation of the effects of biofuel characteristics on the injector nozzle erosion process," *Tribology transactions*, vol. 56, no. 2, pp. 161–168, 2013.

[34] S. Mouvanal, D. Chatterjee, S. Bakshi, A. Burkhardt and V. Mohr, "Numerical prediction of potential cavitation erosion in fuel injectors," *International Journal of Multiphase Flow*, vol. 104, pp. 113–124, 2018.

[35] F. Menter, "Zonal two equation kw turbulence models for aerodynamic flows," in *23rd fluid dynamics, plasmadynamics, and lasers conference*, 1993.

[36] F. Nicoud and F. Ducros, "Subgrid-scale stress modelling based on the square of the velocity gradient tensor," *Flow, Turbulence and Combustion*, vol. 62, no. 3, pp. 183–200, 1999.

[37] J.-L. Reboud, B. Stutz and O. Coutier, "Two phase flow structure of cavitation: Experiment and modeling of unsteady effects," in *3rd international symposium on cavitation CAV1998, Grenoble, France*, vol. 26, 1998, pp. 1–8.

[38] L. Davidson, "Large eddy simulations: How to evaluate resolution," *International Journal of Heat and Fluid Flow*, vol. 30, no. 5, pp. 1016–1025, 2009, The 3rd International Conference on Heat Transfer and Fluid Flow in Microscale.

[39] S. B. Pope, *Turbulent Flows*. Cambridge University Press, 2000.

[40] I. B. Celik, Z. N. Cehreli and I. Yavuz, "Index of Resolution Quality for Large Eddy Simulations," *Journal of Fluids Engineering*, vol. 127, no. 5, pp. 949–958, Sep. 2005.

[41] B. Befrui, G. Corbinelli, D. Robart, W. Reckers and H. Weller, "LES simulation of the internal flow and near-field spray structure of an outward-opening gdi injector and comparison with imaging data reprinted from: Si combustion and direct injection si engine," in *SAE World Congress and Exhibition*, SAE International, 2008.

[42] Q. Xue, S. Som, M. Battistoni, D. E. Longman, H. Zhao, P. K. Senecal and E. D. Pomraning, "Three-dimensional simulations of the transient internal flow in a diesel injector : Effects of needle movement," 2013.

[43] ANSYS, Inc., *Ansys fluent theory guide*, 2021 R1 edition, Canonsburg, Pennsylvania, USA, 2021.

[44] B. Budich, S. Schmidt and N. A. Adams, "Numerical simulation and analysis of condensation shocks in cavitating flow," *Journal of Fluid Mechanics*, vol. 838, pp. 759–813, 2018.

[45] P. Zwart, A. Gerber and T. Belamri, "A two-phase flow model for predicting cavitation dynamics," *Fifth International Conference on Multiphase Flow*, Jan. 2004.

[46] P. Koukouvinis, H. Naseri and M. Gavaises, "Performance of turbulence and cavitation models in prediction of incipient and developed cavitation," *International Journal of Engine Research*, vol. 18, no. 4, pp. 333–350, 2017.

[47] O. Coutier-Delgosha, R. Fortes-Patella and J.-L. Reboud, "Simulation of unsteady cavitation with a two-equation turbulence model including compressibility effects," *Journal of Turbulence*, vol. 3, no. 1, 2002.

[48] M. S. Mihatsch, S. J. Schmidt, M. Thalhamer and N. A. Adams, "Numerical prediction of erosive collapse events in unsteady compressible cavitating flows," in *MARINE 2011, IV International Conference on Computational Methods in Marine Engineering: Selected Papers*, Springer, 2013, pp. 187–198.

[49] F. Salvador, J. Martínez-López, J.-V. Romero and M.-D. Roselló, "Computational study of the cavitation phenomenon and its interaction with the turbulence developed in diesel injector nozzles by large eddy simulation (LES)," *Mathematical and Computer Modelling*, vol. 57, no. 7-8, pp. 1656–1662, 2013.

[50] R. Masuda, T. Fuyuto, M. Nagaoka, E. Von Berg and R. Tatschl, "Validation of diesel fuel spray and mixture formation from nozzle internal flow calculation," SAE Technical Paper, Tech. Rep., 2005.